130p.

ADVANCED TECHNOLOGY LABORATORIES

Schenectady, N. Y.

DESIGN CRITERIA FOR ZERO-LEAKAGE CONNECTORS FOR LAUNCH VEHICLES, VOL. 6, ENVIRONMENTAL EFFECTS

Edited By
S. LEVY

CONTRACT NAS 8-4012

MARCH 15, 1963

GENERAL ELECTRIC

FINAL REPORT FOR FIRST CONTRACT PERIOD

(March 1962 through February 1963)

DESIGN CRITERIA
FOR ZERO-LEAKAGE CONNECTORS
FOR LAUNCH VEHICLES

Contract NAS 8-4012

VOLUME 6

ENVIRONMENTAL EFFECTS

Edited by S. Levy

March 15, 1963

PREPARED FOR: Propulsion and Vehicle Engineering Division
George C. Marshall Space Flight Center
National Aeronautics and Space Administration
Huntsville, Alabama

PREPARED BY: Advanced Technology Laboratories
General Electric Company
Schenectady, New York

SPONSORED BY: Missile and Space Division
General Electric Company
Philadelphia, Pennsylvania

N.A.S.A. TECHNICAL MANAGER: C.C. Wood (M-P&VE-PT)

CONTENTS

61. THERMAL ANALYSIS OF CONNECTORS

by

S. Levy and L. H. Tomlinson

over

18323

61.0 Summary

This Section has been divided into four parts: Section 61.1, Fluid Heat Transfer Coefficients; Section 61.2, Radial Heat Flow Through a Surface Film into a Circular Flange; Section 61.3, Temperature Transients in Bolts; and Section 61.4, Temperature Transient Analysis in Flange Assemblies.

Section 61.1 is included because knowledge of the fluid heat-transfer coefficient is necessary in order to evaluate the magnitude and duration of temperature gradients within a flange connection during the transient state after flow has started. In several examples, coefficients are calculated for a hot combustion gas, liquid oxygen in straight forced convection, and liquid oxygen in two-phase flow. Also a coefficient is calculated for a blanket of stagnant gas to show how it could be used to insulate the inner wall of a flange against sharp temperature changes. It may be stated that calculations of heat-transfer coefficients in single-phase flow are fairly simple and straight-forward as illustrated in the first two examples. In two-phase flow, however, this is not the case, and in many situations the coefficients may only be estimated or guessed at by people with considerable experience and knowledge in the field.

Section 61.2 presents a thermal analysis of transient heat flow into a flange which takes into account the curvature of the flange and is the type of analysis necessary for the larger radius ratios (outer radius divided by inner radius. It is assumed that the flange temperature rise (or fall) can be adequately described by a function such as $T = Ar^n + B$ where A and B are functions of time and n is a constant. A and B are determined by the conditions that (1) the total change in heat content of the flange equals the integrated heat flow through the boundary layer film; and (2) the total change in heat content of the flange outside the mid-radius circle equals the integrated heat flow through the mid-radius circle. The constant n is determined to satisfy the requirement of equal heat flow through the surface film and into the flange at the time of maximum temperature difference from inner to outer wall of the flange. It is assumed that the heat flows radially only. The film coefficient and the thermal properties of the flange material are considered constants. Analytical expressions are given for the maximum temperature difference and the time at which it occurs. The results are in a form which can readily be used in Section 48 to obtain distortions and stresses. Numerical results are presented for several examples. These show a greater temperature difference for the case of a stainless-steel flange than for an aluminum flange, as might be expected, The results are also compared with results using "exact" methods for a flat slab of thickness equal to the flange thickness. Multiplying certain coefficients by a factor of 0.95 brought the agreement to within about a percent.

18323

Section 61.3 presents some preliminary information on what the bolt temperature transients might be. Some temperature transient curves worked up for a particular flange are presented and are used also for the bolt which has a similar path length. Also included is a brief discussion of thermal resistance of metal-to-metal surface contacts along with curves summarizing some of the most applicable data. These data show that for low bolt pressures, and especially for the steels, the thermal conductivity may run from a few hundred to a few thousand Btu/hr.ft^2 ^{o}F. At high bolt loading and for the softer metal, aluminum, the thermal conductivity may reach many thousands of Btu/hr.ft^2 ^{o}F and the joint may for all practical purposes be considered to be bridged by conducting metal.

Section 61.4 presents the analysis of temperature transients in flange assemblies by the use of a digital computer. Preliminary investigation shows that the low-profile flanges (with radius ratios close to 1) used commonly in the missile industry may be regarded as sections of flat plate for purposes of analysis. The permissible radius ratios are as high as 1.4. Analysis of a simple model system representing a flat plate on the digital computer showed very good agreement with previously known flat-plate data. Equations are presented for the analysis of much more complex model systems representing a specific flange assembly. The computer solution for this case is given. It shows good agreement with the appropriate results obtained in Section 61.3.

5

61.1 Fluid Heat Transfer Coefficients (by L.H. Tomlinson)

61.1.1 Introduction

The fluid heat transfer coefficient at the inner wall of a flange will have an important effect on the magnitude and duration of thermal transients within the flange. Very high coefficients (in the thousands of Btu/hr. ft.^{2} $^\circ$F) result in the inner surface driving toward the fluid temperature very quickly. In this case, thermal constants of the flange material exercise most of the control over the thermal history. Lower heat transfer coefficients which may sometimes be encountered will result in reduction of the temperature transients and gradients, and the magnitude of the coefficient will be of considerable importance. It should be noted at this time that all work to date has considered the outside of the flange insulated. Heat flow from the pipe wall into the flange will be small until a combination of very low fluid heat transfer coefficients and high flange conductivity is encountered.

The thermal characteristics of the system may be best described through the use of two dimensionless numbers:

the Fourier Number, $K\tau/\rho cs^2$

and the Biot Number, hs/K

where, K = thermal conductivity of flange material
ρ = density of flange material
c = specific heat of flange material
s = radial thickness of flange
τ = time
h = heat transfer coefficient of the fluid at inner surface of the flange

It will be shown elsewhere how these numbers are related to the thermal transients in the flanges. For the remainder of this section we will confine our discussion to methods of evaluating the h in the Biot Number above.

The heat transfer equation with the widest application to the fluids encountered in missile work is the Dittus-Boelter equation for flow in pipes. In various standard heat transfer texts (Refs. 1-3), this equation may be found with several slightly different coefficients. For calculations done here, the following forms of the Dittus-Boelter equation are used (Ref. 2, p. 394):

$$Nu = 0.023\ (Re)^{0.8}(Pr)^{0.4} \quad \text{for heating the fluid} \tag{1}$$

$$Nu = 0.023\ (Re)^{0.8}(Pr)^{0.3} \quad \text{for cooling the fluid} \tag{2}$$

The above dimensionless numbers may be written as follows:

$Nu = hD/K_f$ Nusselt's number (3)

$Re = DG/\mu$ Reynolds' number (4)

$Pr = c\mu/K_f$ Prandtl's number (5)

	Typical set of consistent units
where h = heat transfer coefficient of the fluid	(Btu/hr.ft.^{2} $^\circ$F)
D = diameter of pipe	(ft.)
K_f = thermal conductivity of fluid	(Btu/hr.ft. $^\circ$F)
G = mass flow density	(lb./hr.ft.^{2})
μ = fluid viscosity	(lb./hr.ft.)
c = heat capacity of fluid	Btu/lb. $^\circ$F

Other equations will be introduced where required. Examples that will now be calculated are listed as follows:

1. Hot combustion gas flowing in 2 in. I.D. pipe
2. Liquid oxygen flowing in 20 in. I.D. pipe
3. Nucleate boiling of liquid oxygen
4. Stagnant film of oxygen gas

7

61.1.2 Sample Calculations of Heat Transfer Coefficients

Example 1. Heat transfer coefficient for hot combustion gas flowing in 2 in. I.D. pipe.

Given data: 10000 lb./hr. flow rate
1700°F gas temp.
940 psi pressure

The following were obtained from Ref. 3, assuming that values for air are close enough at the low temperature of the gases:

$\mu = 3.1 \times 10^{5}$ lb./sec. ft. or 0.111 lb./hr. ft.

$c = 0.28$ Btu/lb. °F

$K_f = 0.044$ Btu/hr. ft. °F

It may be calculated that:

$$G = \frac{10000 \times 144}{\pi} = 4.58 \times 10^{5} \text{ lb./hr. ft.}^2$$

$$D = \frac{2}{12} = 0.167 \text{ ft.}$$

Equation (2) will be used for this case

$$Nu = 0.023(Re)^{0.8}(Pr)^{03}$$

$$Re = DG/\mu = \frac{0.167 \times 458000}{0.111} = 6.89 \times 10^{5}$$

$$Pr = C\mu/K_f = \frac{0.28 \times 0.111}{0.444} = 0.705$$

$$Nu = hD/K_f = 0.023(689000)^{0.8}(0.705)^{0.3}$$

$$h = \frac{0.044 \times 0.023(46600)(0.90)}{0.167}$$

$$= 254 \text{ Btu/hr. ft.}^2 \text{ °F}$$

Example 2. Heat transfer coefficient for liquid oxygen flowing in 20 in. I.D. pipe at a flow rate of 3917 lb./sec.

The following were obtained from Ref. 5:

$\mu = 0.36$ lb./ft. hr.
$c = 0.4$ Btu/lb. °F
$K_f = 0.08$ Btu/hr. ft. °F

It may be calculated that:

$$G = \frac{3917 \times 3600 \times 144}{100\pi} = 6.45 \times 10^6 \text{ lb./hr. ft.}^2$$

$$D = \frac{20}{12} = 1.67 \text{ ft.}$$

Equation (1) will be used for this case.

$$Nu = 0.023(Re)^{0.8}(Pr)^{0.4}$$

$$Re = DG/\mu \quad \frac{1.67 \times 6.45 \times 10^6}{0.36} = 30 \times 10^6$$

$$Pr = c\mu/K_f = \frac{0.4 \times 0.36}{0.08} = 1.8$$

$$Nu = hD/K_f = 0.023(30 \times 10^6)^{0.8}(1.8^{0.4}$$

$$h = \frac{0.08 \times 0.023 \times 9.6 \times 10^5 \times 1.265}{1.67}$$

$$= 1340 \text{ Btu/hr. ft.}^2 \text{ }^\circ\text{F}$$

Example 3. Heat transfer coefficient for nucleate boiling of liquid oxygen flowing at 3917 lb./sec. in a 20 in. I.D. pipe. Pressure is low at this point (100 psi).

First the burnout heat flux for pool boiling (no flow) is calculated by the following equation of Zuber (Ref. 3, p. 349).

$$Q/A = \frac{\pi H_{fg} \rho_v}{24} \left[\frac{\sigma g(\rho_\ell - \rho_v)}{\rho_v^2}\right]^{0.25} \left(\frac{\rho_\ell + \rho_v}{\rho_\ell}\right)^{0.5} \qquad (6)$$

The terms are defined and evaluated as follows, the information coming from Ref. 5.

$\rho_\ell = 72$ lb./ft.^{3}	liquid density
$\rho_v = 0.25$ lb./ft.^{3}	vapor density
$H_{fg} = 92$ Btu/lb.	heat of vaporization
$\sigma = 35.3 \times 10^{-3}$ lb./sec.^{2}	surface tension
$g = 32.2$ ft./sec.^{2}	gravitational constant

Substituting these values in Eq. 6

$$Q/A = \frac{\pi \times 92 \times 0.25}{25} \left(\frac{35.3 \times 10^{-3} \times 32.2 \times 72}{0.25^2}\right) \text{ neglecting final term}$$

$$Q/A = 18 \text{ Btu/ft.}^2 \text{ sec.}$$

$$= 65{,}000 \text{ Btu/ft.}^2 \text{ hr.} \qquad \text{burnout heat flux}$$

Now that the burnout flux is known, a heat transfer coefficient for pool boiling is calculated by use of the following equation of Labuntsov (Ref. 4)

$$\frac{h}{K\ell}\ \frac{c\rho_\ell}{(\rho_v H_{fg})^2}\ \frac{\sigma T_s}{J} = 0.125(N_{RE})^{0.65}(Pr)^{\frac{1}{3}} \tag{7}$$

where

$$N_{Re} = \frac{\rho_\ell^2 (Q/A)\, c\sigma T_s}{\mu(\rho_v H_{fg})^3 J} \tag{8}$$

The additional terms needed for the above equations are defined and evaluated as follows, the information coming from Ref. 5

K_ℓ	= 0.08 Btu/hr. ft. ^oF	thermal conductance of liquid oxygen
c	= 0.4 Btu/lb. ^oF	thermal capacity of liquid oxygen
J	= 778 ft. lb./min. Btu	mechanical equivalent of heat
T_s	= 205^oR	saturation temperature at 100 psi
μ	= 0.36 lb./ft. hr.	viscosity of liquid
σ	= 1.1 x 10^{-3} lb./ft.	surface tension

$$Pr = c\mu/K_\ell = \frac{0.4 \times 0.36}{0.08} = 1.8$$

Evaluating equation (8) we get

$$N_{Re} = \frac{72^2(65{,}000)0.4 \times 1.1 \times 10^{-3} \times 162}{0.36(0.25x92)^3\ 778}$$

$$= 7.05$$

Equation (7) may now be evaluated.

$$\frac{h \times 0.4 \times 72 \times 1.1 \times 10^{-3} \times 162}{0.08(0.25x92)^2\ 778} = 0.125(7.05)^{0.65}(1.8)^{\frac{1}{3}}$$

h = 3230 Btu/hr. ft.^{2} ^oF pool boiling heat transfer coefficient.

The temperature difference between wall and saturated liquid may now be calculated

$$T_w - T_x = Q/Ah = \frac{65000}{3230} = 20^{\circ}F$$

The next step is to compute a burnout heat flux for the flowing liquid oxygen by the following equation of Kutaleladze (Ref. 6)

$$\frac{Q/A}{\rho_v H_{fg}} \left[\frac{\rho_v^2}{\sigma g(\rho_\ell - \rho_v)}\right]^{0.25} \tag{9}$$

$$= 0.085\left[V\left(\frac{\rho_\ell - \rho_v}{\sigma g}\right)^{0.25}\right]^{0.5}\left[1 + 0.057\left(\frac{\rho_\ell}{\rho_v}\right)^{0.5} \frac{c\left(T_s - T_\ell\right)}{H_{fg}}\right]$$

Two additional terms need to be defined and evaluated

$V = 25.3$ ft./sec. velocity of liquid flow

$T_\ell = 205^{\circ}F$ temperature of liquid

Equation (9) is now evaluated

$$\frac{Q/A}{.025 \times 92}\left[\frac{.025^2}{35.3 \times 10^{-3} \times 32.2 \times 72}\right]^{0.25}$$

$$= 0.085\left[25.3\left(\frac{72}{35.3 \times 10^{-3} \times 32.2}\right)^{0.25}\right]^{0.5}\left[1+0.057\left(\frac{72}{0.25}\right)^{0.5} \frac{0.4(0)}{92}\right]$$

$Q/A = 9{,}700$ Btu/sec. ft.^{2} $^{\circ}F$

$= 350{,}000$ Ftu/hr. ft.^{2} $^{\circ}F$

Now Fig. 61.0 is constructed as shown with a line of slope equal to 3 passing through the pool boiling flux and $(T_w - T_s)$. Then the new burnout flux just calculated is entered on the curve and a new $(T_w - T_s)$ value of $39^{\circ}F$ obtained. This graphical method was described to the author in a personal communication from N. Zuber who is now in the Advanced Technology Laboratories of General Electric Co.

Now $h = \frac{Q/A}{(T_w - T_s)}$

$= \frac{350{,}000}{39}$

$= 9{,}000$ Btu/hr. ft.^{2} $^{\circ}F$ heat transfer coefficient for nucleate boiling in the flowing oxygen stream.

FIGURE 61.0

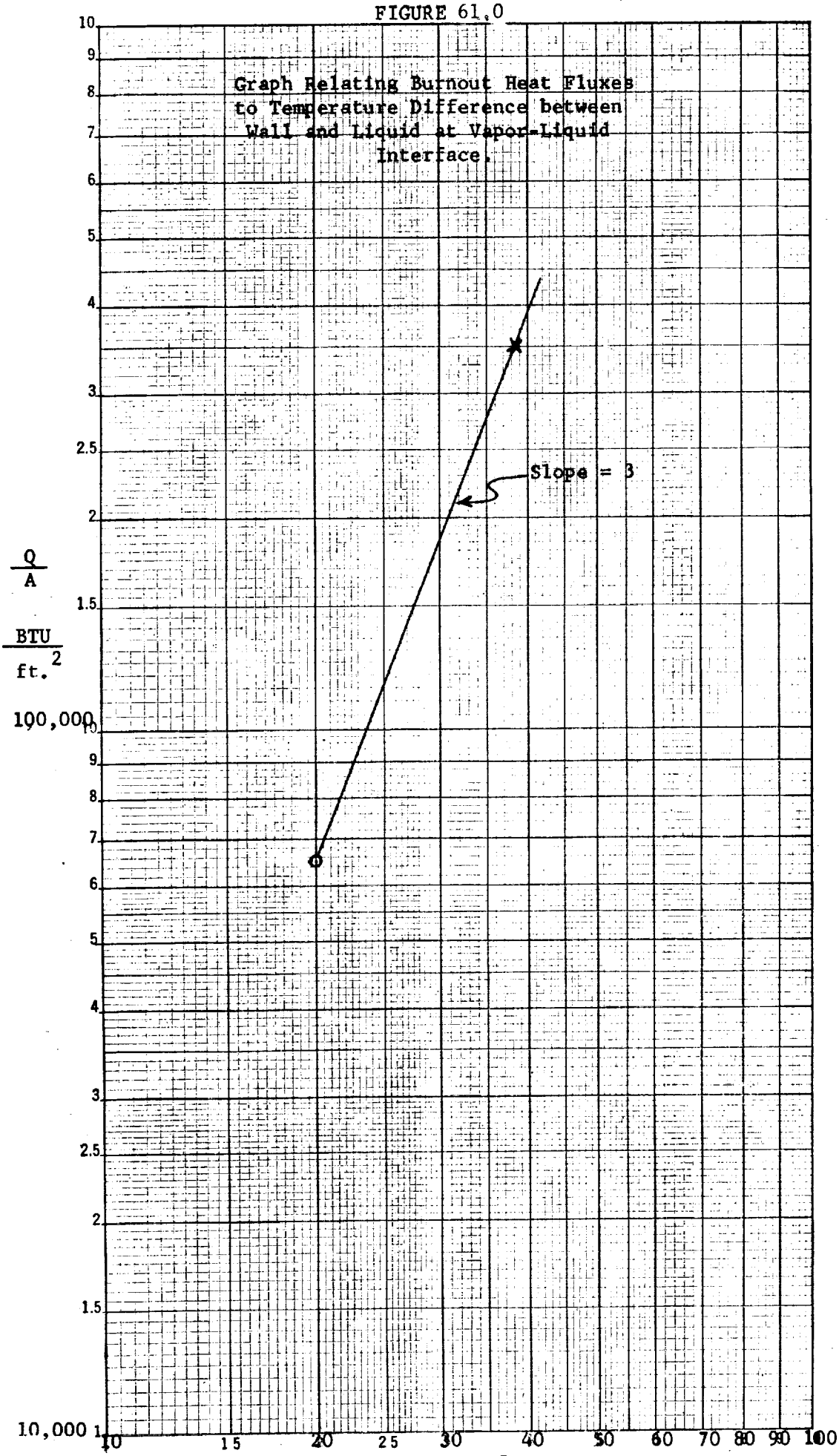
Graph Relating Burnout Heat Fluxes to Temperature Difference between Wall and Liquid at Vapor-Liquid Interface.
Slope = 3
Q/A BTU/ft.2
100,000
10,000
10
9
8
7
6
5
4
3
2.5
2
1.5
1
10
15
20
25
30
40
50
60
70
80
90
100
Tw - Ts (°F)

Example 4. Heat transfer coefficient for a stagnant film of oxygen vapor at low temperature.

The main reason for making this simple little calcuation is to show how low the heat transfer coefficient might go and to suggest a possible use for this.

Assume the vapor film to be at about -250F and the thickness to be 1/16 in. Then Ref. 5 gives a value for K_f of 0.0061 Btu/hr. ft. ^{o}F,

Then: $h = K_f/s$

$= 0.0061 \times 12 \times 16$

$= 1.15$ Btu/hr. $ft.^2$ ^{o}F

The actual value will no doubt be several times higher due to natural convection or flow leakage, but this is still far lower than any of the normally occurring fluid coefficients and could be applied to certain flanges in order to reduce the magnitude of the temperature transients in them. The method of application might be to place a thin metal sleeve liner in the pipe at each flange location so that vapor might be trapped behind it. This scheme would be considerably less effective for hot gases due to heat radiation and to the higher conductivity of a hot gas.

61.1.2 Discussion

From the above examples and other calculations made in the past, one may devise a chart illustrating the approximate ranges into which the coefficients may be expected to fall.

Flow condition	Heat transfer coefficient (Btu/hr ft^2 ^oF)
Gas flow	100-500
Liquid flow	
Straight convection	200-2000
Film boiling	100-300
Nucleate boiling	1000-10,000

The above ranges of coefficients are higher than would be expected in normal practice and most examples will perhaps lie on the high end of these ranges. These high heat transfer coefficients are commonly encountered in the missile field because fluid transfer is being carried out very rapidly in minimum-weight equipment with flow friction losses being of secondary importance.

In actual practice it is possible that in the initial transient, all regimes of heat transfer coefficients may be passed through by cryogenic fluids at lower pressures. Initially, with high temperature differences, film boiling may exist. Then as temperature differences decrease some nucleate boiling may take place, only to be followed by straight liquid convection as inner wall temperatures fall to near the fluid temperature. At higher pressures, forced convection may be the only mode of heat transfer encountered. The boundaries for each of these modes will depend upon: (1) the fluid properties; (2) the pressure and flow conditions; (3) the material and temperature of the flange; and (4) the conditions just upstream of the flange.

11

61.1.4 Conclusion

In conclusion, two main statements should be made on the subject of calculation of heat transfer coefficients.

1. Calculations are straightforward for the case of single phase flow and use of the Dittus-Boelter equation or its equivalent will be satisfactory for practically all the fluids encountered (not liquid metals).

2. Calculations are not so simple for two-phase flow, and in some cases exact coefficients cannot be obtained without experimental data. This field is still being studied and data obtained and correlated. It would be wise to consult an authority on two-phase flow or at least have on hand authoritative information covering the situation in question.

61.2.2 Nomenclature

T	temperature rise (^{o}F). (Minus sign indicates a fall)
A, B, n	terms in $T = A(r/a)^{n} + B$
r	radius (ft)
a	inner radius of flange (ft)
b	outer radius of flange (ft)
t	time (hr)
$c\gamma$	heat content per unit volume of flange material per ^{o}F temperature rise (BTU/cu ft/^{o}F)
h	film coefficient (BTU/hr/sq ft/^{o}F)
k	thermal conductivity (BTU/hr/sq ft/(^{o}F/ft))
T_a	inner wall temperature rise (^{o}F)
T_b	outer wall temperature rise (^{o}F)
T^*	fluid temperature difference from initial flange temperature (^{o}F)
C_1, C_2, C_5	terms in $B/T^* = C_1 e^{m_1 t} + C_2 e^{m_2 t} + C_{10}$
C_3 and C_4	terms in $A/T^* = C_3 e^{m_1 t} + C_4 e^{m_2 t}$
m_1, m_2	constants in above equations

61.2.3 Results

It is shown in Section 61.2.6 that the temperature in the flange is given by:

$$T/T^* = \left[C_1 + C_3(r/a)^n\right]\exp(m_1 t) + \left[C_2 + C_4(r/a)^n\right]\exp(m_2 t) \qquad (1)$$

where,

$$C_1 = \left\{ -\left(\frac{m_2}{m_2-m_1}\right) - \left(\frac{m_1 m_2}{m_2-m_1}\right)\left(\frac{1}{n+2}\right)\left(\frac{c\gamma}{nk}\right)\frac{\left[b^{(n+2)} - \left(\frac{a+b}{2}\right)^{(n+2)}\right]}{\left(\frac{a+b}{2}\right)^n} \right\}(0.95)$$

$$C_2 = -C_1 - 1 \quad \text{(see Fig. 61.3)}$$

$$C_3 = \left\{ \left(\frac{m_1 m_2}{m_2-m_1}\right)\left(\frac{c\gamma}{2nk}\right)\frac{\left[b^2 - \left(\frac{a+b}{2}\right)^2\right]}{\left(\frac{a+b}{2a}\right)^n} \right\}(0.95)$$

$$C_4 = -C_3 \quad \text{(see Fig. 61.3)}$$

$$n = \left[\log\left(\frac{a+3b}{4a+4b}\right) \Big/ \log\left(\frac{a+b}{2a}\right)\right] \quad \text{(see Fig. 61.1)}$$

and m_1 and m_2 (see Fig. 61.2) satisfy the equation

$$C_5 m^2 + C_6 m + C_7 = 0$$

where,

$$C_5 = \frac{\left[b^{(n+2)} - a^{(n+2)}\right]}{(n+2)} - \frac{(b^2-a^2)}{(n+2)}\frac{\left[b^{(n+2)} - \left(\frac{a+b}{2}\right)^{(n+2)}\right]}{\left[b^2 - \left(\frac{a+b}{2}\right)^2\right]} \qquad (2)$$

$$C_6 = \left(\frac{ah}{c\gamma}\right)a^n - \left(\frac{nk}{c\gamma}\right)\frac{\left[b^2-a^2\right]\left(\frac{a+b}{2}\right)^n}{\left[b^2 - \left(\frac{a+b}{2}\right)^2\right]} - \left[\frac{2ah}{c\gamma(n+2)}\right]\frac{\left[b^{(n+2)} - \left(\frac{a+b}{2}\right)^{(n+2)}\right]}{\left[b^2 - \left(\frac{a+b}{2}\right)^2\right]}$$

$$C_7 = -\left(\frac{2ah}{c\gamma}\right)\left(\frac{kn}{c\gamma}\right)\frac{\left(\frac{a+b}{2}\right)^n}{\left[b^2 - \left(\frac{a+b}{2}\right)^2\right]}$$

17

The temperature difference between r = a and r = b is shown to be given by

$$\left(\frac{T_a - T_b}{T^*}\right) = \left[\frac{m_1 m_2}{m_2 - m_1}\right]\left(\frac{c\gamma}{2nk}\right)\left[\frac{a^n - b^n}{\left(\frac{a+b}{2}\right)^n}\right]\left[b^2 - \left(\frac{a+b}{2}\right)^2\right]\left[\exp(m_1 t) - \exp(m_2 t)\right] \quad (0.95) \qquad (3)$$

The time at which the maximum value of the difference occurs is (see Fig. 61.4)

$$t_{max} = \frac{\log\,(m_1/m_2)}{m_2 - m_1}$$

$$\exp(m_1 t_{max}) = \left(\frac{m_1}{m_2}\right)^{\left(\frac{m_1}{m_2 - m_1}\right)} \quad ; \quad \exp(m_2 t_{max}) = \left(\frac{m_1}{m_2}\right)^{\left(\frac{m_2}{m_2 - m_1}\right)} \qquad (4)$$

The maximum value of the difference is (see Fig. 61.5)

$$\left(\frac{T_a - T_b}{T^*}\right)_{max} = (0.95)\left[\frac{m_1 m_2}{m_2 - m_1}\right]\left(\frac{c\gamma}{2nk}\right)\left[\frac{(a^n - b^n)}{\left(\frac{a+b}{2}\right)^n}\right]\left[b^2 - \left(\frac{a+b}{2}\right)^2\right]\left[\left(\frac{m_1}{m_2}\right)^{\left(\frac{m_1}{m_2 - m_1}\right)} - \left(\frac{m_1}{m_2}\right)^{\left(\frac{m_2}{m_2 - m_1}\right)}\right] \qquad (5)$$

The maximum value of A (see Fig. 61.6) is valuable in computing stress. It is given by

$$\left(\frac{A}{T^*}\right)_{max} = (0.95)\left[\frac{m_1 m_2}{m_2 - m_1}\right]\left(\frac{c\gamma}{2nk}\right)\frac{\left[b^2 - \left(\frac{a+b}{2}\right)^2\right]}{\left(\frac{a+b}{2a}\right)^n}\left[\left(\frac{m_1}{m_2}\right)^{\left(\frac{m_1}{m_2 - m_1}\right)} - \left(\frac{m_1}{m_2}\right)^{\left(\frac{m_2}{m_2 - m_1}\right)}\right] \qquad (6)$$

›1.2.4 Examples

Example 1: Consider a flange joint in a pipe (stainless steel) which is suddenly exposed to the flow of liquid oxygen at a temperature 300°F less than the initial temperature of the pipe. Then $T^* = -300^\circ F$. The inner flange radius a = 3 in. = 0.250 ft. The outer flange radius b = 4 in. = 0.3333 ft. Let the value of $c\gamma$ = 52.4 BTU/cu. ft./°F, the value of k = 12.4 BTU/hr./ft.²/(°F/ft.) and the value of h = 500 BTU/hr./sq. ft./°F. What is the maximum temperature difference in the flange?

a. From Eq. 1 or Fig. 61.1, n = -4.1

b. From Eq. 2 or Fig. 61.2, m = -604, $m_2 = -42.9$

c. From Eq. 4 or Fig. 61.4, $t_{(max,\ diff.)} = 0.00471$ hrs. = 1.70 sec.

d. From Eq. 5 or Fig. 61.5, $(T_a - T_b)_{max} = -171^\circ F$

e. From Eq. 1 or Fig. 61.3, $C_1 = 0.519$ $C_2 = -1.519$

$C_3 = -1.015$ $C_4 = 1.015$

f. From Eq. 1 at the time given by (c) and using Eq. 4, we get

$(T_a)_{(max,\ diff.)} = -172^\circ F$ $(T_b)_{(max.\ diff.)} = -1.2^\circ F$

g. From Eq. 6 or Fig. 61.6 $(A)_{max} = -250^\circ F$

h. It is of interest that at the time of maximum temperature difference, $\exp(m_1 t) = 0.0579$ and $\exp(m_2 t) = 0.8169$.

Example 2: In this example we consider a larger flange with material having greater conductivity (aluminum). Inner radius a = 10 in. = 0.8333 ft., outer radius b = 11.3125 in. = 0.9427 ft., $c\gamma$ = 36.2 BTU/cu. ft./°F, k = 118 BTU/hr./sq. ft./(°F/ft.), and h = 500 BTU/hr./sq. ft./°F. What is the maximum ratio of the temperature difference to the fluid temperature?

a. Proceeding as was done in Example 1, we find n = -10.5, giving $m_2 = -102.0$ and $m_1 = -2425$.

b. Substituting these values in Eq. 4 or using Fig. 61.4, gives $t_{(max.diff.)} = 4.9$ secs. (.00136 hrs.)

c. Substituting in Eq. 5 or using Fig. 61.5, gives $(T_a - T_b)_{max} = 0.176T^*$

61.2.5 Discussion

An approximate method of calculating thermal transients in pipe flanges has been presented. It takes account of the flange curvature and in this respect adds additional information to "exact" methods that consider the flange to be flat. A correction factor of about 5 percent has been applied to some coefficients to bring the results presented within about 1 percent of "fitting in" with the flat-plate results. Curvature is shown to be a small factor. No account has been taken of axial flow of heat from the hub into the flange. In general, it is felt that such a heat flow would increase the effective value of h and thus result in somewhat greater temperature differences than would otherwise be reached.

The examples indicate that substantial temperature differences develop in flanges having low thermal conductivity in the presence of a high film coefficient. Flange thickness increases also increase the temperature difference. For the examples presented, the time required to achieve the maximum temperature difference was only a few seconds. This indicates that thermal transients in pipe flanges occur quickly.

In the design of pipe flanges, it might be possible to modify considerably the transient behavior by including an insulating sleeve at the flange or by modifications in the flow pattern at the flange. Such schemes of thermal design warrant further study.

20

61.2.6 Appendix: Thermal Analysis

We assume that the flange temperature rise can be adequately described by

$$T = A(r/a)^n + B \tag{1A}$$

where A and B are functions of time and n will be subsequently selected for fit. We can determine A and B by the conditions:

a. The total rise in heat content of the flange equals the net heat flow through the boundary layer; and

b. The total rise in heat content of the outer half of the flange (outside of mid-radius) equals the net heat flow through the mid-radius layer.

These conditions give

$$ah\left(T^*-T_a\right) = \frac{d}{dt}\int_a^b rTc\gamma dr \tag{2A}$$

$$\left(\frac{a+b}{2}\right) k \left(\frac{dT}{dr}\right)_{\left(r=\frac{a+b}{2}\right)} = -\frac{d}{dt}\int_{\left(\frac{a+b}{2}\right)}^b rTc\gamma dr \tag{3A}$$

Substituting Eq. (1A) into (2A) and (3A) and integrating

$$\left(\frac{ah}{c\gamma}\right)(T^*-A-B) = \left(\frac{b^2-a^2}{2}\right)\frac{dB}{dt} + \left[\frac{b^{(n+2)}-a^{(n+2)}}{(n+2)a^n}\right]\frac{dA}{dt} \tag{4A}$$

$$\text{Note: } \left[\frac{b^{(n+2)}-a^{(n+2)}}{n+2}\right] \longrightarrow \log\frac{b}{a} \text{ as } n \longrightarrow -2$$

and

$$-\left(\frac{nk}{c\gamma}\right)\left(\frac{a+b}{2a}\right)^n A = \left[\frac{b^2-\left(\frac{a+b}{2}\right)^2}{2}\right]\frac{dB}{dt} + \left[\frac{b^{(n+2)}-\left(\frac{a+b}{2}\right)^{(n+2)}}{(n+2)a^n}\right]\frac{dA}{dt} \tag{5A}$$

$$\text{Note: } \left[\frac{b^{(n+2)}-\left(\frac{a+b}{2}\right)^{(n+2)}}{n+2}\right] \longrightarrow \log\frac{2b}{a+b} \text{ as } n \longrightarrow -2$$

Differentiating Eqs. (4A) and (5A) with respect to time, and using the resulting equations together with Eq. (5A) to eliminate dB/dt and d^2B/dt^2 gives

$$C_5 \frac{d^2A}{dt^2} + C_6 \frac{dA}{dt} + C_7 = 0 \tag{6A}$$

where C_5, C_6, and C_7 are given with Eq. (2).

Equations such as (6A) have solutions in the form

$$A/T^* = C_3 \exp(m_1 t) + C_4 \exp(m_2 t) \tag{7A}$$

where C_3 and C_4 are arbitrary constants and m_1 and m_2 are roots of

$$C_5 m^2 + C_6 m + C_7 = 0 \tag{8A}$$

Equation (2) is the same as Eq. (8A).

Substituting the value of A given by Eq. (7A) into (5A) and integrating gives

$$\frac{B}{T^*} = C_{10}$$

$$-C_3 \exp(m_1 t)\left\{\frac{nk}{c\gamma m_1}\left(\frac{a+b}{2a}\right)^n\left[\frac{2}{b^2-\left(\frac{a+b}{2}\right)^2}\right] + \left(\frac{2}{n+2}\right)\left[\frac{b^{(n+2)}-\left(\frac{a+b}{2}\right)^{(n+2)}}{a^n b^2-\left(\frac{a+b}{2}\right)^2 a^n}\right]\right\}$$

$$-C_4 \exp(m_2 t)\left\{\frac{nk}{c\gamma m_2}\left(\frac{a+b}{2a}\right)^n\left[\frac{2}{b^2-\left(\frac{a+b}{2}\right)^2}\right] + \left(\frac{2}{n+2}\right)\left[\frac{b^{(n+2)}-\left(\frac{a+b}{2}\right)^{(n+2)}}{a^n b^2-\left(\frac{a+b}{2}\right)^2 a^n}\right]\right\} \tag{9A}$$

We know that initially T is zero for all values of r. Substituting (7A) and (9A) into (1A) and setting T = 0 and $\dot{t}$ = 0 gives

$$0 = C_{10} - C_3\left\{\frac{nk}{c\gamma m_1}\left(\frac{a+b}{2a}\right)^n\left[\frac{2}{b^2-\left(\frac{a+b}{2}\right)^2}\right] + \left(\frac{2}{n+2}\right)\left[\frac{b^{(n+2)} - \left(\frac{a+b}{2}\right)^{(n+2)}}{a^n b^2 - \left(\frac{a+b}{2}\right)^2 a^n}\right]\right\} - C_4\left\{\frac{nk}{c\gamma m_2}\left(\frac{a+b}{2a}\right)^n\left[\frac{2}{b^2-\left(\frac{a+b}{2}\right)^2}\right] + \left(\frac{2}{n+2}\right)\left[\frac{b^{(n+2)} - \left(\frac{a+b}{2}\right)^{(n+2)}}{a^n b^2 - \left(\frac{a+b}{2}\right)^2 a^n}\right]\right\} \quad (10A)$$

$$0 = C_3 + C_4 \quad (11A)$$

We know also that when t is very large, $T = T^*$. We will find that m_1 and m_2 are negative, so that when t is large, exp(mt) is zero. With (1A) then

$$C_{10} = 1 \quad (12A)$$

Combining Eqs. (10A), (11A) and (12A)

$$0 = 1 - C_3\left(\frac{a+b}{2a}\right)^n\left[\frac{2}{b^2-\left(\frac{a+b}{2}\right)^2}\right]\left(\frac{mk}{c\gamma}\right)\left(\frac{1}{m_1} - \frac{1}{m_2}\right) \quad (13A)$$

giving

$$C_3 = \left(\frac{m_1 m_2}{m_2 - m_1}\right)\left(\frac{c\gamma}{2nk}\right)\left[\frac{b^2-\left(\frac{a+b}{2}\right)^2}{\left(\frac{a+b}{2a}\right)^n}\right] = -C_4 \quad (14A)$$

Substituting (7A), (9A), (12A) and (14A) into (1A) gives Eq. (1), except for the factor (0.95). This factor was applied to force the solution to fit in somewhat better with Ref. 9. Without this factor, the curves for b/a = 1.1 and 1.3 in Fig. 61.5 would have fallen above the curve for b/a = 1.0, taken from Ref. 9. Applying a factor of 0.95 to C_3 and C_4 caused the curves for b/a = 1.1 and 1.3 to be lowered as shown in Fig. 61.5 In this position they "fall in" with the flat curve b/a = 1. Since coefficients C_1 and C_2 also deal with the transient heat flow phenomena, it was felt that the 0.95 factor should be applied to them also. Apparently requiring the temperature distribution to arbitrarily fit the form of Eq. (1A) with only two parameters, A and B, has introduced this 5 percent error. The solution has shown that changing b/a from 1.0 to 1.3 has only a small effect on the answers. This raises the question of using the results in Ref. 9 directly, neglecting curvature effects. This was not done, since a solution in the form of Eq. (1A) is particularly useful in subsequent stress and distortion computations, Section 42.

The temperature difference between the inner and outer flange surfaces is obtained by evaluating T_a and T_b at r = a and b, respectively, from Eq. (1) and forming their difference. The result is given in Eq. (3). To obtain the time at which the difference is a maximum, the derivative is set to zero. The resulting solution for the time of the maximum temperature difference is given in Eq. (4). Substituting the result into Eq. (3) gives Eq. (5). From Eq. (1A) it is evident that $A = (T_a - T_b)\left[a^n/(a^n - b^n)\right]$. Using this result in Eq. (5) gives Eq. (6)

We will now select n to give equality of heat flow through the film and at the inner face of the flange at the time given by Eq. (4). In equation form this is expressed by

$$h(T^* - T_a) = -k\left(\frac{dT}{dr}\right)_{r=a} \qquad \text{when } t = t_{(\text{max. diff.})} \tag{15A}$$

Substituting from Eq. (1) into this equation (neglecting the 0.95 factor for this purpose) gives

$$m_2 C_8 + \frac{m_2}{m_1} C_9 = m_1 C_8 + \frac{m_1}{m_2} C_9$$

where

$$C_8 = \left(1 - \frac{nk}{ah}\right) a^n - \left(\frac{2}{n+2}\right) \frac{\left[b^{(n+2)} - \left(\frac{a+b}{2}\right)^{(n+2)}\right]}{\left[b^2 - \left(\frac{a+b}{2}\right)^2\right]} \tag{16A}$$

$$C_9 = -\left(\frac{2nk}{c\gamma}\right) \frac{\left(\frac{a+b}{2}\right)^n}{\left[b^2 - \left(\frac{a+b}{2}\right)^2\right]}$$

Equation (16A) can be put in the form

$$\left(\frac{m_2 + m_1}{m_1 m_2}\right) = -\frac{C_8}{C_9} \tag{17A}$$

Likewise from Eq. 2 we know that

$$\left(\frac{m_2 + m_1}{m_1 m_2}\right) = -\frac{C_6}{C_7} \tag{18A}$$

Combining Eq. (17A) and (18A) and solving for n gives

$$n = \frac{\log\left(\frac{a + 3b}{4a + 4b}\right)}{\log\left(\frac{a + b}{2a}\right)}$$

This is the value of n given with Eq. (1) and in Fig. 61.1

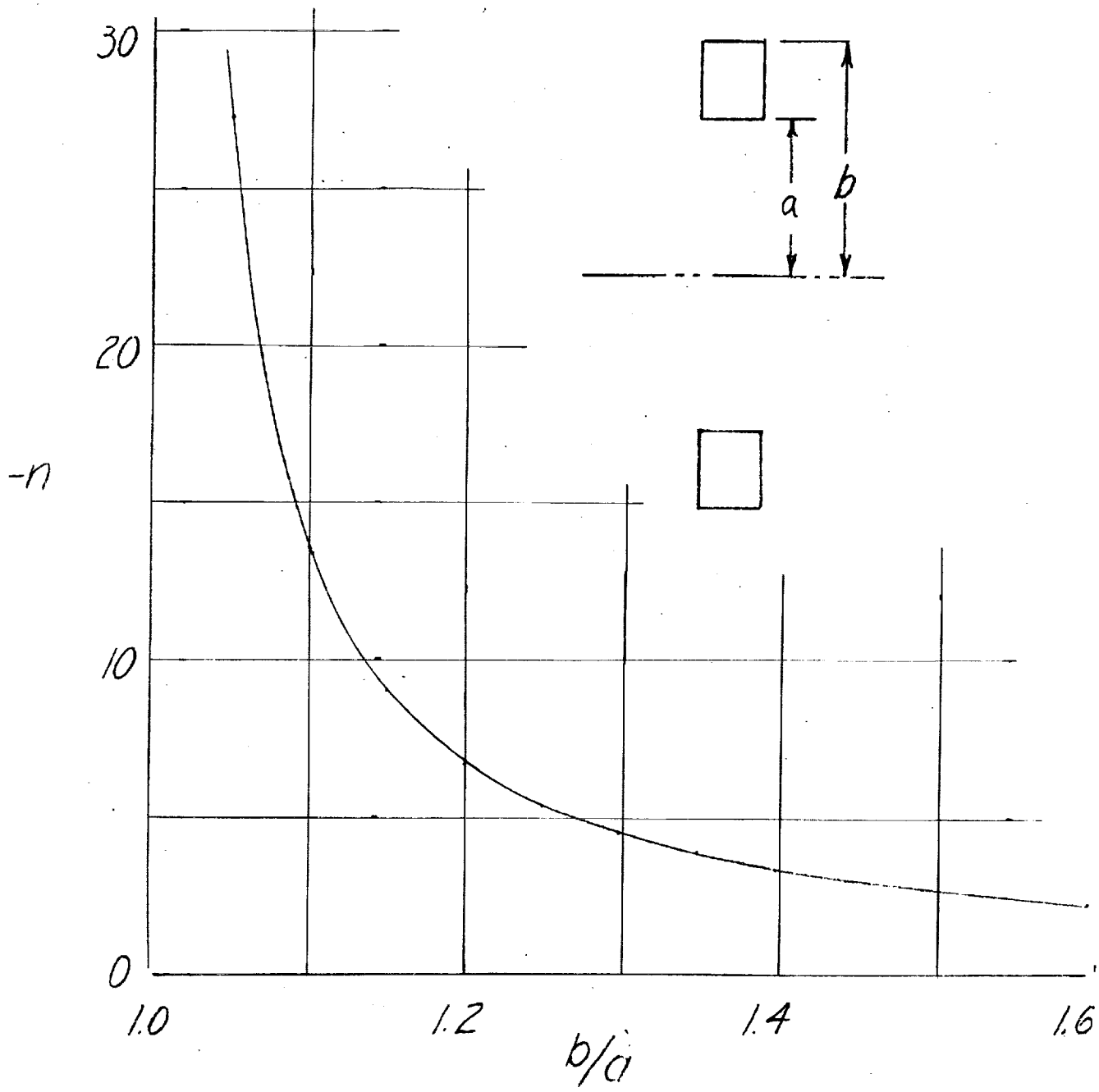

Fig. 61.1 Variation of exponent n with ratio of outer to inner radius, b/a

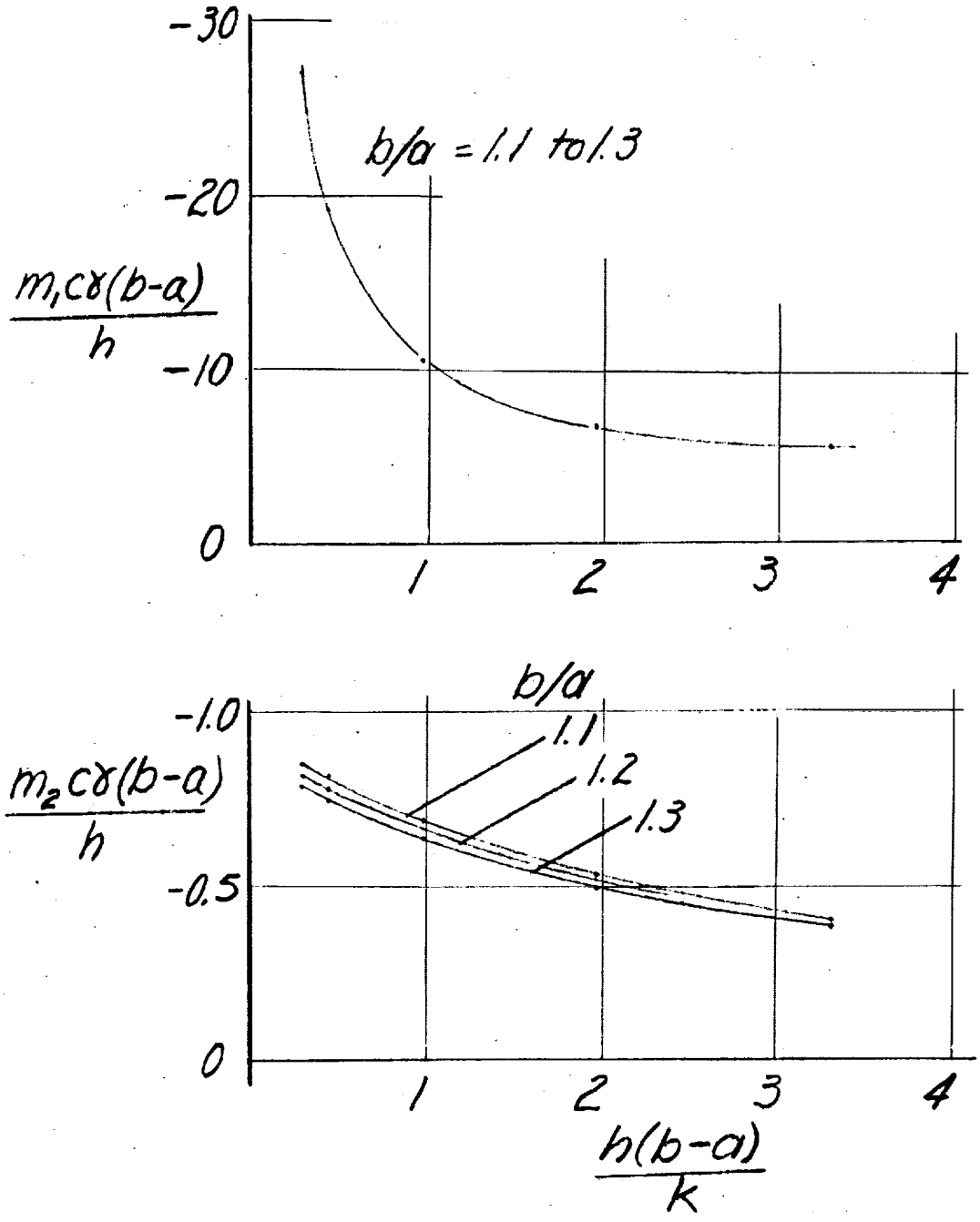

Fig. 61.2 Variation of dimensionless exponents m_1 and m_2 with dimensionless film coefficient for a range of ratios of outer to inner radius

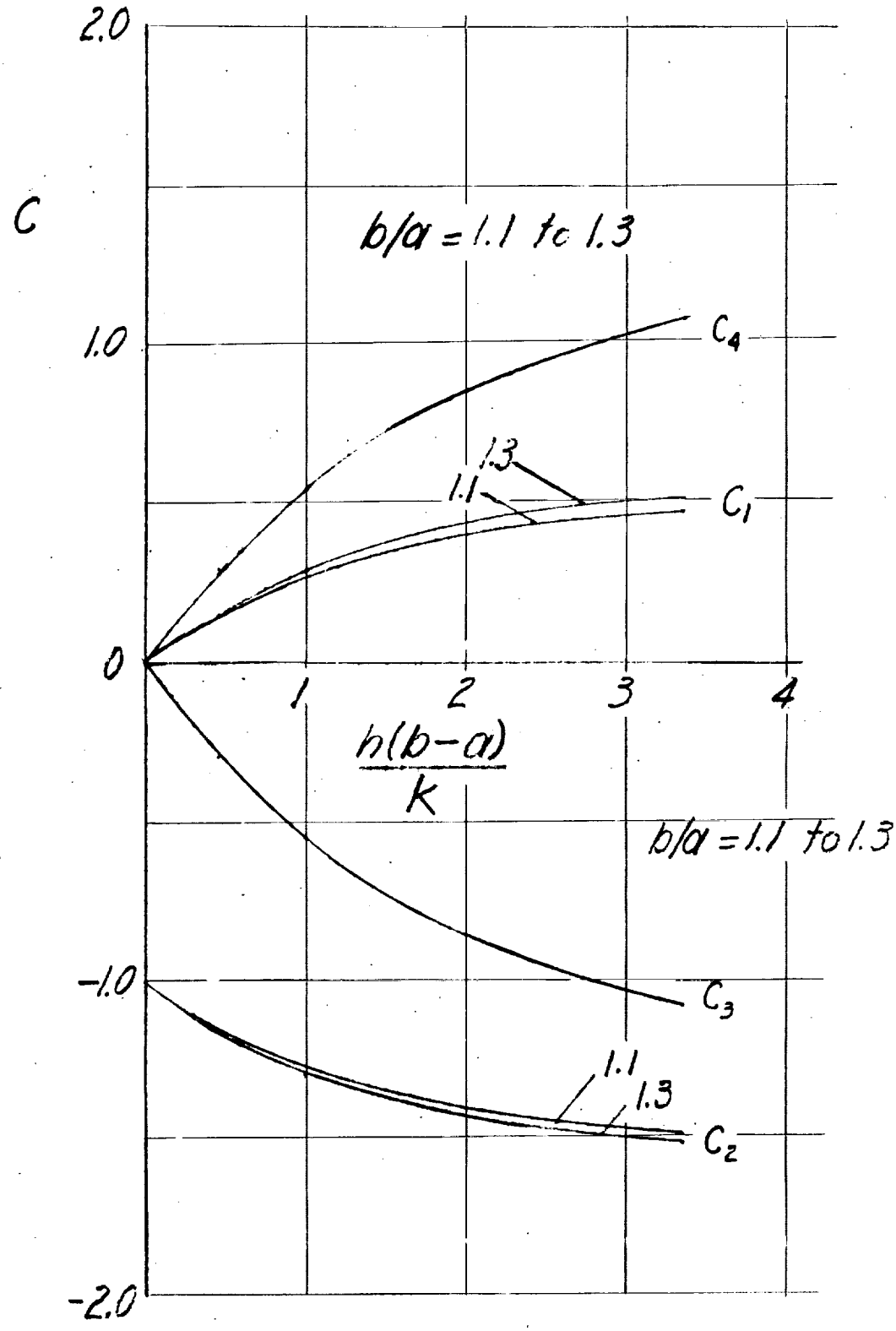

Fig. 61.3 Variation of C with dimensionless film coefficient for a range of radius ratios, b/a

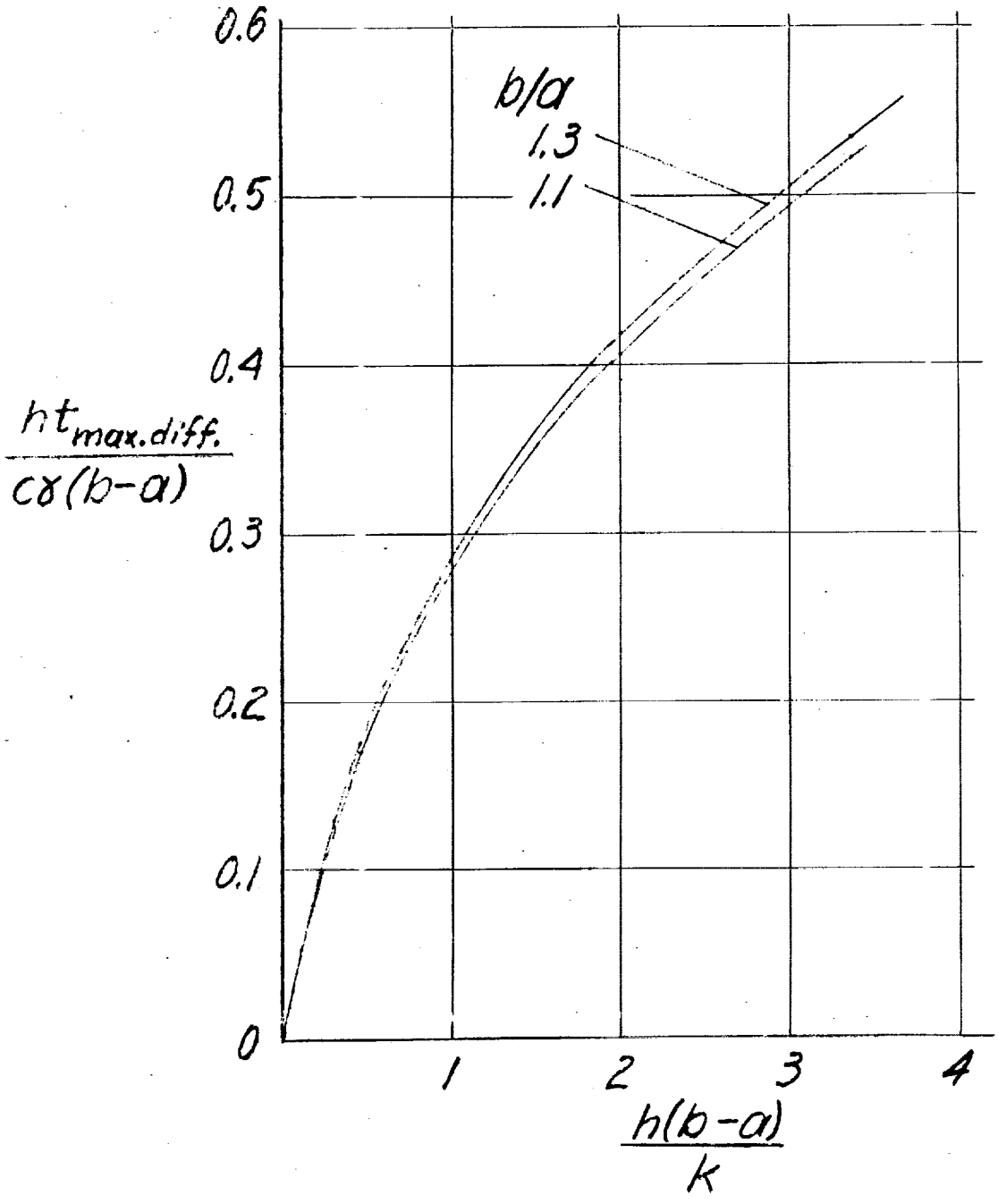

Fig. 61.4 Dimensionless time of maximum temperature difference

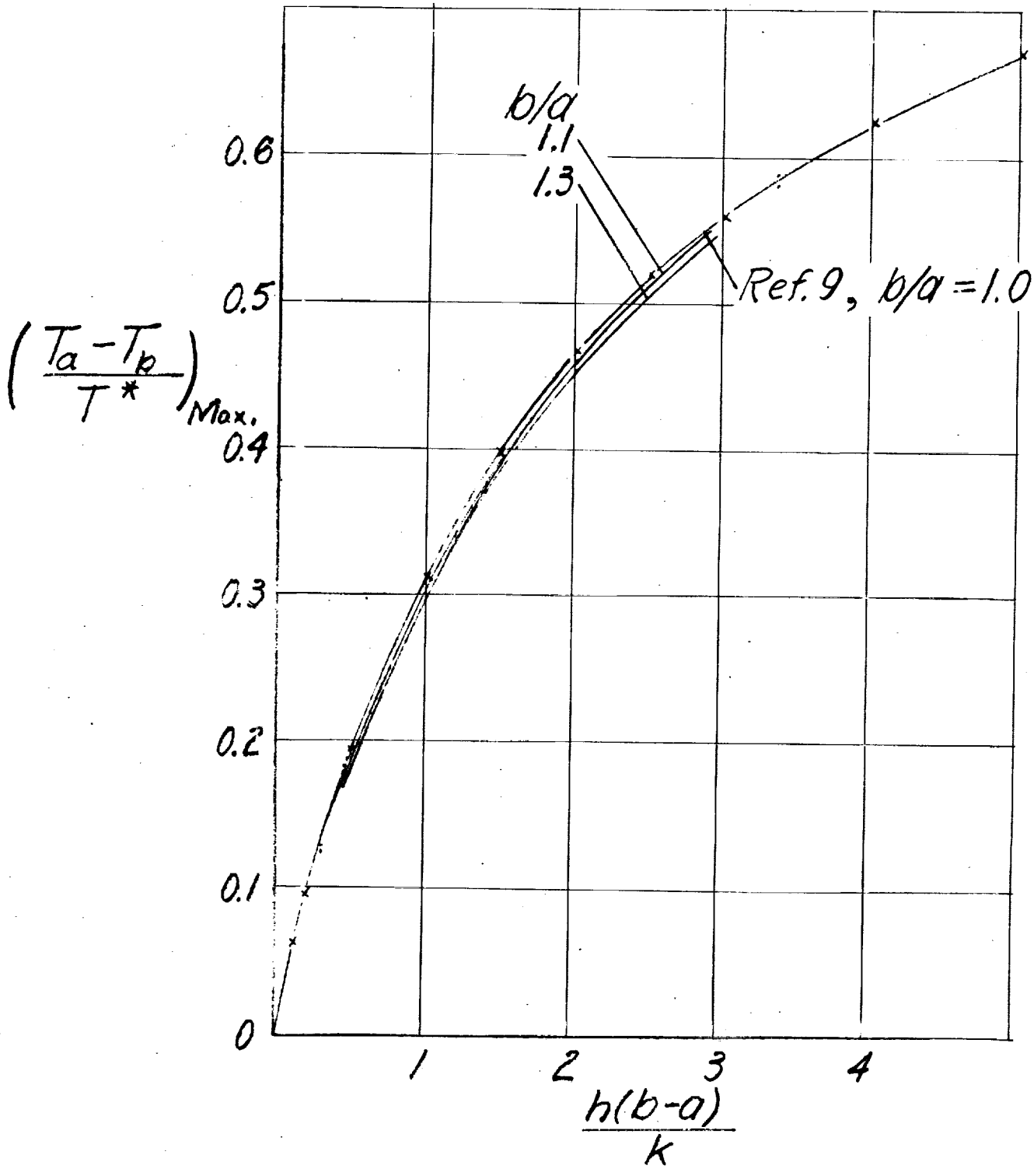

Fig. 61.5. Dimensionless maximum temperature difference

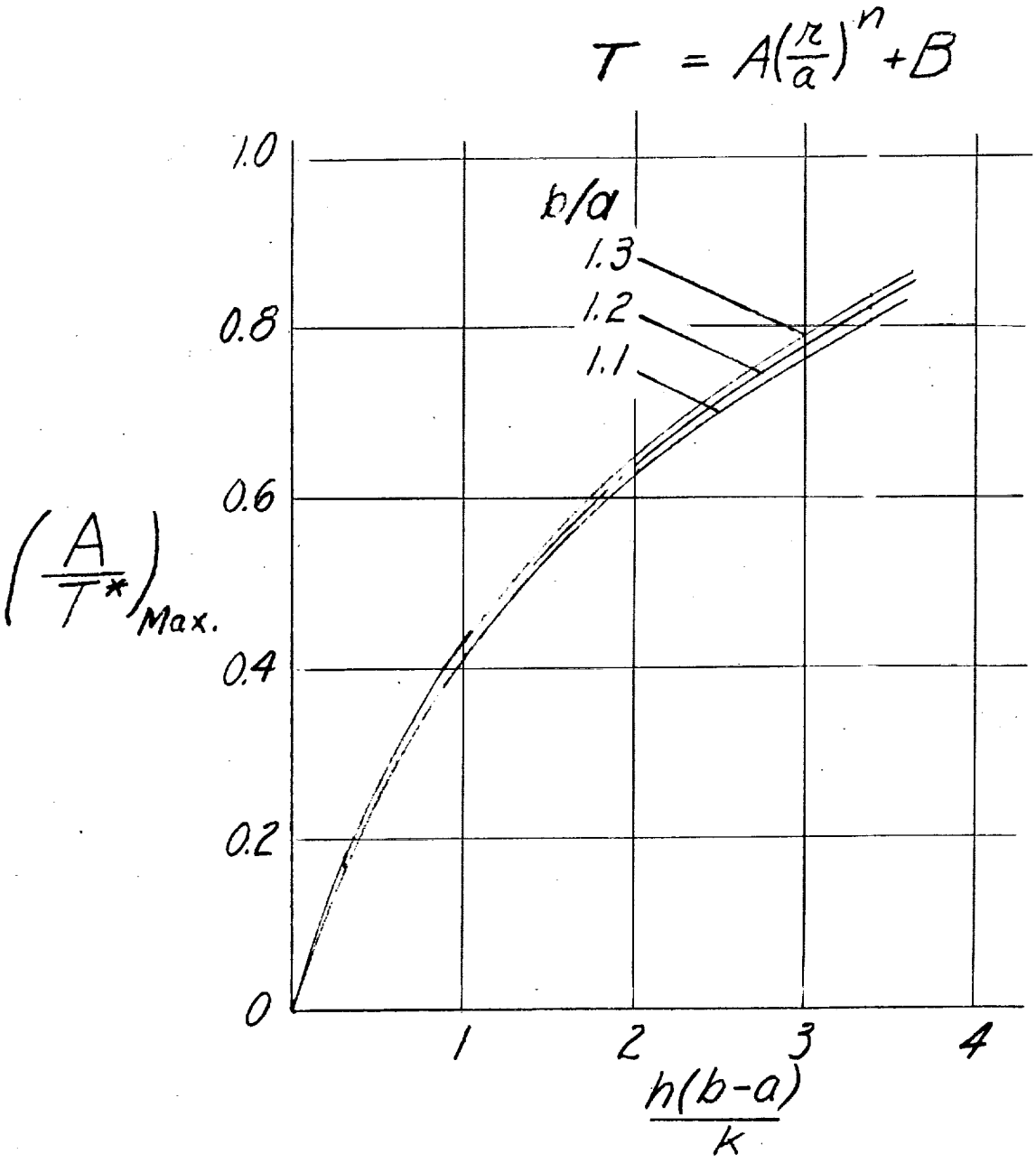

Fig. 61.6. Maximum value of A/T^*, dimensionless factor in temperature function .

61.3 Temperature Transients in Bolts (by L.H. Tomlinson)

61.3.1 Introduction

Knowledge of the temperature transients in the connector bolts is necessary in order to determine the changes in stress and strain in the bolt and the overall effect on the connector. In the case of a sharp and large heating transient in the connector, it may be possible to actually overstress the bolt and put a permanent set in it before it has had a chance to come up to temperature.

In the case of a sharp and large cooling transient, it may be possible to release all bolt loading on the connector before the bolt gets a chance to come to temperature equilibrium.

Determination of the actual temperature transient in the bolt in relation to the fluid transient is quite complex and requires considerable mathematical effort, preferably on a computer. Efforts of this nature will not be covered here at this time, however. Instead, some simplified methods of looking at the problem will be discussed.

Considering the bolt shown in Fig. 61.7 one assumption that may be made is that there is no heat transfer between the bolt and the connector other than by contact with the bolt head and nut. At room temperatures and below, this is very nearly true, as the convection coefficient around the bolt will be only 2 or 3 Btu/hr.ft.^{2} $^\circ$F and the radiation coefficient will be negligible. At high temperatures the coefficients can be considerably higher and might run as high as 20-40 Btu/hr.ft.^{2} $^\circ$F for connectors carrying hot combustion gases.

Accepting the simplifying assumption of only lengthwise heat flow in the bolt, one may look upon the bolt as merely a small section of an infinite flat plate and apply some of the already available thermal transient information to certain cases. In order to get a rough picture of what the thermal transients may look like, Fig. 61.8 was included. This graph was drawn originally to show the temperature transients occurring in flange SK20-1286A (sketched in Fig. 61.7) with liquid oxygen as the fluid and a heat transfer coefficient at the fluid-wall interface of 2000 Btu/hr.ft.^{2} $^\circ$F. This curve was drawn from flat plate data in Ref. 1 and Ref. 2 using dimensionless numbers containing the thermal constants of stainless steel and aluminum, the dimensions of Fig. 61.7 and the above mentioned h of 2000 Btu/hr.ft.^{2} $^\circ$F.

FIG. 61.7

CROSS SECTION OF
BOLT AND FLANGE CONFIGURATION
SIMILAR TO SK 20-1286A

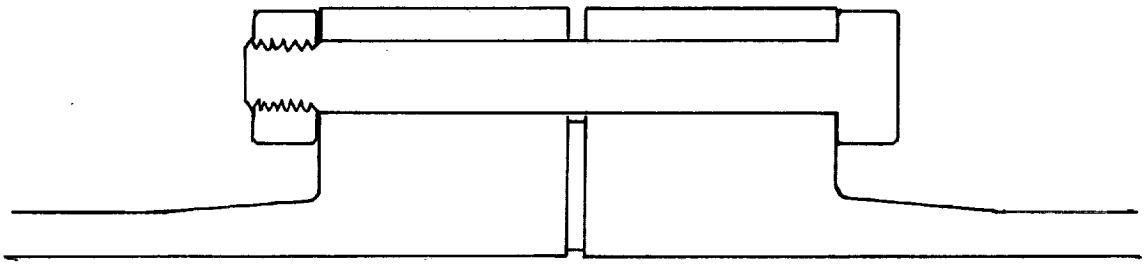

Scale 1 to 1

32

Fig. 61.8 TEMPERATURE - TIME HISTORY of FLANGE of Fig. 61.7 for h = 2000 Btu/hr ft^2 ^{o}F

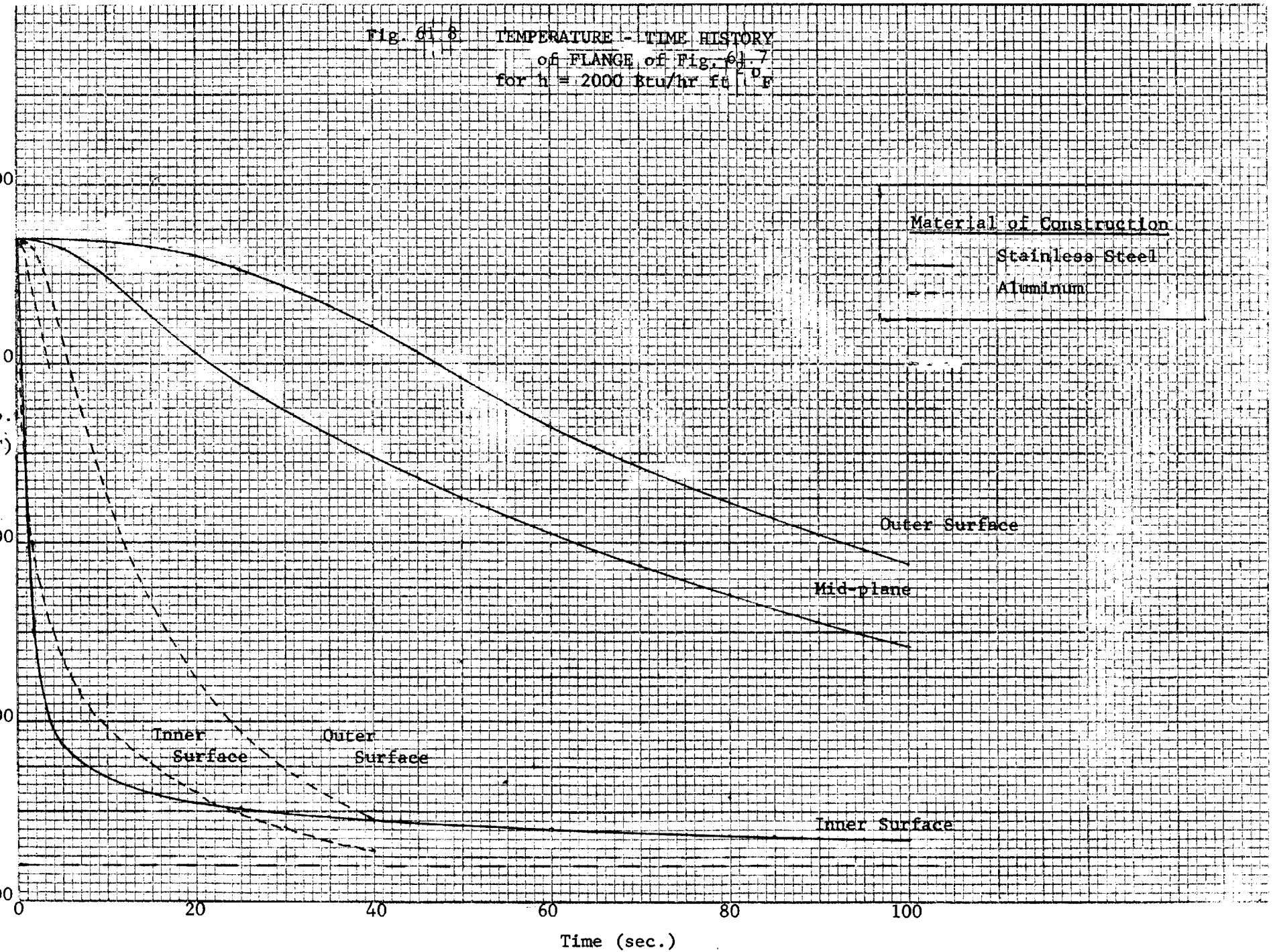

1.3.2 Thermal Resistance at Contact Points

Before we can even use the curves of Fig. 61.8 as approximations for some cases, we must discuss the matter of the contact resistance at the bolt head and nut. Because contact resistance is quite dependent on surface finish as well as on material and the pressure on the joint, only general approximations can be given here. Fig. 61.9 shows some curves (from Refs. 10 and 11) that should apply reasonably well. These data apply to surface roughnesses in the range of 50-100 microinches, which is equivalant to a fairly ordinary machining job that might be done on a flange or bolt. Certainly it would be unreasonable to expect contact surfaces on bolts and flanges to possess a high degree of flatness and a smoothness on the order of 10 microinches or less.

It will be noted that the hardest pair of surfaces, steel on steel, exhibit the lowest thermal conductance at the contact area. Both stainless steel on aluminum and aluminum on aluminum show much higher thermal conductances due to the much greater tendency of the softer materials to deform locally at their scattered points of contact and increase the area of actual physical contact as pressure is increased. Sometimes as the pressure is raised very high, very considerable amounts of plastic flow occur, even in steel, and the resulting high thermal conduction is retained down to very low pressures.

A point to note, especially at lower conductances, is that at the nut end of the bolt there are two resistances in series.

Fig. 61.9 Thermal Conductivity of
Dry Joints in Air

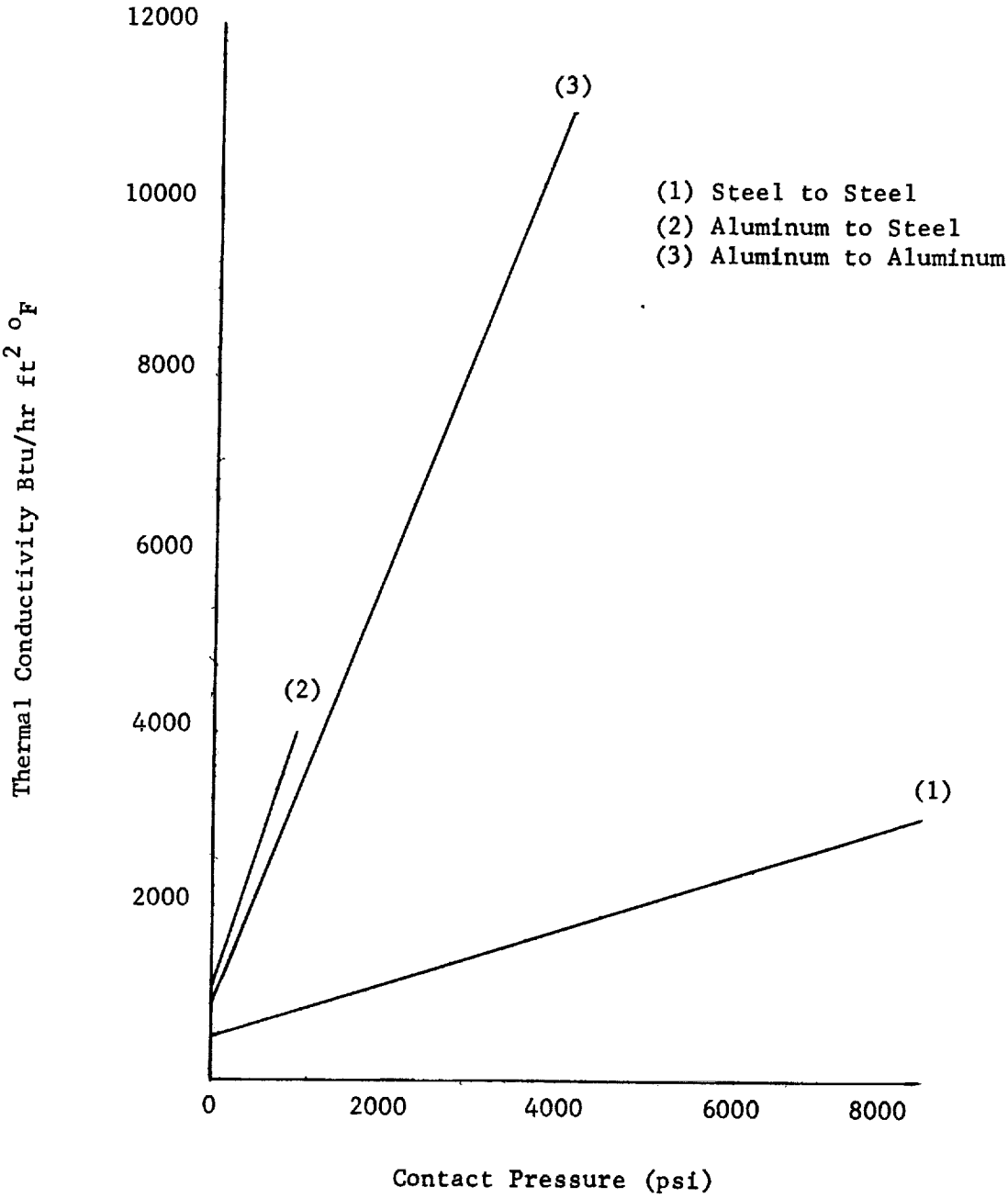

61.3.3 Examples

It will be shown how flat-plate data may be used for getting rough estimates of temperature transients in symetrically heated bolts. It should be kept in mind while using flat-plate data from Ref. 1, pp. 33-34, and Ref. 9 or while referring to Fig. 61.8 that the following terms are equivalents:

Flange outer surface=Bolt center=Flat plate midplane
Flange inner surface=Bolt ends=Flat plate outer surfaces
Flange midplane=1/4 way thru bolt=1/4 way thru flat plate

The reasons for these terms being equivalent may be seen by considering the following facts:

1. Heat flow into the infinite flat plate is from both sides and at the midplane there is no heat flow.

2. Heat flow into the flange is from one side but the outside is considered insulated and there is essentially no heat flow thru the outer boundary.

3. Heat flow into the bolts is limited arbitrarily in our cases to symetrical flow from both ends. Thus there is no heat flow thru the center of the bolt.

It can be seen therefore that the heat flow through the flange is equivalent to heat flow through one-half the thickness of the flat plate or through one half the length of the bolt.

(a) First case - Stainless steel bolt as per Fig. 61.7
Stainless steel flanges as per Fig. 61.7

Assume a contact surface pressure of about 7,000 psi, producing thermal surface conductance of about 2000 Btu/hr. ft.^{2} $^\circ$F. For a first look at the bolt, we could assume that the temperature of the flange had changed instantly. Than both halves of the bolt would exhibit temperature transients as in Fig. 61.8 with the center of the bolt being equivalent to the curve labeled "outer surface". It is evident that at this rate, 100 seconds will elapse before the center of the bolt comes down even halfway in temperature and much longer before the bolt as a whole comes close to the final temperature.

Since the assumption of instantaneous temperature change in the flange is certainly not correct, it is well to take a look at what actually happens. It will be noted from Fig. 61.8 that the point at which the bolt contacts the flange (about 3/4 of the way out) really follows a temperature curve rather closer to the outer surface than the midplane. This, then, is the initial temperature applied, thru the contact resistance, to the bolt head or nut. Obviously the temperatures in the bolt will take even longer than previously estimated to react to the initial fluid temperature change. A good estimate might be 2.5 minutes for the center of the bolt to come down halfway in temperature.

(b) Second case - Aluminum bolt as per Fig. 61.7
- Aluminum flange as per Fig. 61.7

Assume a modest contact surface pressure to produce a thermal surface conductance of about 2000 Btu/hr.ft.^{2}.$^\circ$F. Actually, though, higher thermal conductivities are not going to alter greatly the answers arrived at here. Again making a temporary assumption that the flange temperature changes instantly, it becomes evident from Fig.61.8 that the center of the bolt will be halfway down in temperature in about 14 seconds. If the actual rate of change in flange temperature is taken into account, it is estimated that it will take about 25 seconds for the center of the bolt to drop halfway in temperature.

Other more complex cases, where flanges of different materials are used, will not be discussed here, as even rough estimates of temperatures in the bolts will be difficult and hardly worthwhile.

FIG. 61-10 GRAPH FOR DETERMINATION OF MAXIMUM TEMPERATURE DIFFERENCE ACROSS FLANGE

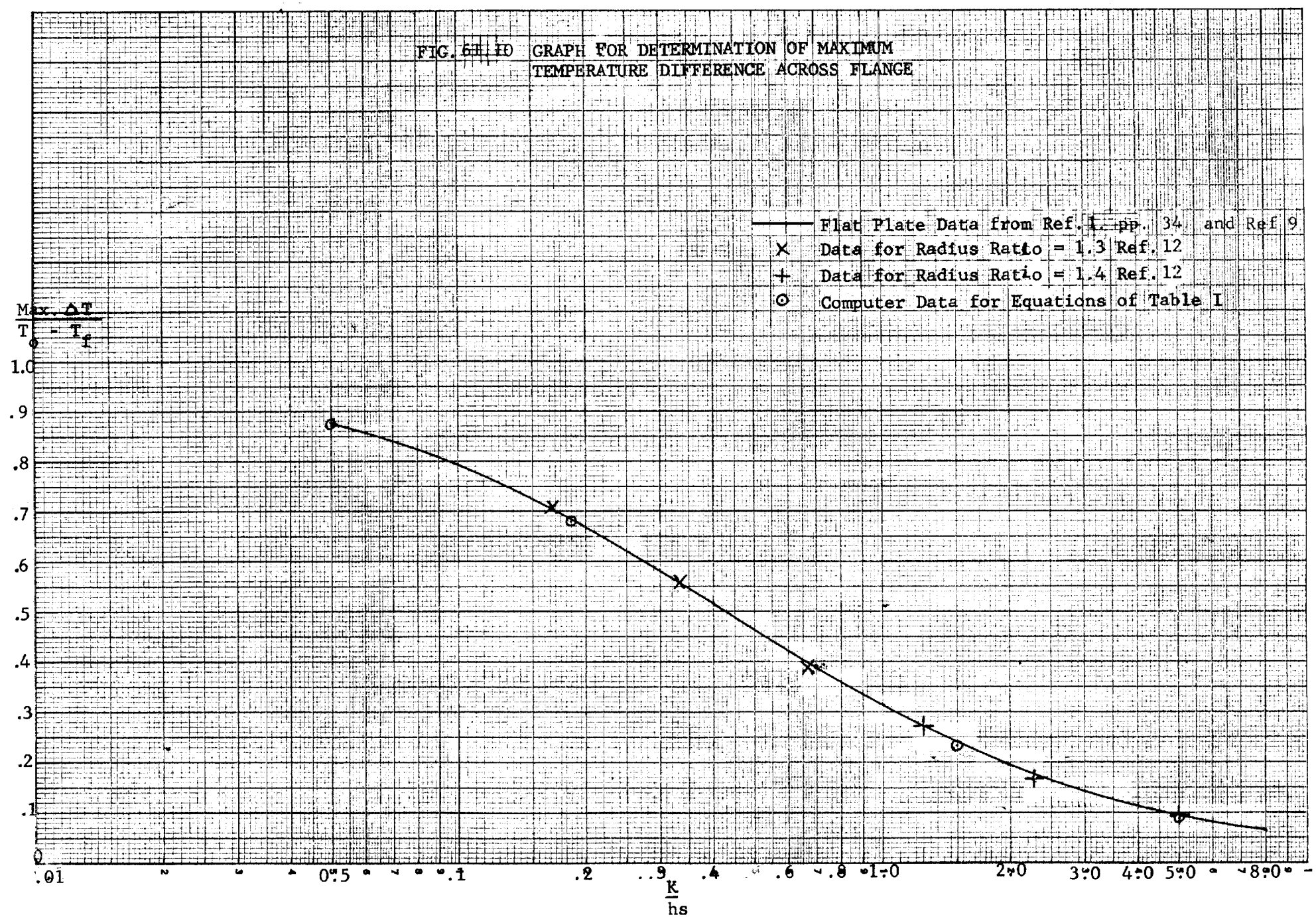

61.4 Temperature Transient Analysis in Flange Assemblies (by L.H. Tomlinson)

61.4.1 Preliminary Computer Efforts

Sections 61.2 and 61.3 present information on temperature transients for plain flanges and for flange bolts in certain simplified cases. There is a need for some knowledge of the thermal transients in more complex assemblies, however. This could cover combinations of flanges, bolts, spacers, and sometimes, gaskets of various materials in the same assembly.

One question that needed to be answered was whether or not the flanges could be considered as sections of flat plates due to their relatively low profiles or low radius ratios. Ref. 12 gives data on thermal transients in cylinders, and some of it lies in the range in which we are interested. Fig. 61.10 presents a curve plotted from flat plate data given in Refs. 1, pp. 33-34, and Ref. 9. Data from Ref. 12 for radius ratios of 1.3 and 1.4 are plotted on Fig. 61.10 and it will be noted that the points fall very close to the curve for flat plate transients. The conclusion to be drawn is that we may consider our low profile flanges of radius ratio 1.1 to 1.3 to be sections of flat plate.

As a test, a section of flange or plate was divided into nodes as shown in Fig. 61.11 and the dimensionless heat transfer equations of Tables I and II were derived. A very brief description of their writing follows. A heat balance equation is written for the node "a" as the generalized example following shows:

$$A\,(t_b - t_a) + B\,(t_c - t_a) + \frac{C\,(t_a - t'_a)}{\Delta T} = 0$$

This equation is written with so-called "forward time steps" wherein all the temperatures t_n are known for the beginning of the time step and only one temperature t'_n of the node itself is unknown and therefore readily solved for. The other way of writing the equation with "backward time steps" is as follows:

$$A\,(t'_b - t'_a) + B\,(t'_c\ t'_a) + \frac{C\,(t'_a - t_a)}{\Delta T} = 0$$

Here there is only one known t_a and the rest unknown. This results in a matrix of unknowns to solve for each time step. This latter method is inherently a much more accurate one but it is very time consuming to solve a matrix each time. The use of "forward time steps" avoids this difficulty but introduces possible error because of the assumption that

$$\frac{(t_a - t'_1)}{\Delta T}$$

is constant throughout the time interval. Since there is usually more or less curvature to the function the only way to keep error down is to make the time interval (ΔT) quite small. It was decided to try "forward time steps" since there could be considerable savings in computer time and in programming if the time steps did not have to be extremely small. The equations of Table I were made dimensionless by appropriate manipulation of the constants involved. Trial solutions were run on these equations using time steps of one-tenth of a second and printouts every second but these solutions proved

to be somewhat in error. Selection of a time step of one hundredth of a second with a printout of data every second gave results of quite satisfactory accuracy with only a small increase in computer time (to a little over 5 minutes on the GE 225).

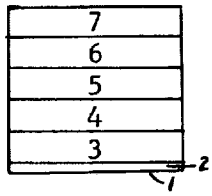

FIGURE 61.11

Division of thickness into nodes for step-by-step numerical solution

It should be noted here that Ref. 13 contains a very good description of the methods being used here. Pages 19 and 20 of this reference have some especially pertinent comments concerning time steps.

TABLE I

Equations for Simple Flat Plate Representation of Flange
(written in completely dimensionless form)

1. $$R_1' = \frac{1}{1 + A'} + \left[\frac{A'}{1 + A'}\right] R_2'$$

2. $$R_2' = \frac{A\Delta T}{C(1+A')} - \left[\frac{A\Delta T}{C(1+A')} + \frac{B\Delta T}{C} - 1\right] R_2 + \frac{B\Delta T}{C} R_3$$

3. $$R_3' = \frac{B\Delta T}{E} R_2 - \left[\frac{B\Delta T}{E} + \frac{D\Delta T}{E} - 1\right] R_3 + \frac{D\Delta T}{E} R_4$$

4. $$R_4' = \frac{D\Delta T}{G} R_3 - \left[\frac{D\Delta T}{G} + \frac{F\Delta T}{G} - 1\right] R_4 + \frac{F\Delta T}{G} R_5$$

5. $$R_5' = \frac{F\Delta T}{I} R_4 - \left[\frac{F\Delta T}{I} + \frac{H\Delta T}{I} - 1\right] R_5 + \frac{H\Delta T}{I} R_6$$

6. $$R_6' = \frac{H\Delta T}{L} R_5 - \left[\frac{H\Delta T}{L} + \frac{J\Delta T}{L} - 1\right] R_6 + \frac{J\Delta T}{L} R_7$$

7. $$R_7' = \frac{J\Delta T}{M} R_6 - \left[\frac{J\Delta T}{M} - 1\right] R_7$$

TABLE II

Definition of Terms Used in Equations of TABLE I

R_n = Known dimensionless temperature at beginning of time step $(\frac{t_o - t}{t_o - t_f})$

R_n' = Unknown dimensionless temperature at end of time step $(\frac{t_o - t'}{t_o - t_o})$

ΔT = time step in seconds

A = 40

A' = $40 \frac{K}{hs}$

B = 10

C = $0.05 \frac{\rho c s^2}{k}$

D = 5.71

E = $0.15 \frac{\rho c s^2}{k}$

F = 5

G = $0.2 \frac{\rho c s^2}{k}$

H = 5

I = $0.2 \frac{\rho c s^2}{k}$

J = 5

L = $0.2 \frac{\rho c s^2}{k}$

M = $0.2 \frac{\rho c s^2}{k}$

K	=	thermal conductivity of flange material	BTU/hr.ft.^oF
ρ	=	density of flange	lb/ft^3
c	=	specific heat of flange material	BTU/lb^oF
s	=	radial thickness of flange	ft
h	=	heat transfer coefficient of fluid at surface	BTU/hr.$ft^{2o}F$

FIGURE 61.12

Bolt & Flange Assembly
(cross section)

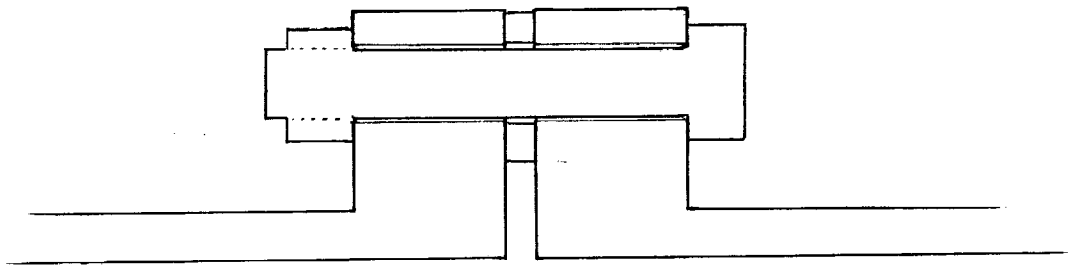

Nodes
(Flanges & Spacer)

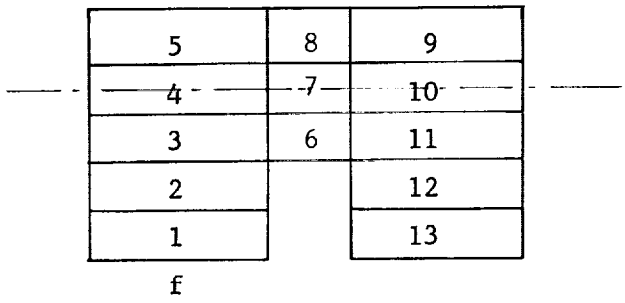

Nodes
(Bolt)

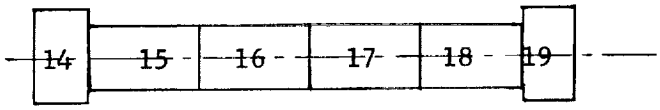

61.4.2 General Equations for Computer Solution of Flange Assembly Temperature Transients

Fig.61.12 shows a combination of flanges, bolt and spacer each of which may be a different material. The nodal structure chosen is also shown. Heat balance equations were written for each node and the general equations of Tables III and IV obtained. These equations are non-dimensional only in temperature in order to make substitution of different materials and dimensions of flanges easier.

It would be appropriate at this time to comment on why the flanges are left disconnected from the pipe in this analysis. Actually for most cases of cryogenic fluid flow the fluid heat transfer coefficient is so high that the pipe wall makes a rather ineffective fin for the flange. For those cases where the fluid heat transfer coefficient is not very high (perhaps under 500 BTU/hr.ft^2 ^{o}F) an additional node will have to be introduced to represent a piece of pipe wall.

41

TABLE III

Equations Written for Flange & Bolt Assembly of Figure 61.12

1. $$R_1' = \left[\frac{Z_{f1}\Delta T}{S_1}\right] R_f - \left[\frac{(Z_{f1}+Z_{21})\Delta T}{S_1} - 1\right] R_1 + \left[\frac{Z_{21}\Delta T}{S_1}\right] R_2$$

2. $$R_2' = \left[\frac{Z_{12}\Delta T}{S_2}\right] R_1 - \left[\frac{(Z_{12}+Z_{32})\Delta T}{S_2} - 1\right] R_2 + \left[\frac{Z_{32}\Delta T}{S_2}\right] R_3$$

3. $$R_3' = \left[\frac{Z_{23}\Delta T}{S_3}\right] R_2 - \left[\frac{(Z_{23}+Z_{43}+Z_{63})\Delta T}{S_3} - 1\right] R_3 + \left[\frac{Z_{43}\Delta T}{S_3}\right] R_4 + \left[\frac{Z_{63}\Delta T}{S_3}\right] R_6$$

4. $$R_4' = \left[\frac{Z_{34}\Delta T}{S_4}\right] R_3 - \left[\frac{(Z_{34}+Z_{54}+Z_{74})\Delta T}{S_4} - 1\right] R_4 + \left[\frac{Z_{54}\Delta T}{S_4}\right] R_5 + \left[\frac{Z_{74}\Delta T}{S_4}\right] R_7 + \left[\frac{Z_{14\text{-}4}\Delta T}{S_4}\right] R_{14}$$

5. $$R_5' = \left[\frac{Z_{45}\Delta T}{S_5}\right] R_4 - \left[\frac{(Z_{45}+Z_{85})\Delta T}{S_5} - 1\right] R_5 + \left[\frac{Z_{85}\Delta T}{S_5}\right] R_8$$

6. $$R_6' = \left[\frac{Z_{36}\Delta T}{S_6}\right] R_3 - \left[\frac{(Z_{36}+Z_{76}+Z_{11\text{-}5})\Delta T}{S_6} - 1\right] R_6 + \left[\frac{Z_{76}\Delta T}{S_6}\right] R_7 + \left[\frac{Z_{11\text{-}6}\Delta T}{S_6}\right] R_{11}$$

7. $$R_7' = \left[\frac{Z_{47}\Delta T}{S_7}\right] R_4 + \left[\frac{Z_{67}\Delta T}{S_7}\right] R_6 - \left[\frac{(Z_{47}+Z_{67}+Z_{87}+Z_{10\text{-}7})\Delta T}{S_7} - 1\right] R_7 + \left[\frac{Z_{87}\Delta T}{S_7}\right] R_8 + \left[\frac{Z_{10\text{-}7}\Delta T}{S_7}\right] R_{10}$$

8. $$R_8' = \left[\frac{Z_{58}\Delta T}{S_8}\right] R_5 + \left[\frac{Z_{78}\Delta T}{S_8}\right] R_7 - \left[\frac{(Z_{58}+Z_{78}+Z_{98})\Delta T}{S_8} - 1\right] R_8 + \left[\frac{Z_{98}\Delta T}{S_8}\right] R_9$$

9. $$R_9' = \left[\frac{Z_{89}\Delta T}{S_9}\right] R_8 - \left[\frac{(Z_{89}+Z_{10\text{-}9})\Delta T}{S_9} - 1\right] R_9 + \left[\frac{Z_{10\text{-}9}\Delta T}{S_9}\right] R_{10}$$

10. $$R_{10}' = \left[\frac{Z_{7\text{-}10}\Delta T}{S_{10}}\right] R_7 + \left[\frac{Z_{9\text{-}10}\Delta T}{S_{10}}\right] R_9 - \left[\frac{(Z_{7\text{-}10}+Z_{9\text{-}10}+Z_{11\text{-}10})\Delta T}{S_{10}} - 1\right] R_{10} + \left[\frac{Z_{11\text{-}10}\Delta T}{S_{10}}\right] R_{11} + \left[\frac{Z_{19\text{-}10}\Delta T}{S_{10}}\right] R_{19}$$

11. $$R'_{11} = \left[\frac{Z_{6-11}\Delta T}{S_{11}}\right] R_6 + \left[\frac{Z_{10-11}\Delta T}{S_{11}}\right] R_{10} - \left[\frac{(Z_{6-11}+Z_{10-11}+Z_{12-11})\Delta T}{S_{11}} - 1\right] R_{11} + \left[\frac{Z_{12-11}\Delta T}{S_{11}}\right] R_{12}$$

12. $$R'_{12} = \left[\frac{Z_{11-12}\Delta T}{S_{12}}\right] R_{11} - \left[\frac{(Z_{11-12}+Z_{13-12})\Delta T}{S_{12}}\right] R_{12} + \left[\frac{Z_{13-12}\Delta T}{S_{12}}\right] R_{13}$$

13. $$R'_{13} = \left[\frac{Z_{f13}\Delta T}{S_{13}}\right] R_f + \left[\frac{Z_{12-13}\Delta T}{S_{13}}\right] R_{12} - \left[\frac{(Z_{f13}+Z_{12-13})\Delta T}{S_{13}} - 1\right] R_{13}$$

14. $$R'_{14} = \left[\frac{Z_{4-14}\Delta T}{S_{14}}\right] R_4 - \left[\frac{(Z_{4-14}+Z_{15-14})\Delta T}{S_{14}} - 1\right] R_{14} + \left[\frac{Z_{15-14}\Delta T}{S_{14}}\right] R_{15}$$

15. $$R'_{15} = \left[\frac{Z_{14-15}\Delta T}{S_{15}}\right] R_{14} - \left[\frac{(Z_{14-15}+Z_{16-15})\Delta T}{S_{15}} - 1\right] R_{15} + \left[\frac{Z_{16-15}\Delta T}{S_{15}}\right] R_{16}$$

16. $$R'_{16} = \left[\frac{Z_{15-16}\Delta T}{S_{16}}\right] R_{15} - \left[\frac{(Z_{15-16}+Z_{17-16})\Delta T}{S_{16}} - 1\right] R_{16} + \left[\frac{Z_{17-16}\Delta T}{S_{16}}\right] R_{17}$$

17. $$R'_{17} = \left[\frac{Z_{16-17}\Delta T}{S_{17}}\right] R_{16} - \left[\frac{(Z_{16-17}+Z_{18-17})\Delta T}{S_{17}} - 1\right] R_{17} + \left[\frac{Z_{18-17}\Delta T}{S_{17}}\right] R_{18}$$

18. $$R'_{18} = \left[\frac{Z_{17-18}\Delta T}{S_{18}}\right] R_{17} - \left[\frac{(Z_{17-18}+Z_{19-18})\Delta T}{S_{18}} - 1\right] R_{18} + \left[\frac{Z_{19-18}\Delta T}{S_{18}}\right] R_{19}$$

19. $$R'_{19} = \left[\frac{Z_{10-19}\Delta T}{S_{19}}\right] R_{10} + \left[\frac{Z_{18-19}\Delta T}{S_{19}}\right] R_{18} - \left[\frac{(Z_{10-19}+Z_{18-19})\Delta T}{S_{19}} - 1\right] R_{19}$$

TABLE IV

Definition of Terms in TABLE III

$$Z_n = U_n A_n$$

$$Z_{f1} = \frac{A_{f1}}{\frac{1}{h_f} + \frac{\ell 1}{K_1}}$$

$$Z_{12} = \frac{K_{12} A_{12}}{\ell_{12}}$$

$$Z_{23} = \frac{K_{23} A_{23}}{\ell_{23}}$$

$$Z_{34} = \frac{K_{34} A_{34}}{\ell_{34}}$$

$$Z_{45} = \frac{K_{45} A_{45}}{\ell_{45}}$$

$$Z_{36} = \frac{A_{36}}{\frac{1}{h_6} + \frac{\ell 36}{K_{36}}}$$

$$Z_{47} = \frac{A_{47}}{\frac{1}{h_c} + \frac{\ell 47}{K_{47}}}$$

$$Z_{58} = \frac{A_{58}}{\frac{1}{h_c} + \frac{\ell 58}{K_{58}}}$$

$$Z_{89} = \frac{A_{89}}{\frac{1}{hc} + \frac{\ell 9}{K_9} + \frac{\ell 8}{K_8}}$$

$$Z_{7\text{-}10} = \frac{A_{7\text{-}10}}{\frac{1}{h_c} + \frac{\ell 7}{K_7} + \frac{\ell 10}{K_{10}}}$$

$$Z_{6\text{-}11} = \frac{A_{6\text{-}11}}{\frac{1}{h_c} + \frac{\ell 6}{K_6} + \frac{\ell 11}{K_{11}}}$$

$$Z_{9\text{-}10} = \frac{K_{9\text{-}10} A_{9\text{-}10}}{\ell_{9\text{-}10}}$$

$$Z_{10\text{-}11} = \frac{K_{10\text{-}11} A_{10\text{-}11}}{\ell_{10\text{-}11}}$$

$$Z_{11\text{-}12} = \frac{K_{11\text{-}12} A_{11\text{-}12}}{\ell_{11\text{-}12}}$$

$$Z_{12\text{-}13} = \frac{K_{12\text{-}13} A_{12\text{-}13}}{\ell_{12\text{-}13}}$$

$$Z_{f13} = \frac{A_{f13}}{\frac{1}{h_f} + \frac{\ell 13}{K_{13}}}$$

$$Z_{4\text{-}14} = \frac{A_{4\text{-}14}}{\frac{1}{h_c} + \frac{\ell 4}{K_4}}$$

$$Z_{14\text{-}15} = \frac{K_{14\text{-}15} A_{14\text{-}15}}{\ell_{14\text{-}15}}$$

$$Z_{15\text{-}16} = \frac{K_{15\text{-}16} A_{15\text{-}16}}{\ell_{15\text{-}16}}$$

$$Z_{16\text{-}17} = \frac{K_{16\text{-}17} A_{16\text{-}17}}{\ell_{16\text{-}17}}$$

TABLE IV
(continued)

$$Z_{17-18} = \frac{K_{17-18}\, A_{17-18}}{\ell_{17-18}}$$

$$Z_{18-19} = \frac{K_{18-19}\, A_{18-19}}{\ell_{18-19}}$$

$$Z_{18-19} = \frac{A_{10-19}}{\frac{1}{h_c} + \frac{\ell_{10-19}}{K_{10-19}}}$$

Further definitions

S_n = $M_n\, C_n$

M_n = mass of node n

C_n = specific heat of node n

A_{nm} = cross section of node interface between n & m (ft^2)

h_f = fluid heat transfer coefficient (BTU/hr $ft^{2o}F$)

h_c = contact heat transfer coefficient (BTU/hr $ft^{2o}F$)

ℓ_n = length of heat path in node n (ft)

ℓ_{nm} = length of heat path in nodes n & m (ft)

K_n = thermal conductivity in node n (BTU/hr $ft^{o}F$)

$R_n = \frac{t}{t_f - t_o}$ = temperature ratio at beginning of time stop

t = nodal temperature at time T

t_f = fluid temperature

t_o = nodal temperature at time 0

R_n' = temperature ratio at end of time step

ΔT = length of time step

61.4.3 Computer Solution for Specific Flange Assembly

The general equations previously presented have been solved for a specific case. This is for the test flange assembly shown in Figure 61.7 where one flange is aluminum, the other is stainless steel, the spacer is stainless steel and the bolt is aluminum. Thus nodes 1 through 8 are stainless and nodes 9 through 19 are aluminum. The following physical characteristics are assumed for these materials:

Aluminum

$K = 80$ Btu/hr. ft. ^{o}F

$C = 0.211$ Btu/lb. ^{o}F

$\rho = 0.101$ lb./in.^{3}

Stainless steel

$K = 10$ Btu/hr.ft. ^{o}F

$C = 0.117$ Btu/lb. ^{o}F

$\rho = 0.283$ lb./in.^{3}

When the above constants and the physical dimensions are substituted in the general equations of Tables III & IV, the equations of Table V are arrived at.

The equations of Table V were solved by a digital computer using time steps of 0.01 sec. The program was run for 50 sec. with a printout of results every second. Figure 61.13 shows some of the most significant of these results plotted in terms of dimensionless temperature vs. time.

The assumption is, of course, that the flange assembly is at temperature t_o when suddenly at time zero a fluid of temperature t_f is passed over the inner surface. Temperatures then start towards t_f and are given as a fraction of the total initial temperature difference $t_o - t_f$. The bolt temperature B is just an arithmetic average of all the temperatures of the bolt nodes but it should be quite close to the true average temperature. It is of interest to compare some of the curves of this figure with those of Figure 61.8 which was prepared for just plain disconnected flanges of the same dimensions and materials. It is apparent that they show fair agreement.

Table V

Equations for Test Flange Assembly of SK20-1286A

1. $1.17\ R1' = 0.000853\ R_f + 1.167937\ R_1 + 0.00121\ R_2$

2. $1.17\ R2' = 0.00121\ R_1 + 1.16758\ R_2 + 0.00121\ R_3$

3. $1.17\ R_3' = 0.00121\ R_2 + 1.167408\ R_3 + 0.00121\ R_4 + 0.000172\ R_6$

4. $1.17\ R_4' = 0.00121\ R_3 + 1.166947\ R_4 + 0.00121\ R_5 + 0.000172\ R_7 + 0.000461\ R_{14}$

5. $1.17\ R_5' = 0.00121\ R_4 + 1.168618\ R_5 + 0.000172\ R_8$

6. $0.219\ R_6' = 0.000172\ R_5 + 0.218048\ R_6 + 0.000227\ R_7 + 0.000553\ R_{11}$

7. $0.219\ R_7' = 0.000172\ R_4 + 0.000227\ R_6 + 0.217821\ R_7 + 0.000227\ R_8 + 0.000553\ R_{10}$

8. $0.219\ R_8' = 0.000172\ R_5 + 0.000227\ R_7 + 0.218048\ R_8 + 0.000553\ R_9$

9. $0.753\ R_9' = 0.000553\ R_8 + 0.742787\ R_9 + 0.00966\ R_{10}$

10. $0.753\ R_{10}' = 0.000553\ R_7 + 0.00966\ R_9 + 0.732666\ R_{10} + 0.00966\ R_{11} + 0.000461\ R_{19}$

11. $0.753\ R_{11}' = 0.000553\ R_6 + 0.00966\ R_{10} + 0.733127\ R_{11} + 0.00966\ R_{12}$

12. $0.753\ R_{12}' = 0.00966\ R_{11} + 0.73368\ R_{12} + 0.00966\ R_{13}$

13. $0.753\ R_{13}' = 0.00123\ R_f + 0.00966\ R_{12} + 0.74211\ R_{13}$

14. $0.117\ R_{14}' = 0.000461\ R_4 + 0.11620\ R_{14} + 0.000339\ R_{15}$

15. $0.103\ R_{15}' = 0.000339\ R_{14} + 0.102429\ R_{15} + 0.000232\ R_{16}$

16. $0.103\ R_{16}' = 0.000232\ R_{15} + 0.102536\ R_{16} + 0.000232\ R_{17}$

17. $0.103\ R_{17}' = 0.000232\ R_{16} + 0.102536\ R_{17} + 0.000232\ R_{18}$

18. $0.103\ R_{18}' = 0.000232\ R_{17} + 0.102429\ R_{18} + 0.000339\ R_{19}$

19. $0.141\ R_{19}' = 0.000461\ R_{10} + 0.000339\ R_{18} + 0.14020\ R_{19}$

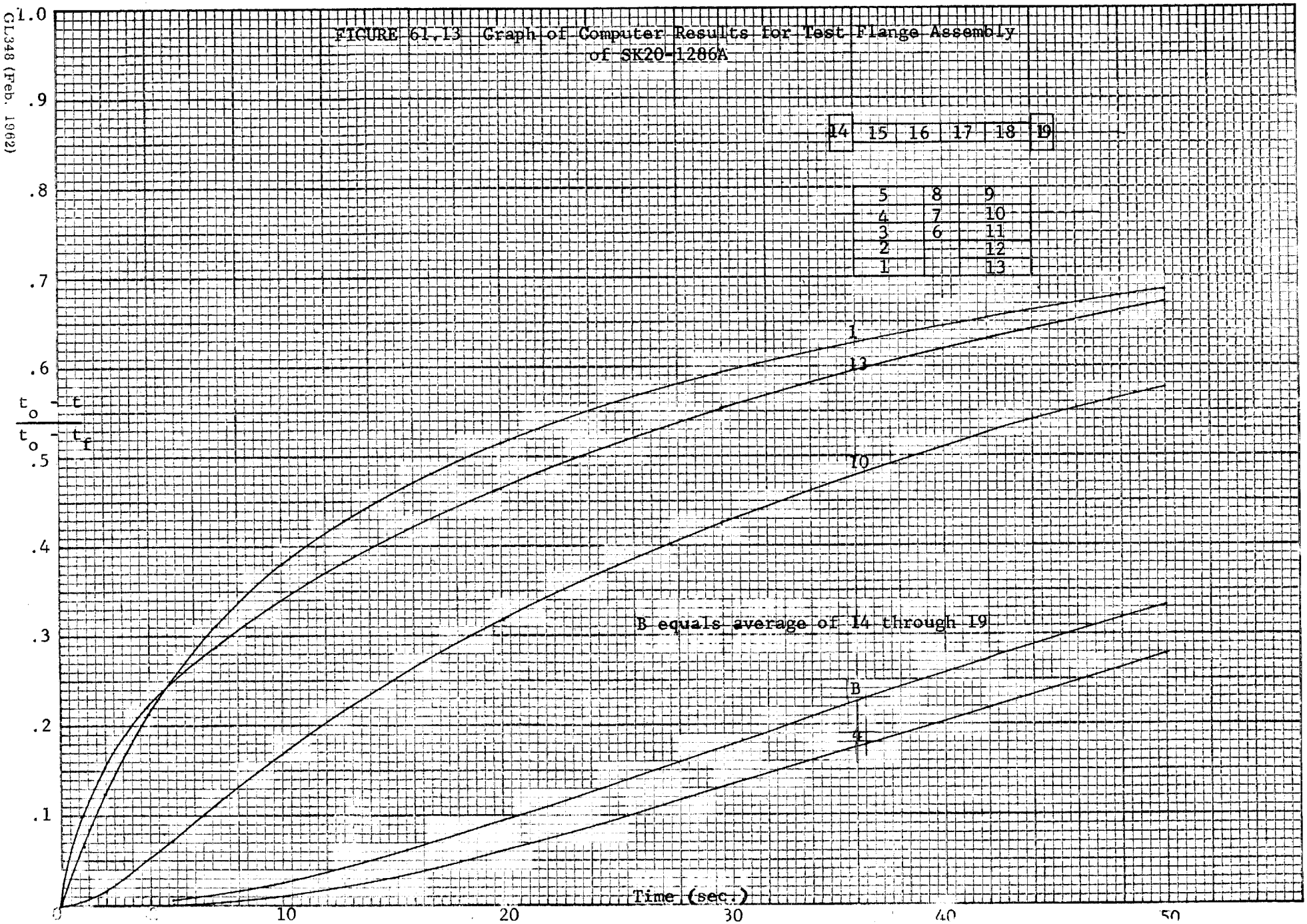

FIGURE 61.13 Graph of Computer Results for Test Flange Assembly of SK20-1286A

61.5 References

1. W. H. McAdams, Heat Transmission, 2nd Ed., McGraw-Hill, 1942.

2. J. G. Knudsen & D. L. Katz, Fluid Dynamics & Heat Transfer, 1958, McGraw-Hill.

3. E. R. G. Eckert & R. M. Drake, Heat & Mass Transfer, 2nd Ed., 1959, McGraw-Hill.

4. D. A. Labuntsov, "Generalized Correlation for Nucleate Boiling," Teploenergetika, Vol. 7, No. 5, 1960, pp. 76-81.

5. WADD Tech. Report 60-65, Part I, "Properties of Materials at Low Temperatures."

6. S. S. Kutaleladze, "Critical Heat Flux to Flowing, Wetting, Subcooled Liquids," Energetika, No. 2, 1959, p. 229.

7. M. P. Heisler, "Transient Thermal Stresses in Slabs and Circular Pressure Vessels," Pressure Vessels and Piping Desing Collected Papers 1927-1959, ASME, p. 532 (also J. Appl. Mech, 1953).

8. A. Mendelson and S. S. Manson, "Approximate Solution to Thermal Shock Problems in Plates, Hollow Spheres, and Cylinders with Heat Transfer at Two Surfaces," Trans. ASME, April 1956, pp. 545-553.

9. M. Jakob, Heat Transfer, Volume I, J. Wiley & Sons, 1958, p. 415, 416.

10. N. D. Weills and E. A. Ryder, "Thermal Resistance Measurements of Joints Formed Between Stationary Metal Surfaces", Trans. ASME, April 1949, p. 259-266.

11. M. E. Barzelay, N. Kim, and G. Holloway, "Effect of Pressure on Thermal Conductance of Contact Joints", NACA TN 3295, May 1955.

12. J. E. Hatch, R. L. Schacht, L. U. Albers, and P. G. Saper, "Graphical Presentation of Difference Solutions for Transient Radial Heat Conduction in Hollow Cylinders with Heat Transfer at the Inner Radius and Furite Slabs with Heat Transfer at One Boundary", Tech. Report No. 56, NASA

13. G. M. Dusinberre, Heat Transfer Calculations by Finite Differences, International Textbook Co., 1961.

62. EFFECT OF PRESSURE SURGES

by

B. T. Fang

62.0 Summary

The pressure surges ("water hammer") in a pipeline system have been studied extensively by hydraulic engineers (Refs. 1, 2 and 3). Attention was mainly given to the severe case of sudden stop of liquid flow in a pipeline. For launch vehicles we are faced with the pressure surges in connection with the sudden start of flow. In this section the magnitudes and frequencies of these pressure surges are studied. The essential effects they have on the sealing of fluid connectors are

(1) The higher pressure associated with these surges aggravates the already existing adverse effect of internal fluid pressure.

(2) These pressure surges are sources of shock loading which may excite undesirable vibrations.

(3) The results indicate that a proof pressure of twice the operating pressure would exceed any expected surge pressure.

53

62.1 Water Hammer Effect as a Phenomenon of Interchange of Kinetic and Pressure Energy

The water hammer effect is a phenomenon of the interchange of the kinetic and elastic (pressure) energy of the fluid. When the motion of the fluid is suddenly stopped, most of its kinetic energy is transformed into its elastic energy with a resulting increase in its pressure. Conversely, when the pressure of the fluid is suddenly released, most of its elastic energy is transformed into kinetic energy with a resulting increase in its velocity. It can be shown from an energy balance that the relation between the pressure change and velocity change is given by the simple formula (Ref. 1)

$$\frac{\text{Pressure Increment, } \Delta p}{\text{Velocity Reduction, } -\Delta v} = \sqrt{K\rho} \qquad (1)$$

where ρ is the density and K the bulk modulus of the fluid.

Equation (1) shows that the denser and the more incompressible the fluid, the greater is the magnitude of pressure surges.

62.2 Transmission and Reflection of Pressure Signals

Pressure signals are transmitted in a fluid with finite velocity - the velocity of sound. In a rigid pipe the velocity of sound of the fluid is (Ref. 1)

$$v_p = \sqrt{K/\rho} \tag{2}$$

For not-so-rigid pipes the velocity of sound is smaller. It can be calculated from Eq. (2) with the bulk modulus K replaced by the apparent bulk modulus (Ref. 1),

$$K' = K/(1 + \frac{2r}{tE} K) \tag{3}$$

where r is the radius, t the thickness and E the Young's modulus of the pipe.

Eq. (1) can now be written in the alternate form

$$\frac{\Delta p}{-\Delta v} = \rho v_p \tag{1a}$$

The following table gives v_p and $-\Delta p/\Delta v$ for some typical liquids in a rigid pipe

	Velocity of Sound v_p, fps	Pressure Increment, Δp, psi / Velocity Reduction, $-\Delta v$, fps
Water (60°F)	4700	63.3
Liquid Oxygen (-325°F)	3370	53.6
Liquid Hydrogen (-428°F)	4010	3.92

Within a pressure wave, the velocity of the fluid particle is given by Eq. (1a)

$$-\Delta v = \Delta p/\rho v_p$$

It is in the direction of wave propagation if the pressure wave is a compression wave and is opposite to the direction of wave propagation if it is a rarefaction wave.

The pressure wave will be reflected unchanged when it comes to the closed end of a pipeline. At the open end (where pressure is fixed) a pressure wave is reflected reversed in sign, i.e., a compression wave is reflected as a rarefaction wave and a rarefaction wave as a compression wave. At an obstruction (change in cross section of pipe, pipe bends, etc.), the pressure wave is partially transmitted and partially reflected. In particular, it can be shown from Eq. (1) and the equation of continuity that at a cross section where the area changes from A_1 to A_2 an incident wave of intensity Δp is reflected as a wave of intensity (Ref. 1)

$$\frac{A_1 - A_2}{A_1 + A_2} \quad \Delta p \tag{4}$$

and transmitted as a wave of intensity

$$\frac{2A_1}{A_1 + A_2} \quad \Delta p \tag{5}$$

With the above understanding we shall be able to discuss the sequence of events following the opening of a valve.

62.3 Instantaneous Valve Opening

If a valve can be opened instantaneously, the fluid layer adjacent to the valve drops to the outside pressure with a resulting increase in velocity Δv related to the pressure drop $-\Delta p$ by Eq. (1). This pressure drop, $-\Delta p$, propagates upstream with sonic velocity v_p. With the passage of this rarefaction wave, the fluid particles move downstream with velocity Δv. At the upstream end of the pipe (a tank or pump outlet), the pressure is maintained constant, the incoming rarefaction wave $-\Delta p$ is reflected as a compression wave of magnitude Δp moving downstream. The fluid particles now return to their previous pressure while acquiring a velocity $2\Delta v$. When this compression wave reaches the valve end, it is again reflected as a rarefaction wave moving upstream. This process goes on and on until finally a steady flow condition prevails. The following figure shows the idealized pressure and velocity variation at the mid-point of a pipeline.

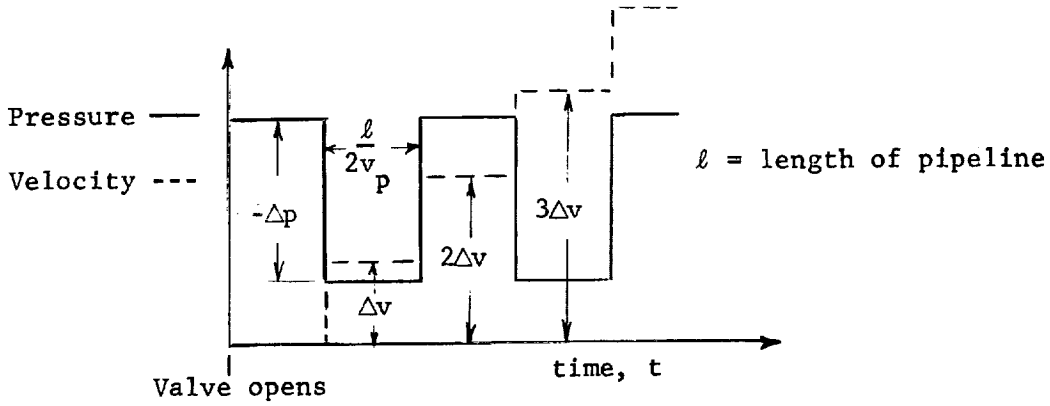

Fig. 62.1 Pressure and Velocity Variation in a Pipeline

The actual pressure-time and velocity diagram, of course, will have rounded corners and less stiff rises and falls because of friction and other effects. It is clear that in this case the pressure in the pipeline alternates between tank pressure and outside pressure, and there will be no dangerous high pressure build-up. This conclusion also holds if the opening of the valve is so rapid that the valve is fully open before the reflected compression wave comes back to the valve, i.e.,

$$\text{Time of valve opening} < \frac{\text{Twice the length of pipeline}}{\text{Velocity of pressure wave}}$$

62.4 Slower Valve Opening

The preceding section indicates that a characteristic time of the pipeline can be defined as

T = Time for pressure wave to travel from the valve to the pipe inlet and back

When the time of valve opening is less than T, we have the preceding case of instantaneous valve opening with no dangerous pressure build-up. When the time of valve opening is large compared with T, the elastic property of the fluid is negligible, and again there is no dangerous pressure build-up. In this section we shall discuss the case where the valve opening time is intermediate between these extremes and shall show that pressure surges can occur under certain cases.

In order to illustrate, we shall consider a valve partially opened instantaneously, with the opening held constant thereafter. The fluid layer behind the valve immediately experiences a pressure drop $-\Delta p$. The magnitude of Δp depends on percentage area of valve opening A. If the valve opening is not large, the usual discharge equation holds:

$$\Delta v = c_d A \sqrt{2p/\rho} \tag{6}$$

where c_d is the discharge coefficient (close to unity) and

$$p = p_o + \Delta p$$

p_o being the pressure in the pipeline before valve opening. This equation together with Eq. (1a)

$$-\Delta p = \Delta v \rho v_p \tag{1a}$$

enables us to determine the pressure drop $-\Delta p$. This pressure drop $-\Delta p$ (and velocity increment Δv) propagates as a wave of rarefaction upstream and is reflected at the pipe inlet as a compression wave. After the passage of this reflected compression wave, the fluid returns to the pressure p_o and acquires a velocity 2v. When the reflected compression wave comes back to the partially opened valve, because of the obstruction of the valve, only part of the wave is transmitted, the rest is reflected as a compression wave of intensity

$$\Delta p \left(\frac{1-A}{1+A} \right) \tag{7}$$

according to Eq. (4). The pressure in the pipeline now jumps to the pressure

$$p_o + \Delta p \left(\frac{1-A}{1+A} \right) \tag{8}$$

By keeping track of repeated reflections, we will be able to find out the pressure in the pipeline at each instant. The idealized pressure-time history at the valve end and at the mid-point along the pipeline is shown

in the following figures. The actual pressure-time history would, of course, be smoother because of friction effects and because of the impossibility of instantaneous valve opening.

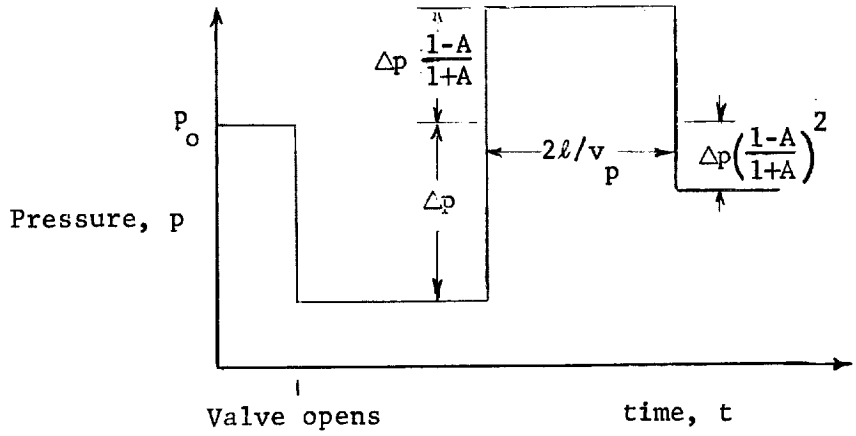

Fig.62.2a - Pressure-Time History at the Valve End

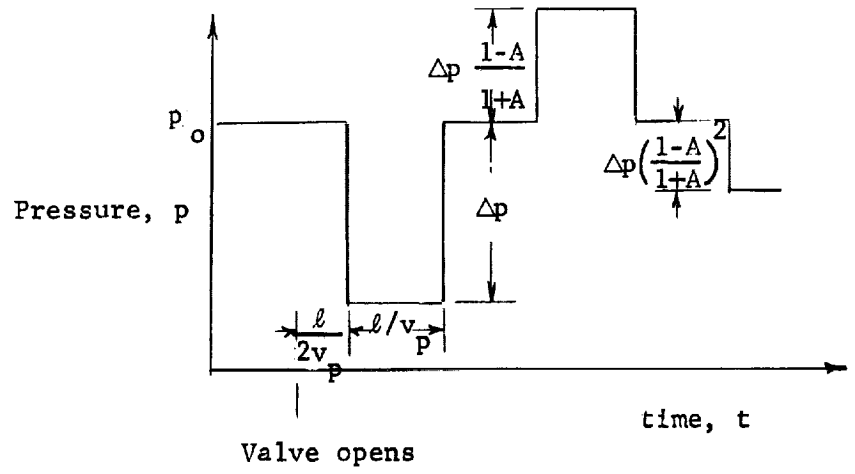

Fig.62.2b - Pressure-Time History at the Midpoint of the Pipeline

It is clear from these figures that each point along the pipeline experiences a decaying pressure oscillation of period $4\ell/v_p$. The maximum jump in pressure

$$-\Delta p\left(\frac{1-A}{1+A}\right) \tag{9}$$

is the same at points along the pipeline. But at points closer to the pipe inlet end, the duration of pressure quiescence is longer. Notice that since $\Delta p \leq p_o$ and $A \geq 0$, the pressure jump can never be greater than the static pressure of the fluid in the pipeline.

As an example, we shall consider a pipeline carrying liquid oxygen at 190 psig. A valve at 50 ft. from the pipe inlet is suddenly opened. The percentage area of opening is A = 1/4. For simplicity, we take the discharge coefficient $c_d = 1$. Eqs. (1a) and (6) become

$$-\Delta p = 53.6\Delta v \tag{1b}$$

$$\Delta v = 1/4\sqrt{\frac{2(190+\Delta p) \times 144}{2.3}} \tag{6a}$$

from which we obtain the pressure drop following the valve opening

$$-\Delta p = 189.1 \text{ psi}$$

The maximum pressure in the pipeline is

$$p_o - \Delta p\left(\frac{1-A}{1+A}\right)$$

$$= 190 + 189.1\left(\frac{1-1/4}{1+1/4}\right) = 303 \text{ psi}$$

The period of the pressure oscillation is

$$\frac{4\ell}{v_p} = \frac{4 \times 50}{33\%} = 0.06 \text{ sec.}$$

In the above we considered the valve as being opened instantaneously and held constant thereafter. In the actual situation the valve is being opened continuously, and we have to know the variation of valve opening with time. The above example shows that most of the pressure drop occurs in the beginning of the valve opening; therefore, a good approximation to the maximum pressure jump can be obtained as

$$p_o \frac{1-\bar{A}}{1+\bar{A}} \tag{10}$$

where $\bar{A}$ is the percentage area of valve opening at a time of $\frac{2\ell}{v_p}$ after the start of valve opening.

A surge pressure of 325 psi was recorded by Marshall Space Flight Center following the opening of valve for liquid oxygen at 190 psi. This shows good agreement with the present result, even though the exact manner of valve opening is not known. Also recorded was the 50 milliseconds time interval between the peak and the valley of the pressure surges. This corresponds to the half period $2\ell/v_p$ of the pipeline. Assuming a sonic velocity of

v_p = 3370 fps, this would correspond roughly to a pipe length of 85 ft.

It is to be noted that in the usual treatment of water hammer effect, the discharge equation (6) is used instead of Eq. (7) in the determination of the pressure surges. Water hammer is a transient effect. It seems to be unreasonable to use Eq. (6) which is based on the steady flow Bernoulli's Equation. Furthermore, the use of Eq. (6) cannot explain the sequence of events following the instantaneous valve opening. It is also in conflict with experimental data obtained in Huntsville and elsewhere. (The use of Eq. (6) can only predict pressure surges smaller than a quarter of the static pressure (Ref. 2).) The use of Eq. (7) in the present treatment seems to be more reasonable, based on physical reasoning as well as providing better correlation with experimental evidence.

61

62.5 Closing of Valve

The water hammer effect in the sudden closing of a valve is a subject treated extensively in the literature. We shall only describe it briefly here.

When a valve is closed instantaneously, the layer of fluid in contact with the upstream side of the valve is suddenly stopped; its kinetic energy is converted into strain energy with a sudden rise in pressure. This generates a compression wave moving upstream with sonic velocity, and with the passage of the compression wave, the fluid originally flowing with velocity v comes to a rest. Similarly, a rarefaction wave moves downstream of the valve. The amplitude of the compression wave can be obtained from Eq. (1a) as

$$\Delta p = -\Delta v \rho v_p$$

and it can be seen that dangerous high pressures may occur. The propagation and reflection of these pressure waves follow much the same manner we discussed previously. If the valve is not closed instantaneously, the pressure in the pipeline will be the superposition of these traveling waves and will in general be lower than that given by Eq. (1a). If, however, the valve closing time is shorter than the characteristic time T of the pipeline, then there is no chance for the reflected rarefaction wave to come back to the valve and prevent the pressure at the valve from reaching its maximum value given by Eq. (1a).

62.6 Fluid Reaction at Pipe Bends

We have shown that due to sudden initiation of flow, pressure surges approaching twice the operating pressure may occur. The increase in "hoop stress" in the pipe due to this pressure surge is usually considered in piping design. Because of the unavoidable existence of pipe bends, however, large bending moment and axial force may occur, depending on how the piping is supported. There are two kinds of fluid reaction at a pipe bend, that due to the fluid momentum and that due to fluid pressure. The fluid reaction due to the change of fluid momentum can be obtained as follows:

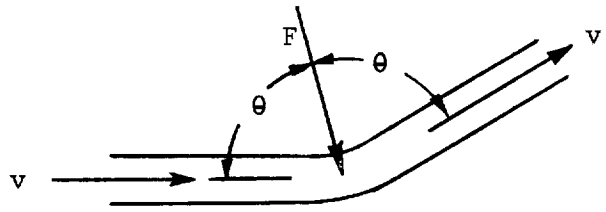

FIGURE 62.3 Reaction due to Change of Fluid Momentum at a Pipe Bend

From Newton's law we have

$$F = 2\,Q\,v\cos\theta$$

where Q = mass flow rate, slugs/sec.

v = fluid velocity, ft./sec.

F = reactive force, lb.

As an example consider a 90^{o} bend in a 20 in. inside diameter pipe. The fluid is LOX at a pressure of 190 psi, a density of 2.3 slug/ft^3 and at a velocity of 25 ft/sec.

then
$$F = 2\,(2.3)\,(\pi)\left(\frac{20}{2\text{x}12}\right)^2\,(25)\,\cos 45^{o}$$
$$= 180 \text{ lb.}$$

which is rather small in comparison with the end force of

$$(190)(\pi)\left(\frac{20}{2}\right)^2 = 59{,}600 \text{ lb.}$$

due to static fluid pressure. This example shows that the fluid momentum effect is generally not of importance unless there is possible resonance due to pulsating flow. The static pressure on the other hand is of great importance for fluids under high pressure. Depending on the method of

supporting the piping, the static pressure force may be transmitted as an axial load, a bending moment on the pipe or may be transmitted entirely to the support. The axial load due to static pressure has been well recognized by previous investigators. The possibility of large bending moment, however, has not attracted much attention. The following figure illustrates the situation where the static pressure at a pipe bend gives rise to bending moment but negligible axial load.

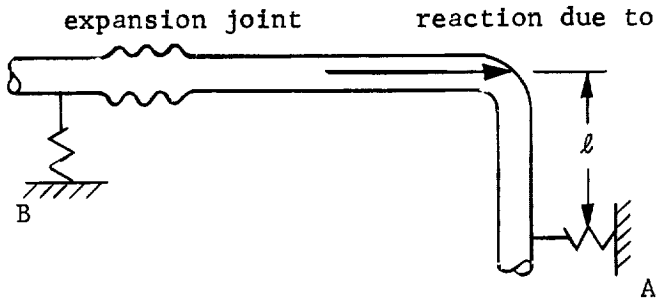

FIGURE 62.4 Pipe Arrangement Giving Rise to Large Bending Moment

Because of the flexibility of the expansion joint some of the hydraulic end load is transmitted to the support A. The pipe at A is subjected to a bending moment of $F\ell$. Take our previous example, and assume the unbalanced hydraulic end load is half the maximum possible with complete flexibility at the expansion joint,

$$F = 1/2\ (59,600)\ \text{lb.} = 29,800\ \text{lb.}$$

a length $\ell = 2$ ft., the bending moment at A is

$$29,800 \times 2(12) = 720,000\ \text{lb-lb}$$

which could be rather serious.

So far we have been considering the hydraulic end load under steady flow conditions. With the sudden intiation of flow, we have shown that surge pressures higher than the operating pressure may occur. First of all this higher pressure aggravates the adverse effects of hydraulic end load we have discussed above. Secondly it is a source of shock loading which may set up undesirable vibrations. The following figure illustrates a pipe arrangement which is subjected to negligible bending moment during steady operating conditions but to a shock loading during start-ups.

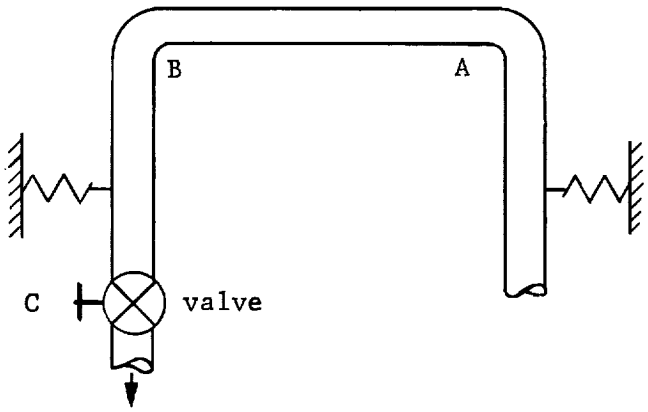

FIGURE 62.5 Pipe Arrangement Giving Rise to Impulse Following Valve Opening

Because of the pressure oscillation in the pipeline after sudden opening of the valve, the pressure at A and B may not be the same at any instant. This sets up an unbalanced force in the pipe. To illustrate, consider the valve at C being opened instantaneously. The pressure drops from the static pressure of approximately 190 psi to, say, vacuum. This pressure drop propagates upstream. After the wave front passes B, the hydraulic end force acting toward the left is reduced to zero, while at A the hydraulic end force acting toward the right is still 190 psi. There is an unbalanced force of (190) (pipe cross-sectional area) = 59,600 lb. acting to the right, which is taken by the pipe support. After a time interval of

$$t = \frac{\text{pipe length between A and B}}{\text{velocity of wave propagation}}$$

the wave front reaches A and the unbalanced force vanishes. Since the wave velocity is usually large, this time interval is small and this unbalanced force appears as a sharp impulse

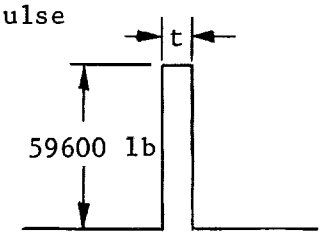

FIGURE 62.6 Impulse Due to Fluid Pressure

which may excite undesirable vibrations of the pipe system. This pressure wave is reflected back and forth and, therefore, will appear repeatedly until it finally dissipates. The situation becomes most serious when there is possible resonance.

62.7 Conclusions

In this section the pressure surges in a pipeline following the sudden opening of a valve have been investigated. It is concluded that

(1) There will be pressure oscillations in the pipeline with period equal to

$$\frac{4\ell}{v_p} = \frac{4 \text{ (pipe length from valve to pipe inlet)}}{\text{Velocity of wave propagation in the pipeline}}$$

If the valve opening is either very fast or very slow, there will be no high pressure build-up. For valve opening time intermediate between these extremes, there will be high pressure surges. The maximum amplitude will always be smaller than the static pressure p_o in the pipeline before opening and can be approximated by

$$p_o\left(\frac{1-\bar{A}}{1+\bar{A}}\right)$$

where $\bar{A}$ is the percentage area of valve opening at time $2\ell/v_p$ after the start of valve opening. At points closer to the pipe inlet, the duration of the high pressure is shorter.

(2) These high pressure surges may affect the sealing capability of the fluid connector in the following ways:

(a) They aggravate the adverse effects of internal pressure such as stretching the pipe line and reducing the gasket compression, causing the flanges to roll due to the barreling effect, and introducing higher stresses in the pipeline.

(b) They are a source of shock loading which may induce undesirable vibration of the pipeline.

(3) Recommendations:

(a) The usual proof pressure should be raised from 1.5 to 2 times the operating pressure, since, as shown in Eq. (10), the surge pressure may be greater than 1.5 times the operating pressure but never greater than twice the operating pressure.

(b) It is desirable to locate the fluid connector as far as possible from the valves, since the duration of pressure surges will be shorter there.

(c) Pipe layout should be treated with care to minimize the conditions that give rise to large bending moment due to hydraulic end load and the conditions that are prone to shock loading during start-up and shut-down.

62.8 References

1. H. Rouse (Editor), Engineering Hydraulics, Wiley, 1950.

2. C. Jaeger, Engineering Fluid Mechanics, Blackie, London, 1956.

3. L. Bergeron, Water Hammer in Hydraulics and Wave Surges in Electricity, Wiley, 1961.

67

63. EFFECT OF SHOCK AND VIBRATION ON CONNECTORS

by

G. W. Sarney

63.0 Summary

This section considers a simplified analysis of the missile piping system to determine its response in terms of pipe reactions of interest to the fluid connector designer. The sinusoidal and shock excitation levels specified for the Saturn C-1, Block II vehicle are used on typical pipe configurations to predict their response in terms of end bending moments. A dynamical method of analysis is presented for simple pipe configurations to show the nature of the problem. For complex pipe systems a simplified approach is used to give the fluid connector designer a quick estimate of the pipe reactions. The loads determined in typical examples are quite high and must be included in the connector design if leakage is to be avoided.

68

63.1 Introduction

The fluid connector joins sections of pipe and seals against leakage. Environmental conditions in the missile induce vibrations in the piping system which are transmitted through the fluid connector (Fig. 63.1). Design of the fluid connector requires an estimation and evaluation of the effect of these pipe reactions.

The random noise excitation may be predicted based on past tests and is presented in terms of vibration acceleration levels in the Shock and Vibration Specifications (Ref. 1). This loading acts on the pipe configuration which may be described by its end conditions, joints, physical dimensions, and damping characteristics. The response of the system can then be predicted with varying degrees of sophistication. This analysis uses a greatly simplified approach to meet the needs of the fluid connector designer to obtain estimates of the missile piping end reactions.

63.2 Environment

The piping system of a missile is subjected to vibrations due to such environmental effects as maneuvering loads, aerodynamic noise, the rocket engine sound field, and direct transmission from the supporting structure. These effects are grouped and presented in the "Shock and Vibration Specifications for Components on Saturn, C-1, Block II Vehicles" (Ref. 1). This specification presents acceleration loading for sinusoidal resonant vibrations in terms of peak "g" level for a given range of frequency. The shock test requirement specifies an impulse shape and "g" level of shock acting along any axis of the component.

71

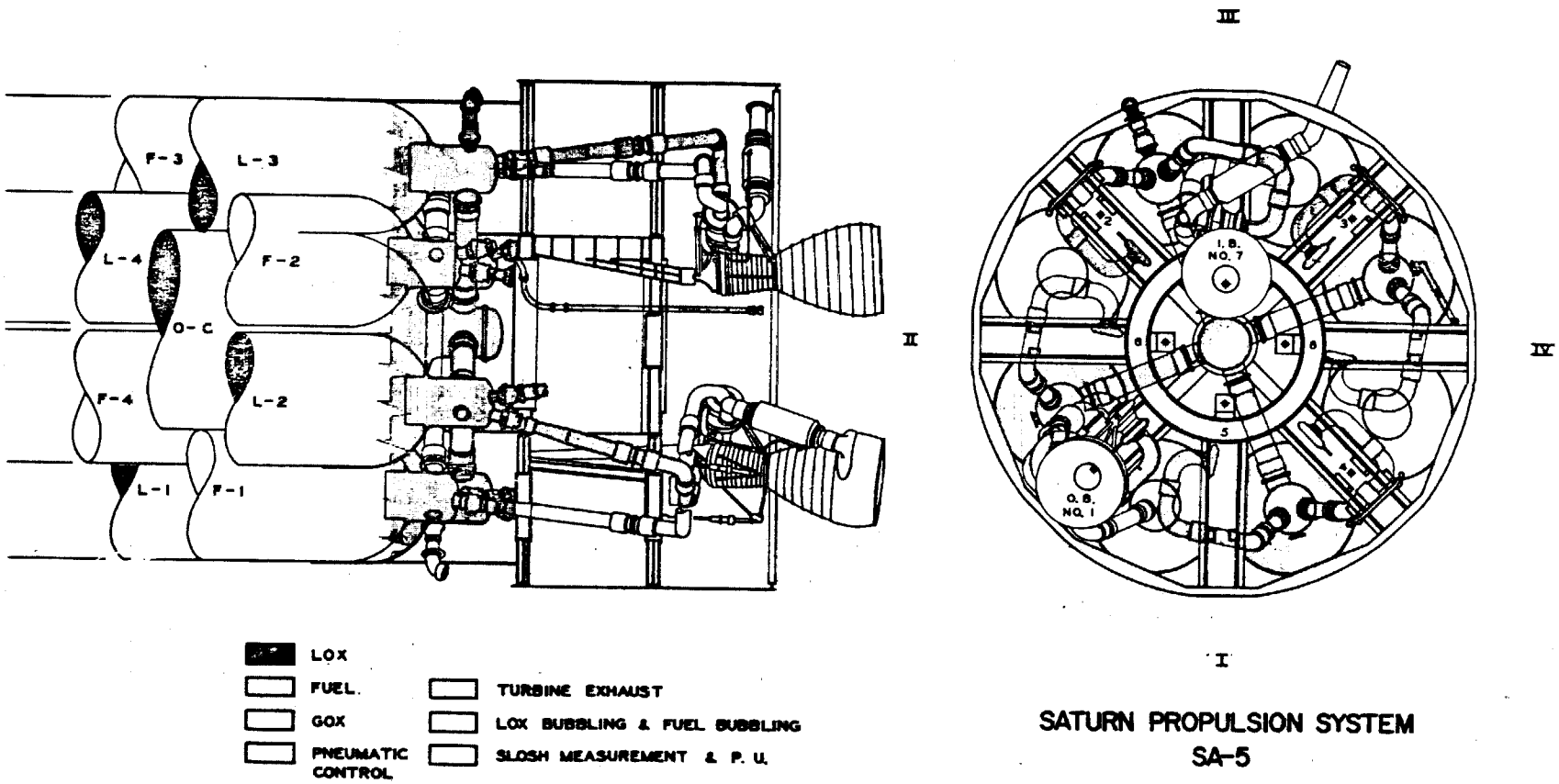

FIGURE 63.1

SATURN BLOCK II, LOX DUCTING

63.3 Definition of Component Loading

The vibration excitation in the missile environment is random in direction, magnitude and frequency. This random excitation acts on a piping system which usually has many intermediate joints connecting different shaped sections (see Fig. 63.1). A complete dynamical analysis of such a system is not required for the purposes of the fluid connector designer. The procedure here, then, is to make reasonable simplifications of the loading and structure to obtain quick estimates of the pipe end reactions.

The following simplifications of loading are made. The vibration acceleration level specified for the component under consideration will be the value for the frequency range which includes the natural frequency of the beam. This acceleration acts on the mass of the beam to produce a uniform load transverse to the beam and a concentrated load along the beam axis. The most severe vibrations will occur in a direction which is transverse to the longest beam length.

Complex pipe configurations will be resolved into straight beams whose length equals the pipe length normal (transverse) to the direction in which the acceleration acts. Sections of pipe along the acceleration axis will serve only to produce a concentrated load.

63.4 Response

The response of several typical pipe configurations will be obtained for the loading conditions discussed.

A simple configuration of a straight pipe with fixed ends (the actual end support may vary from simple-support to fixed; however, the effect of this variation on connector bending moment will depend on connector location) is first considered and the response found in terms of the normal modes of vibration of a simple beam based on the analysis of Sections 63.5 and 63.8. This analysis is useful to show the type of response typical of a missile piping system.

An example of a complex piping system is included to illustrate the simplifications of loading and pipe configuration used to estimate the response (Section 63.6). A static analysis is used on this type of system to compute the inertial reactions of the pipes for a given "g" level of excitation. The pipe reactions thus obtained are modified by an amplification factor for possible resonances.

The piping structure will contribute an appreciable amount of damping. The gimbal is a sliding type joint which serves as an additional damper so that the expected amplification factor at resonance, Q, has the range

$$5 < Q < 20$$

The conservative estimate Q = 20 will be used in the examples that follow.

63.5 Vibration Analysis of Lox Interconnector Line

This first example is a straight pipe to which a complete analysis can be simply applied.

The LOX interconnector line connects the main oxygen tank with smaller oxygen tanks on the periphery of the Saturn Block II Vehicle.

Configuration (See Fig. 63.2)

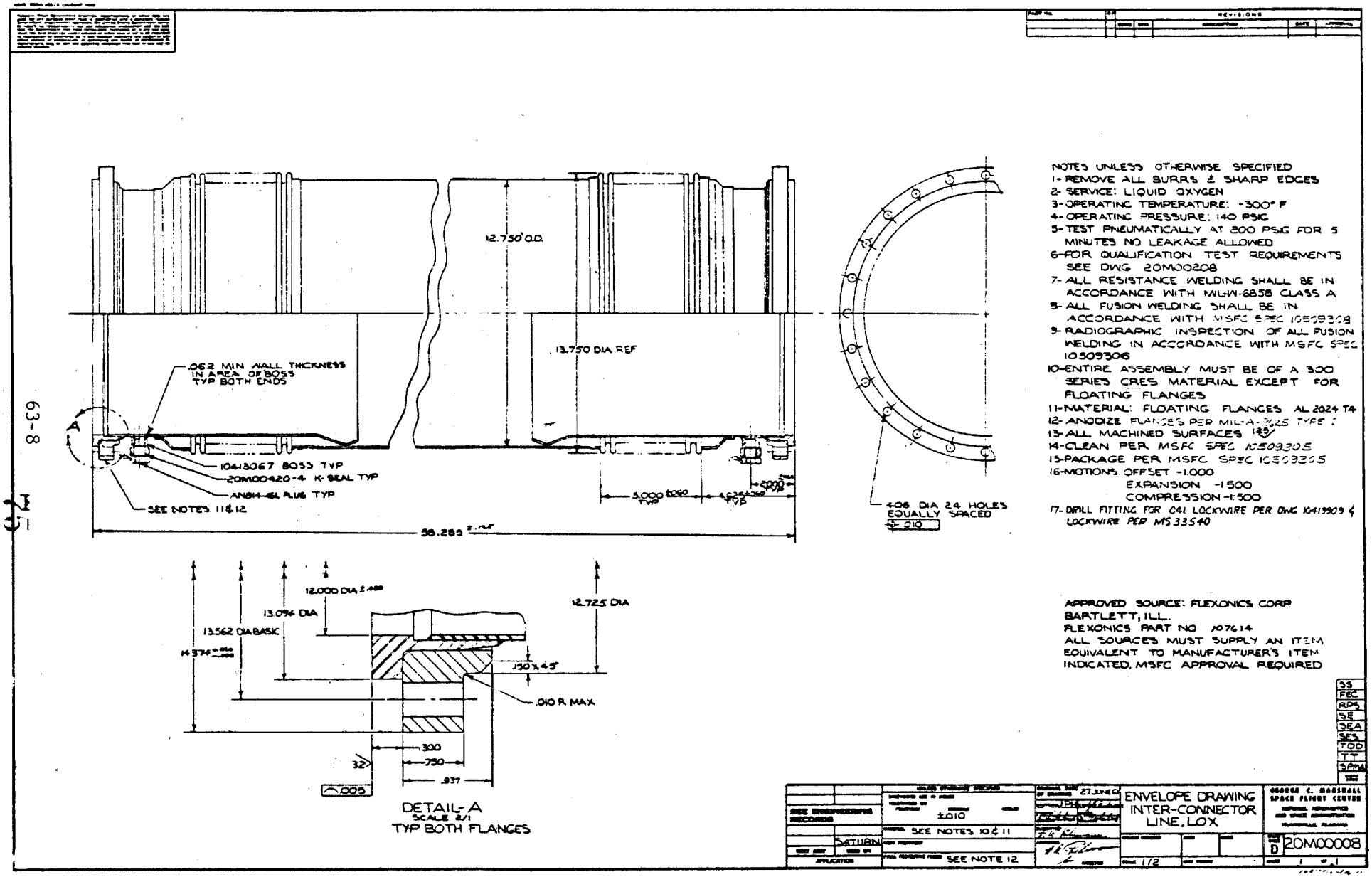

FIGURE 63.2 LOX INTERCONNECTOR LINE

63.5.1 Physical Parameters

Internal pressure	200 psig (max)
Density LOX	$\rho_L = 62.4$ lb/ft^3
Density Steel	$\rho_s = .285$ lb/in^3
Beam Thickness	$t = .0625$ in
Beam Diameter	$D_o = 12.75$ in
Beam Length	$\ell = 58.3$ in; $\ell^2 = 3390$ in^2; $\ell^4 = 11.5 \times 10^6$ in^4
Cross Section, Inertia	$I = 43.2$ in^4
Modulus of Elasticity	$E = 30{,}000{,}000$ lb/in^2
Beam Mass per Unit Length	$\rho = .0132$ lb sec^2/in^2
Beam Weight per Unit Length	$\mu = 5.09$ lb/in

63.5.2 Excitation

The LOX interconnector line is located in Zone 3-2-B as designated by the "Vibration and Shock Specifications for Components on Saturn, C-1 Block II Vehicles" (Ref. 1). In this zone the following vibration and shock requirements must be met along any axis of the LOX interconnector component.

Resonant Test Code 1-A

20-28 cps at 0.1 in D.A. displacement
28-72 cps at 4.0 g peak
72-140 cps at 0.015 in D.A. displacement
140-2000 cps at 15.0 g peak

Shock Test Code b

50 g peak

77

63.5.3 Analysis of Loading

All loading cases are considered with LOX in the pipes since this lowers the natural frequency and increases the magnitude of the load significantly.

The beam may be analyzed in either of the two models shown below, depending on stiffness of the gimbal joint.

Continuous Model

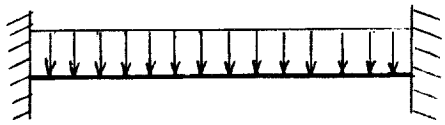

Discrete Model

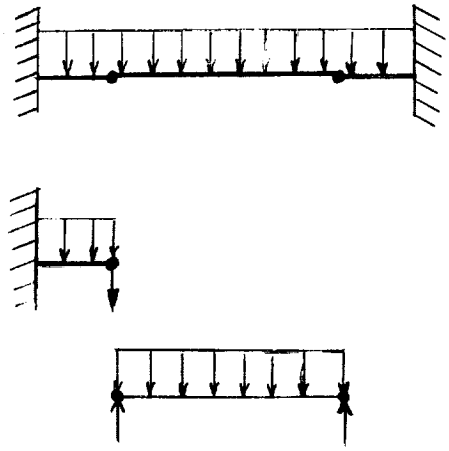

The gimbal joint configuration is as follows:

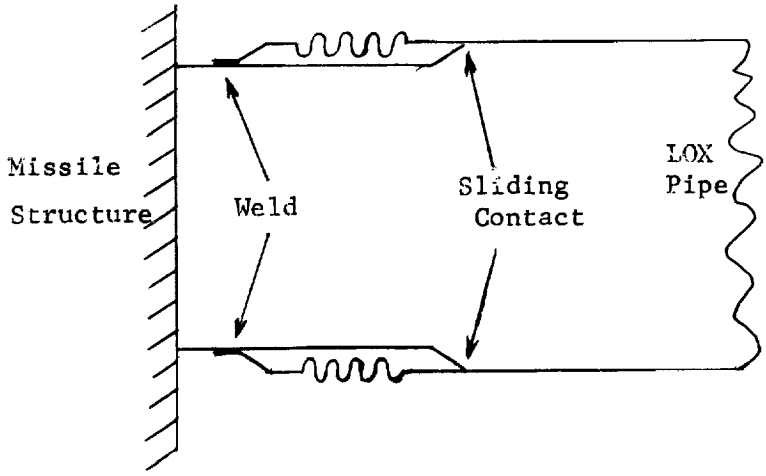

The relative stiffness in bending for this joint as compared to the LOX pipe is indeterminate. As extremes, the response of a continuous model with uniform stiffness will be compared with that of a model which assumes no gimbal stiffness in bending.

63.5.4 Response for Continuous Model

The following mode parameters are obtained from Ref. 2 for the continuous beam with clamped-clamped supports.

Mode	α_n	$B_n\ell$	$(B_n\ell)^2$	$(B_n\ell)^4$	f_n	$\phi_n(x=\ell/2)$	$\phi_n''(x=0)$
1	0.98	4.73	22.4	500.6	330cps	1.588	2.00
3	0.99	10.99	120.9	14617	1790cps	-1.406	2.00
5	0.99	17.28	298.6	89135	4400cps	1.414	2.00

63.5.4.1 Steady State Vibration

The steady state acceleration loading in the resonant test code requirement is most critical in the frequency range of 140 to 2000 cps where the peak acceleration is G = 15 g's.

This acceleration acts on the mass of the beam to produce the load intensity P(x). (See Appendix, Sec. 63.8)

$$P(x) = \mu G$$

Then

$$P_n = \frac{1}{\ell}\int_0^{\ell} (\mu G)\,\phi_n(x)\,dx$$

The integral is evaluated using Ref. 3, clamped-clamped beam, Integral #1.

$$P_n = \frac{(\mu G)\,2\alpha_n}{\ell\, B_n}\left[1-(-1)^n\right] \qquad n = 1,2,3\cdots\cdots$$

Since $\alpha_n \approx 1$ and for $n = 1,3,5,\cdots\cdots$

$$P_n = \frac{4\mu G}{\ell B_n}$$

We calculate the bending moment at the end of the beam (x=0) according to the relation obtained in the Appendix, Sec. 63.8

$$M = \sum_{n=1}^{\infty} \frac{\ell^2 P_n \phi_n''(x)}{(\ell B_n)^2} \frac{\sin(\omega t - \psi)}{\sqrt{\left(1-\frac{\omega^2}{\omega_n^2}\right)^2 + \frac{1}{Q^2}\left(\frac{\omega}{\omega_n}\right)^2}} \qquad n = 1,3,5\cdots\cdots \text{ (even modes are not excited)} \qquad (72)$$

The amplitudes of the fifth and higher modes are negligible and their natural frequencies are too high for resonances to occur in the range of interest. The amplification factor is taken to be Q=20.

The amplitude of the bending moment is:

$$M = (3390)(305.6)(2.0)\left[\frac{1}{(4.73)(22.4)\sqrt{\left(1-\frac{\omega^2}{\omega_1^2}\right)^2+\frac{1}{Q^2}\frac{\omega^2}{\omega_1^2}}}\right.$$

$$\left.+\frac{1}{(11)(121)\sqrt{\left(1-\frac{\omega^2}{\omega_3^2}\right)^2+\frac{1}{Q^2}\frac{\omega^2}{\omega_3^2}}}\right]$$

and

$$M = \frac{19600}{\sqrt{\left(1-\frac{f^2}{330^2}\right)^2+\frac{1}{400}\left(\frac{f}{330}\right)^2}} + \frac{1570}{\sqrt{\left(1-\left(\frac{f}{1740}\right)^2\right)^2+\frac{1}{400}\left(\frac{f}{1740}\right)^2}} \text{ in lb}$$

at f = 330 cps we get the maximum moment ignoring phase relations as:

$$M = 392{,}000 + 1600 = 393{,}600 \text{ in lb}$$

63.5.4.2 Shock Response for the Continuous Model

The transient excitation requirements in the shock test code are most critical for the rectangular type pulse. The ratio of response to excitation which is applied to each mode of beam vibration is: (See Appendix, Sec. 63.8.3

$$\frac{\text{Response}}{\text{Excitation}} = 1 - e^{-\eta_i t}\cos\omega_n t \qquad 0<t<\tau$$

for rectangular pulse τ =.005 seconds

A calculation is now made to determine the time needed to reach the maximum response amplitude for each mode in this beam. The maximum amplitude of the shock response occurs when

$$\cos\omega_n t = -1$$

Then the rise time is: $t = \pi/\omega_n$

Mode	Circular Frequency, ω_n	Rise-Time, t_n
1	(330)(6.28) rad/sec	.0015 second
3	(1790)(6.28)	.00028
5	(4400)(6.28)	.00011

Since there is little damping of the response during the excitation period (τ = 5 milliseconds) it is possible for the first fives modes to reach their maximum during this time and this summation must be considered.

The load function for a G = 50 g's peak impulse is

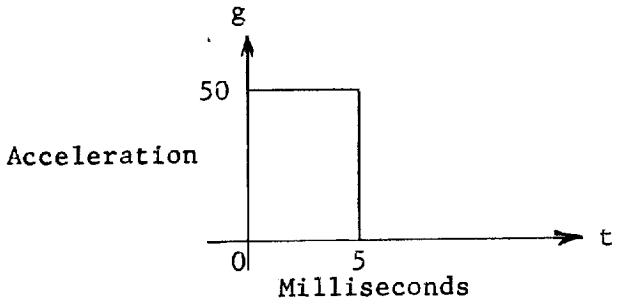

Now the load per unit length is:

$$P_n = \frac{1}{\ell}\int_0^{\ell} (\mu G)\,\phi_n(x)\,dx$$

Using the integral tables of Ref. 3 for the clamped-clamped beam:

$$P_n = \frac{(\mu G)\ (2\alpha_n)}{\ell\, B_n}\ \left[1 - (-1)^n\right] \qquad n = 1,2,3,4\cdots\cdots$$

Since $\alpha_n \approx 1$; $\mu G = (5.09)(50)$

$$P_n = \frac{1018}{\ell\, B_n} \qquad n = 1,3,5\cdots\cdots$$

The bending moment at the ends of the LOX pipe for a 50 g shock impulse as determined in Section 63.8 is:

$$M = \sum_{n=1}^{\infty} \frac{\ell^2 P_n \phi_n''(x)}{(\ell B_n)^2} \left[1 - e^{-\eta t} \cos\omega_n t\right]$$

The maximum amplitude of the end bending moment is therefore

$$M = \sum_{n=1}^{\infty} \frac{\ell^2 P_n \phi_n''(x)}{(\ell B_n)^2} \left[(2) \right] \qquad n = 1,3 \text{ (even modes are not excited)}$$

Then the value of bending moment neglecting phase is: (higher modes are negligible)

$$M = 131,000 + 10,400 = 141,400 \text{ in lb}$$

82

63.5.5 Response of Discrete Model

In this section the LOX interconnector is analyzed by considering the gimbal joint to have zero stiffness in bending.

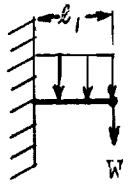

The beam loading is analyzed in two sections; however, the natural frequency of the system is a function of the deflections of the combined system. Since ℓ_1, is 12 inches, the split in the continuous beam (ℓ = 58 inches) occurs at its point of inflection or when the moment of the continuous beam is zero. This discrete model will have the same static deflection shape as the continuous model and hence nearly the same natural frequencies.

An approximate type of analysis will be used. The cantilver beam ℓ_1 will be analyzed as loaded with a uniform load and a concentrated load at the end due to one-half the loading on the center span ℓ_2. The mode parameters will be taken for the cantilever section alone as obtained from Ref. 2 for the uniform clamped-free beam. These are as follows:

Mode	f_n*	$\phi_n(\ell_1)$	$\phi_n''(0)$	$\beta_1 B_n$	$(\ell_1 B_n)^2$	α_n
1	330	2.00	2.00	1.875	3.516	.734
2	910	-2.00	2.00	4.694	22.03	1.018
3	1790	2.00	2.00	7.855	61.70	.999
4	2950	-2.00	2.00	10.995	120.90	1.000
5	4400	2.00	2.00	14.137	199.86	.999

* f_n for continuous beam model

63.5.5.1 Resonant Vibration

Steady-state vibration response for a sinusoidal excitation of G = 15 g's is now calculated:

Load: $W = 1/2(5.09)(58-24)(G) = 86.6\ G$

then $W = 1300$ lb.

Then the load intensity is:

$$P(x) = W(x=\ell_1) + \mu G$$

and

$$P_n = \frac{W}{\ell_1}\phi_n(\ell_1) + \frac{1}{\ell_1}\int_0^{\ell_1} \mu G \phi_n(x)\,dx$$

Using the tables of integrals in Ref. 3 for a cantilever beam

$$P_n = \frac{W}{\ell_1}\phi_n(\ell_1) + 2\left(\frac{\mu G \alpha_n}{\ell_1 B_n}\right) \qquad n = 1,2,3,4,5,\cdots\cdots$$

The steady state response for moments at the fixed end of the cantilever beam based on the relation from Section 63.8 is

$$M = \sum_{n=1}^{\infty} \frac{\ell_1^2 P_n \phi_n''(x=0)}{(\ell_1 B_n)^2} \frac{\sin(\omega_n t - \psi)}{\sqrt{\left(1 - \frac{\omega^2}{\omega_n^2}\right)^2 + \frac{1}{Q^2}\left(\frac{\omega^2}{\omega_n^2}\right)}}$$

Neglecting phase, as a conservative assumption, the amplitude of this bending moment for the first four modes then is

$$M_{x=0} = \left|\frac{(2)(144)\left[\frac{1300}{12}(2.0) + \frac{(2)(76.3)(.734)}{1.875}\right]}{(3.516)\sqrt{\left(1 - \frac{f^2}{(330)^2}\right)^2 + \frac{1}{Q^2}\left(\frac{f^2}{(330)^2}\right)}}\right| + \left|\frac{(2)(144)\left[\frac{1300}{12}(-2.0) + \frac{(2)(76.3)(1.018)}{4.69}\right]}{(22.03)\sqrt{\left(1 - \frac{f^2}{910^2}\right)^2 + \frac{1}{Q^2}\left(\frac{f^2}{910^2}\right)}}\right|$$

$$+ \left|\frac{(2)(144)\left[\frac{1300}{12}(2.0) + \frac{(2)(76.3)(.999)}{7.855}\right]}{(61.7)\sqrt{\left(1 - \frac{f^2}{1790^2}\right)^2 + \frac{1}{Q^2}\left(\frac{f^2}{1790^2}\right)}}\right| + \left|\frac{(2)(144)\left[\frac{1300}{12}(-2.0) + \frac{(2)(76.3)(1.00)}{10.99}\right]}{(120.9)\sqrt{\left(1 - \frac{f^2}{2940^2}\right)^2 + \frac{1}{Q^2}\left(\frac{f^2}{1790^2}\right)}}\right|$$

The amplification factor at resonance is taken to be Q=20 as for the continuous beam:

$$M_{x=0} = \frac{22{,}700}{\sqrt{\left(1 - \frac{f^2}{330^2}\right)^2 + \frac{1}{400}\left(\frac{f^2}{330^2}\right)}} + \frac{2{,}410}{\sqrt{\left(1 - \frac{f^2}{910^2}\right)^2 + \frac{1}{400}\left(\frac{f^2}{910^2}\right)}} + \frac{1{,}110}{\sqrt{\left(1 - \frac{f^2}{1740^2}\right)^2 + \frac{1}{400}\left(\frac{f^2}{1740^2}\right)}}$$

The amplitude of the end bending moment at the worst condition when, f = 330 cps, is:

$$M = 454,000 + 2,000 + 1,000 = 457,000 \text{ in lb.}$$

63.5.5.2 Transient Solution for Cantilever Beam

The analysis of the response function for a rectangular shock pulse is similar to the approach used for the continuous model. Therefore, the maximum ratio of response to excitation is two for each mode. The excitation function for a G = 50 g's rectangular impulse on the cantilever beam is similar in form to the steady state vibration excitation.

$$P_n = \left[\frac{86.6}{\ell_1}\phi_n(\ell_1) + 2\frac{\mu\alpha_n}{\ell_1 B_n}\right] G$$

The maximum amplitude of the clamped end bending moment therefore is:

$$M_{x=0} = \sum_{n=1}^{\infty} (2)\frac{\ell_1^2 P_n \phi_n''(x=0)}{(\ell_1 B_n)^2}$$

Considering the first three modes, and neglecting phase:

$$M_{x=0} = 151,000 + 16,000 + 7,300 = 174,000 \text{ in lb.}$$

63.6 Vibration Analysis of LOX Suction Line

The LOX suction line is an example of a complex pipe configuration which must be simplified.

The LOX suction line connects the LOX tanks to the nozzle assembly. A typical configuration from the Saturn Block II Vehicle (Fig. 63.1) is shown in the attached drawing (Fig. 63.3).

86

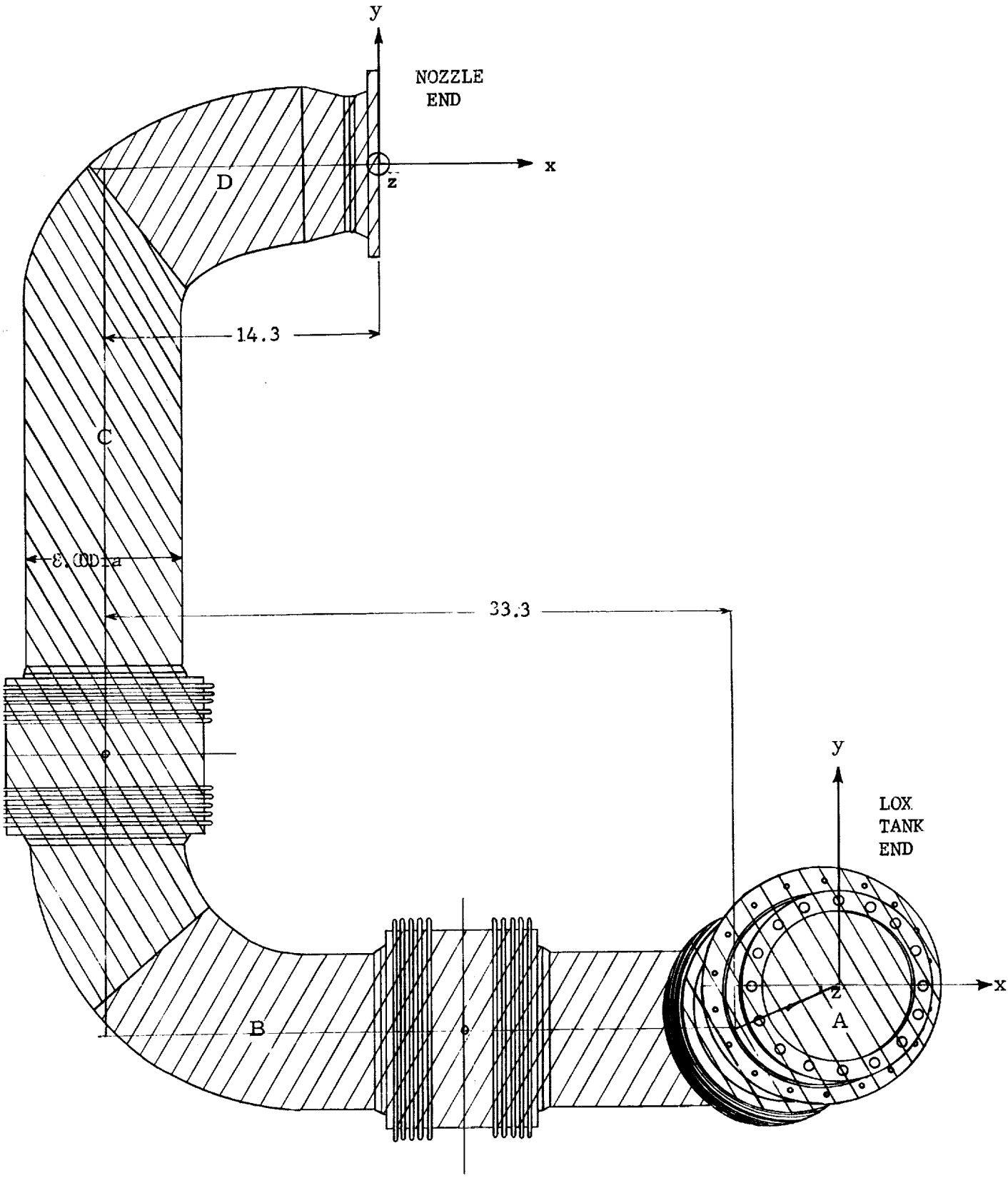

LOX SUCTION LINE - TOP VIEW

FIGURE 63.3 (a)

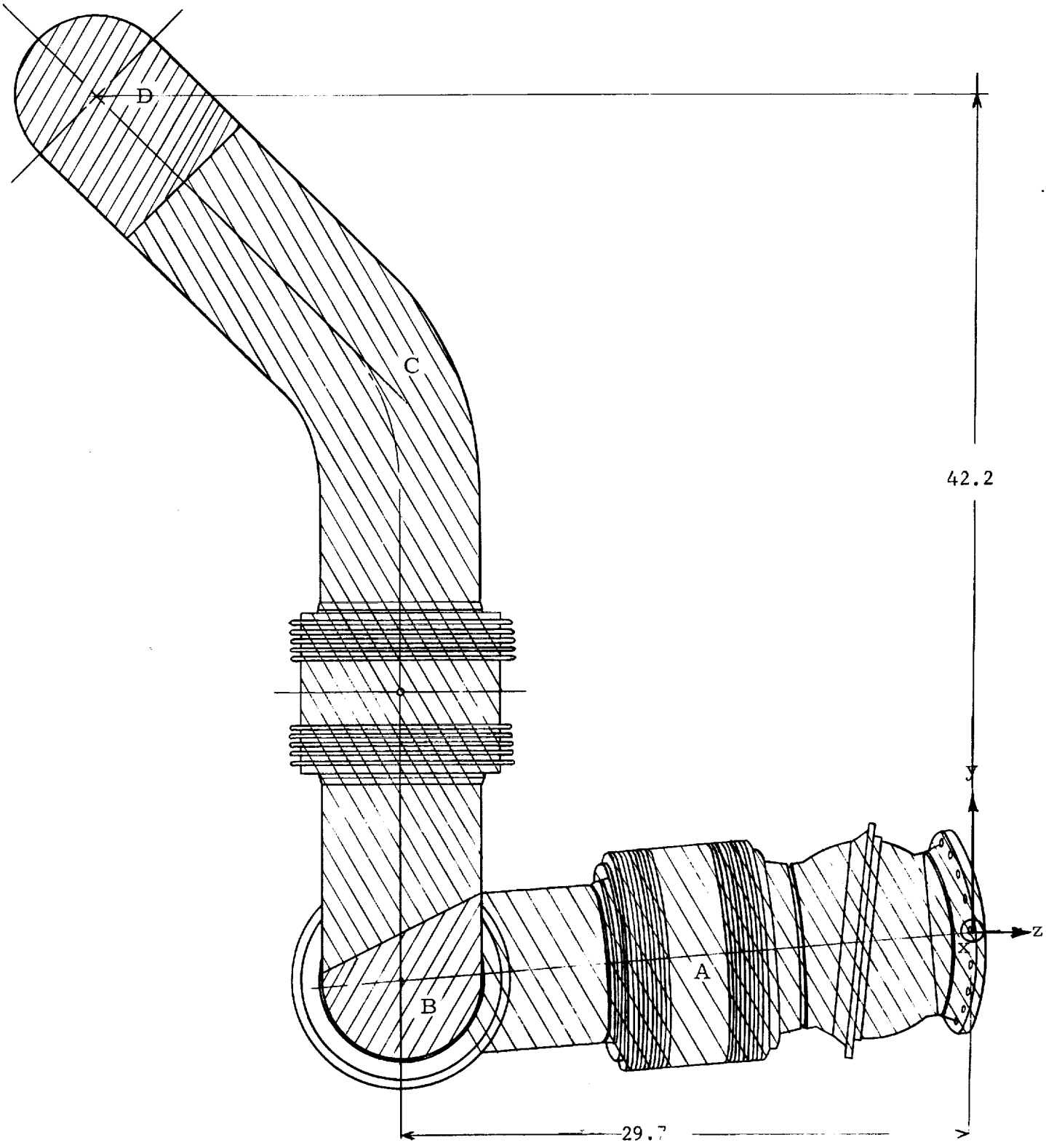

LOX SUCTION LINE - SIDE VIEW

FIGURE 63.3 (b)

63-21

63.6.1 Physical Parameters

The following parameters are typical and are applied as though continuous in the system:

Density LOX	ρ_L	= 62.4 lb/ft^3
Density steel	ρ_s	= .285 lb/in^3
Line thickness	t	= .0625 in
Line diameter	D_o	= 8.00
Cross section inertia	I	= 11.8 in^4
Modulus of Elasticity	E	= 30x10^6 psi
Line mass per unit length	ρ	= .00573 lb sec^2/in^2
Line weight per unit length	μ	= 2.21 lb/in

63.6.2 Loading Requirement

The LOX suction line is located in Zone 1-1-G as designated by the "Vibration and Shock Specifications for Components on Saturn, C-I, Block II Vehicles". In this zone the following steady-state vibration and transient shock conditions must be met when the inputs are applied to the end of the line which fastens to the pump on the lower end.

Resonant Test Code 1-A

20-100 cps at 4.0 g peak
100-142 cps at 0.0078 in D.A. displacement
142-540 cps at 0.00055 in D.A. displacement
540-1000 cps at 0.00055 in D.A. displacement
1000-2000 cps at 28.0 g peak

Shock Test Code b

100 g peak

63.6.3 Analysis of Loading

The procedure here is to consider the system to have uniform stiffness and to consider the acceleration to act along each of the three axes shown on the drawing. The pipe system is split into four sections labeled A, B, C and D which are either normal to or lie along the axes x, y and z. Each section has a static weight per unit length given by $\mu = 2.21$ lb/in. The complex pipe configuration will be simplified by constructing a beam of length equal to the pipe length which is normal to the direction of the acceleration. The loading diagram for acceleration acting along the y axis is:

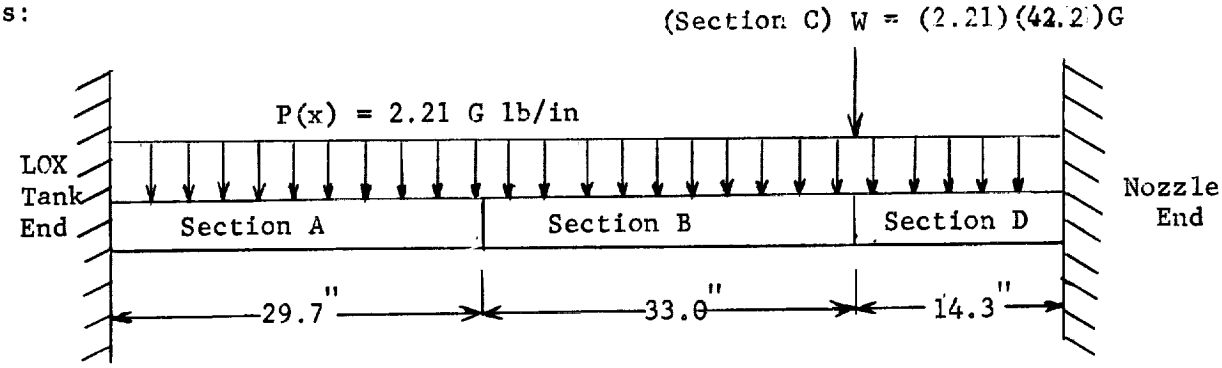

The pipes which are normal in direction to the axis through which the acceleration acts contribute a uniform load along their length, and pipes which are parallel to the acceleration axis contribute a concentrated load. The bending moments at the fixed ends can be calculated for a steady load distribution at the "g" level of excitation along each of the three axes. These values are modified by an amplification factor for possible resonances (Q=20).

This procedure is used to find the bending moments at each end of the LOX suction line for the three cases in which the acceleration is resolved along the x, y and z axes respectively. The accuracy depends on the ability to obtain the same deflection shape in the equivalent model with the new length and loading conditions.

63.6.4 Response

The first case is analyzed using the loading diagram above for acceleration resolved along the y axis. The moments at the ends are evaluated by superimposing the following two loading diagrams and applying formulas from Roark, Ref. 5.

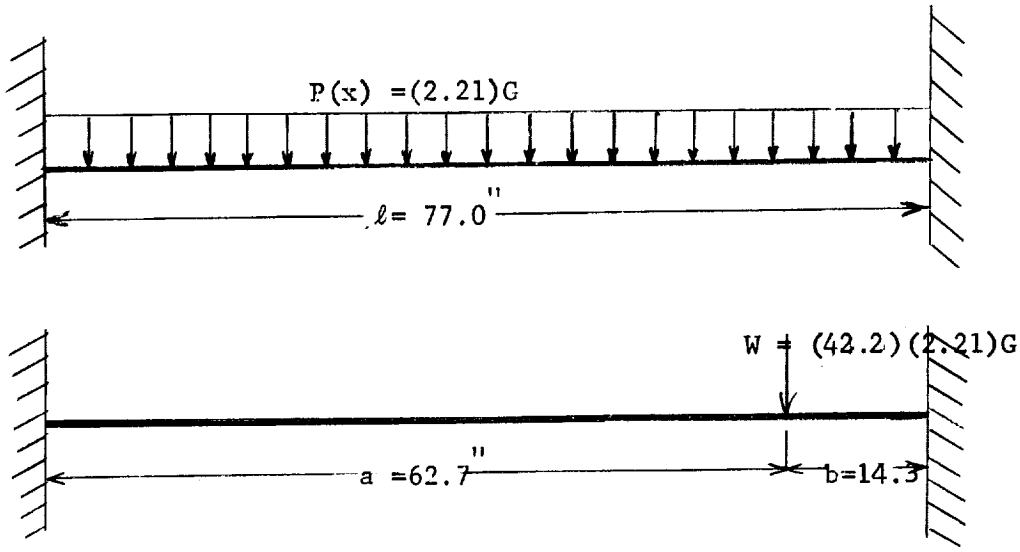

Then $M_1 = \left[\frac{(2.21)(77)^2}{12} + \frac{(62.7)(14.3)^2}{(77)^2}(42.2)(2.21)\right] G = 1300\ G$

$M_2 = \left[\frac{2.21(77)^2}{12} + \frac{(62.7)^2(14.3)}{(77)^2}(42.2)(2.21)\right] G = 2020\ G$

For this component G = 4 g's, assuming the natural frequency below 100 cps.

M_1 = 5,200 in lb

M_2 = 8,000 in lb

Applying the expected amplification factor for resonance

M_1 = 104,000 in lb

M_2 = 161,000 in lb

92

The second case is analyzed using the following loading diagram for weight resolved along the x axis.

(Section B) W = (33)(2.21)G

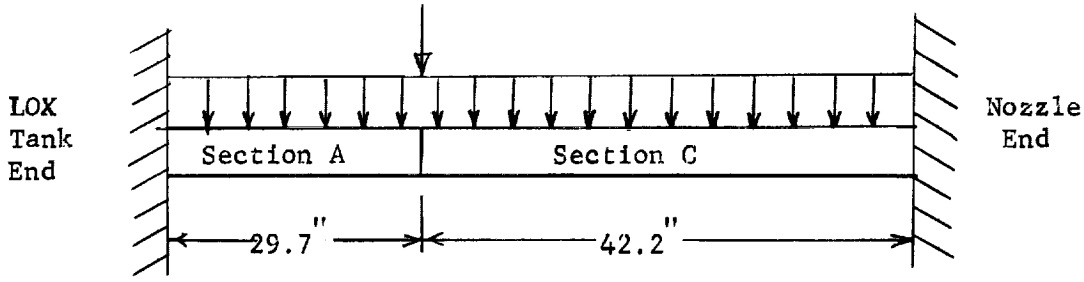

The moments at each end are obtained by superimposing the following loading diagrams:

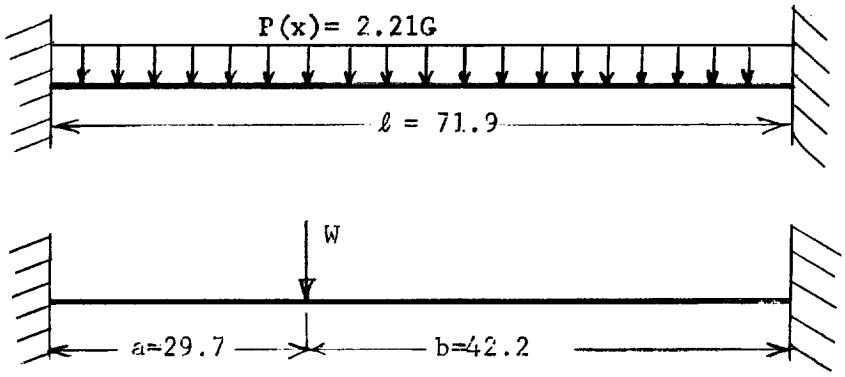

$$M_1 = \left[\frac{(2.21)(71.9)^2}{12} + \frac{(2.21)(33)(29.7)(42.2)^2}{(71.9)^2}\right] \quad G = 1700\ G$$

$$M_2 = \left[\frac{(2.21)(71.9)^2}{12} + \frac{(2.21)(33)(42.2)(29.7)^2}{(71.9)^2}\right] \quad G = 1490\ G$$

For the LOX suction line G = 4 g's

M_1 = 6,800 in lb

M_2 = 6,000 in lb

The end pipe reactions at resonance are then: (Q = 20)

M_1 = 136,000 in lb

M_2 = 120,000 in lb

The third case is analyzed using the following loading diagram for weight resolved along the z axis.

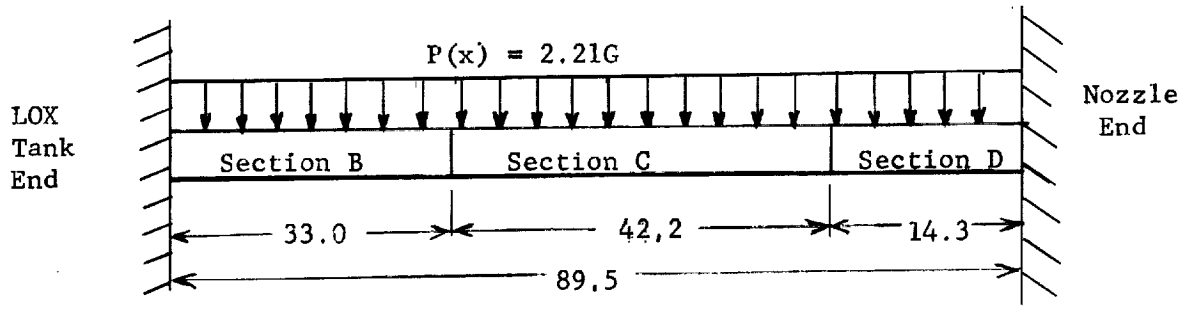

The static bending moments at each end are:

$$M_1 = \frac{(2.21)(89.5)^2}{12} G = 1550\ G$$

M_2 = 1550 G

For the LOX suction line G = 4 g's

M_1 = 6,200 in lb

M_2 = 6,200 in lb

Applying the amplification factor for resonance, Q=20:

M_1 = 124,000 in lb

M_2 = 124,000 in lb

63.7 Conclusions

Only for simple pipe configurations can an exact dynamical analysis be easily applied. For pipe systems with intermediate joints or curved sections, the normal modes of vibration cannot be predicted easily, and simplifications must be made. A pipe system of variable stiffness, complex shape and uniform loading is replaced by an equivalent straight beam with a uniform stiffness, an altered length and a variable loading to approximate the deflection curve of the original configuration. The typical examples of this section show that gimbal-type joints of indeterminate stiffness occur near the point of inflection of the continuous equivalent system so that a good approximation for the deflection curve of the original configuration is obtained. A static analysis of the equivalent system can be used to obtain a reasonable estimate of the pipe end reactions for purposes of the fluid-connector designer.

The end reactions determined on some typical pipe configurations in the environment of the Saturn C-1 Vehicle are quite high and must be considered in the connector design if leakage is to be avoided.

95

3.8. Appendix: Vibration Analysis of Beam

3.8.1 Normal-Mode Analysis (Summary of References 3 and 7)

The governing differential equation of motion of a beam with a time-varying load is obtained by equating the external load intensity to the sum of the inertial and elastic loads.

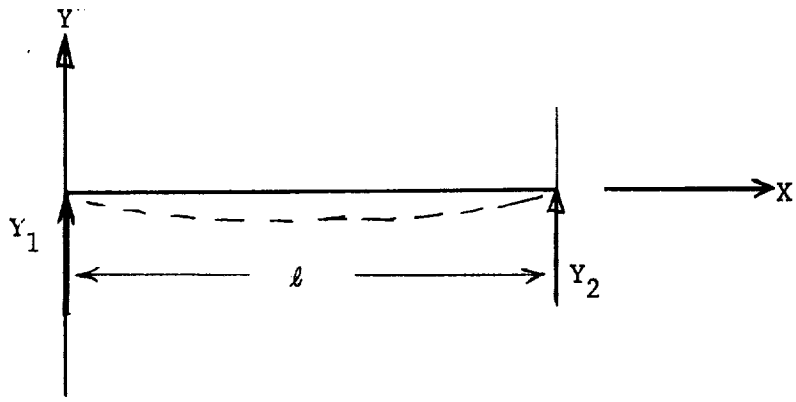

The equation of motion is written with respect to the co-ordinate system, X,Y. Motion of the beam with respect to this co-ordinate system denoted by "y" may be caused by an application of an external load or by movement of the beam supports which is denoted by Y_1 and Y_2. The movement of the supports with respect to the fixed co-ordinate system produces an equivalent "G" loading on the beam. This "G" loading is a continuous load which has a value at x=0 of

$$P(0) = \rho \frac{\partial^2 Y_1}{\partial t^2} \tag{1}$$

and at $x = \ell$

$$P(\ell) = \rho \frac{\partial^2 Y_2}{\partial t^2} \tag{2}$$

This equivalent load intensity varies linearly across the beam to satisfy the boundary values.

For the case of uniform acceleration $\frac{\partial^2 Y_1}{\partial t^2} = \frac{\partial^2 Y_2}{\partial t^2} = Gg$ (3)

the equivalent load intensity becomes

$$P(x,t) = \rho G g f(t) \tag{4}$$

or

$$P(x,t) = \mu G f(t) \tag{5}$$

where ρ = mass per unit length of beam
μ = weight per unit length
G = number of g's - uniform acceleration
f(t) = time function of acceleration loading

The external load produces a beam deflection y with respect to the ends of the beam. This deflection is resisted by the following forces.

1. Flexural stiffness of beam - resistance to bending along beam.

$$M = - EI \frac{\partial^2 y}{\partial x^2}, \quad \text{bending moment} \tag{6}$$

$$Q = \frac{\partial M}{\partial x}, \quad \text{shear force} \tag{7}$$

$$P(x,t) = -\frac{\partial Q}{\partial x} = EI \frac{\partial^4 y}{\partial x^4}, \quad \text{load intensity} \tag{8}$$

where: EI is uniform stiffness of beam

2. Beam Inertia - resistance to movement of each section

$$P(x,t) = \rho \frac{\partial^2 y}{\partial t^2} \tag{9}$$

where: ρ = uniform density of beam

3. Damping in beam - considered viscous and distributed along the beam

$$P(x,t) = C \frac{\partial y}{\partial t} \tag{10}$$

The governing equation for flexural vibration of the beam, neglecting shear forces and rotary inertia, is:

$$EI \frac{\partial^4 y}{\partial x^4} + \rho \frac{\partial^2 y}{\partial t^2} + C \frac{\partial y}{\partial t} = \mu G f(t) \tag{11}$$

where: y = deflection of beam with respect to its ends (in)
EI = bending stiffness of beam - uniform $(lb/in^2)(in^4)$
ρ = uniform mass density per unit length $(lb/sec/in^2)$
C = damping coefficient per unit length
μ = beam weight per unit length
G = number of "g's" peak acceleration
f(t) = time function of acceleration loading (12)

The beam is a continuous system with an infinite number of degrees of freedom which may be analyzed by superimposing the response in the normal modes.

Let beam deflection in each mode $y_n = \phi_n(x)\ \gamma_n(t)$ (13)

Then beam deflection $$y = \sum_{n=1}^{\infty} \phi_n(x)\ \gamma_n(t) \tag{14}$$

where the mode shape in the nth mode is $\phi_n(x)$ and the amplitude γ_n.

The normal modes are solutions of:

$$EI \frac{\partial^4 y}{\partial x^4} + \rho \frac{\partial^2 y}{\partial t^2} = 0 \tag{15}$$

Trying as an assumed solution

$$y_n = \phi_n(x) \sin\omega_n t \tag{16}$$

then Eq. (15) yields:

$$\frac{\partial^4}{\partial x^4} \left[\phi_n(x)\right] - \frac{\rho\, \omega_n^2}{EI} \phi_n(x) = 0 \tag{17}$$

Define

$$\beta_n^4 = \frac{\rho\, \omega_n^2}{EI} \tag{18}$$

then

$$\frac{\partial^4}{\partial x^4} \left[\phi_n(x)\right] - \beta_n^4 \phi_n = 0 \tag{19}$$

Define

$$\phi_n''''(x) = \frac{1}{\beta_n^4} \frac{\partial^4}{\partial x^4} \left[\phi_n(x)\right] \tag{20}$$

then

$$\phi_n''''(x) - \phi_n = 0 \tag{21}$$

The general solution for the mode shape $\phi_n(x)$ from equation (19) is:

$$\phi_n(x) = A\sin\beta_n x + B\cos\beta_n x + C\sinh\beta_n x + D\cosh\beta_n x \tag{22}$$

The constants A, B, C, and D are solved from the boundary conditions of mode shape at the ends of the beam and may be grouped as follows:

$$\phi_n(x) = \cosh\beta_n x - \cos\beta_n x - \alpha_n(\sinh\beta_n x - \sin\beta_n x) \tag{23}$$

The mode shape for the case of a simply supported beam will be analyzed here to determine β_n, α_n and $\phi_n(x)$. These values are tabulated for all other mounting conditions for the first five modes in Ref. 2.

Boundary conditions - simply supported beam

$$y = 0;\ x = 0,\ x = \ell \tag{24}$$

$$y'' = 0;\ x = 0,\ x = \ell \tag{25}$$

Applying the above conditions to Eq. (23) yields:

$$\phi_n(x) = \sin\beta_n x \tag{26}$$

Using $y = 0;\ x = \ell$ (27)

$$0 = \sin\beta_n \ell \tag{28}$$

then

$$\beta_n \ell = n\pi \qquad n = 1,2,3,\cdots\cdots \tag{29}$$

From Equation (18)

$$\omega_n = (n\pi/\ell)^2\sqrt{EI/\rho} \tag{30}$$

and

$$\phi_n(x) = \sin n\pi x/\ell \tag{31}$$

The response of the beam system will now be obtained for a transient and a steady-state type time-varying load.

63.8.2 Response to Steady-State Vibration

The steady-state excitation is a sinusoidal force which is specified by its frequency and peak acceleration in g's.

$$\text{Excitation} \quad P(x)\sin\omega t = \sum_{n=1}^{\infty} P_n \phi_n(x) \quad \sin\omega t \tag{32}$$

$$\text{where:} \quad P_n = \frac{1}{\ell}\int_0^{\ell} P(x)\phi_n(x)\,dx \tag{33}$$

Response

$$y = \sum_{n=1}^{\infty} a_n \phi_n(x) \sin\omega t \tag{34}$$

Substituting the excitation and response into the governing differential equation yields for each mode n.

$$EI\, a_n \frac{\partial^4}{\partial x^4}\left[\phi_n(x)\right] - \rho\omega^2 a_n \phi_n(x) + j\omega c a_n \phi_n(x) = P_n \phi_n(x) \tag{35}$$

where

$$\frac{\partial^4}{\partial x^4}\left[\phi_n(x)\right] = \frac{1}{\beta_n^4}\phi_n(x) \tag{19}$$

$$\omega_n^2 = EI\,\beta_n^4/\rho \tag{18}$$

then

$$a_n\omega_n^2 - a_n\omega^2 + jc\omega a_n/\rho = P_n/\rho \tag{36}$$

$$a_n = \frac{P_n}{\rho(\omega_n^2-\omega^2)+j\omega c} \tag{37}$$

and

$$y = \sum_{n=1}^{\infty} \frac{P_n\phi_n(x)\sin(\omega t-\psi)}{\sqrt{\rho^2(\omega_n^2-\omega^2)^2 + c^2\omega^2}} \tag{38}$$

where $\tan\psi = \omega c/\rho\,(\omega_n^2-\omega^2)$

Making the substitution $\omega_n^2 \rho = EI\beta_n^4$ (18)

$$y = \sum_{n=1}^{\infty} \frac{P_n \phi_n(x) \sin(\omega t - \psi)}{EI\beta_n^4 \sqrt{\left(1 - \frac{\omega^2}{\omega_n^2}\right)^2 + \left(\frac{C}{\rho\omega_n}\right)^2 \left(\frac{\omega}{\omega_n}\right)^2}} \tag{39}$$

which can be written as:

$$y = \sum_{n=1}^{\infty} \frac{P_n \phi_n(x)}{(\ell\beta_n)^4} \frac{\ell^4}{EI} \frac{\sin(\omega t - \psi)}{\sqrt{\left(1 - \frac{\omega^2}{\omega_n^2}\right)^2 + \left(\frac{C}{\rho\omega_n}\right)^2 \left(\frac{\omega}{\omega_n}\right)^2}}$$

The deflection is the infinite sum of the modal deflections due to an excitation

$$P_n = \frac{1}{\ell}\int_0^{\ell} P(x)\phi_n(x)\,dx$$

acting on a mode shape characterized by $\phi_n(x)$ and β_n. Integrals of this type are tabulated in Ref. 3.

The beam response is also a function of the beam parameters:

ℓ = length
EI = stiffness
ρ = density
C = damping coefficient

The amplification factor of a particular mode of resonance, $\omega = \omega_n$, is of interest.

Resonant deflection $y_n = Q_n y_{static}$ (41)

Resonant condition $\omega = \omega_n$ (42)

Then combining equations (40), (41), and (42)

$$Q_n = \frac{\rho\omega_n}{C} \tag{43}$$

The damping factor may be defined as

$$\eta = C/2\rho \tag{44}$$

3.8.3 Amplification Factor for Shock

The shock response of the linear, multiple-degree-of-freedom beam can be obtained by applying the transient response for a single-degree-of-freedom system to the normal coordinates of the beam system. The normal coordinates are the amplitudes in the modes. The amplitude of the steady-state deflection for each mode is:

$$A_n = \frac{P_n}{(\ell \beta_n)^4} \frac{\ell^4}{EI} \tag{45}$$

This amplitude of displacement of the beam for each mode "n" will be modified by the shock response.

The shock requirement used on the LOX pipes is presented in "Vibration and Shock Specifications for Components on Saturn, C-1, Block II Vehicles" (Ref. 1) in terms of peak acceleration for each component or block within the vehicle. The shock test code states that the acceleration shall be applied along each of the three perpendicular axes and shall be one of the following wave shapes.

1. Triangular pulse with duration of 10 milliseconds
2. Half-sine pulse with duration of 8 milliseconds
3. Rectangular pulse with duration of 5 milliseconds.

This analysis considers lateral vibrations which are the most critical. The shock pulses have approximately equal areas and approximately equal responses. The response of a linear, single-degree-of-freedom system with damping for the rectangular shock pulse is now derived. (Ref. 6, pages 8-49,50).

Equation of motion

$$m\ddot{v}+c\dot{v}+kv = g(t) \tag{46}$$

$$\frac{m}{k}\ddot{v}+\frac{c}{k}\dot{v}+v = \xi(t) \tag{47}$$

$$\xi(t) = \frac{g(t)}{k} \tag{48}$$

v = response

ξ = excitation

Also

$$\frac{\ddot{v}}{\omega_n^2} + \frac{c}{k}\dot{v} + v = \xi(t) \tag{49}$$

The Laplace transform with respect to "t" is:

$$\frac{1}{\omega_n^2}\left[S^2F_v(s) - Sv(o) - \dot{v}(o)\right] + \frac{c}{k}\left[SF_v(s) - v(o)\right] + F_v(s) = F_\xi(s) \tag{50}$$

The initial conditions in this case are:

$$v(o) = 0 \tag{51}$$

$$\dot{v}(o) = 0 \tag{52}$$

The subsidiary equation becomes

$$F_v(s) = \frac{F_\xi(s)}{\frac{S^2}{\omega_n^2} + \frac{c}{k}S + 1} \tag{53}$$

Response

$$v(t) = L^{-1}\left[\frac{\omega_n^2 F_\xi(s)}{S^2 + \left(\frac{c}{k}\omega_n^2\right)S + \omega_n^2}\right] \tag{54}$$

For rectangular pulse $\xi(t) = \bar{\xi}$, $0 < t \leq \tau$ (55)

Pulse

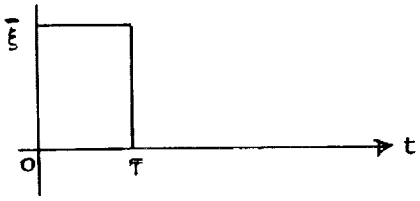

$$F_\xi(s) = L\left\{\xi(t)\right\} = \bar{\xi}/S, \quad 0 \leq t \leq \tau \tag{56}$$

Then

$$v(t) = \bar{\xi}\omega_n^2 L^{-1}\left[\frac{1}{S\left(S^2 + \left(\frac{c}{k}\omega_n^2\right)S + \omega_n^2\right)}\right] \tag{57}$$

Roots of denominators, in addition to S = 0, are

$$S = -\omega_n\left(\frac{c\omega_n}{2k} \pm \sqrt{\frac{c^2\omega_n^2}{4k^2} - 1}\right) \tag{58}$$

Let

$$\zeta = \frac{c\omega_n}{2k} = \frac{c}{2m\omega_n} \tag{59}$$

Rewriting Eq. (57):

$$v(t) = (\bar{\xi}\,\omega_n^2)L^{-1}\left[\frac{1}{s\left[(s+\omega_n(\zeta+i\sqrt{1-\zeta^2})\right]\ s+\omega_n(\zeta-i\sqrt{1-\zeta^2})}\right] \tag{60}$$

Therefore from inverse Laplace tables

$$v(t) = \bar{\xi}\,\omega_n^2\left[\frac{1}{ab} + \frac{be^{-at}-ae^{-bt}}{ab(a-b)}\right] \tag{61}$$

where:

$$a = \omega_n(\zeta - i\sqrt{1-\zeta^2}) \qquad b = \omega_n(\zeta + i\sqrt{1-\zeta^2})$$

then

$$\begin{cases} ab = \omega_n^2 \\ a-b = -2i\omega_n\sqrt{1-\zeta^2} \\ \dfrac{b}{a-b}\,e^{-at} = -\left[\dfrac{\zeta}{2i\sqrt{1-\zeta^2}} + \dfrac{1}{2}\right] e^{-\omega_n\zeta t}\, e^{i\omega_n\sqrt{1-\zeta^2}} \\ -\dfrac{a}{a-b}\,e^{-bt} = +\left[\dfrac{\zeta}{2i\sqrt{1-\zeta^2}} - \dfrac{1}{2}\right] e^{-\omega_n\zeta t}\, e^{-i\omega_n\sqrt{1-\zeta^2}} \end{cases}$$

Therefore Eq. (61) becomes

$$b(t) = \left[1+e^{-\omega_n\zeta t}\left(-\cos\left(\omega_n\sqrt{1-\zeta^2}\right)t - \frac{\zeta}{\sqrt{1-\zeta^2}}\sin(\omega_n\sqrt{1-\zeta^2})t\right)\right] \tag{62}$$

Now $$\zeta = \frac{c\omega_n}{2k} = \frac{c}{2m\omega_n} \tag{59}$$

Let $$\eta = \frac{c}{2m} \quad \text{damping factor} \tag{44-a}$$

then $$\eta = \zeta\omega_n$$

Since the damping ζ is small

$$1 \approx \sqrt{1-\zeta^2} >> \zeta \tag{64}$$

and the frequency

$$\omega_d = \omega_n\sqrt{1-\zeta^2} \approx \omega_n, \tag{65}$$

$$v(t) = \bar{\xi}\left[1-e^{-\eta t}(\cos\omega_n t)\right] \quad 0 \leq t \leq \tau \tag{66}$$

Therefore the dimensionless amplification factor for shock in the "n" mode of vibration of the continuous beam is:

$$\bar{\gamma}_n(t) = \frac{v(t)}{\xi(t)} = 1 - e^{-\eta t}(\cos\omega_n t) \tag{67}$$

Then for $0 < t < \tau$ the transient response is given by Eqs. (14), (45) and (67) as,

$$y = \sum_{n=1}^{\infty} \frac{P_n\phi_n(x)}{(\ell\beta_n)^4}\frac{\ell^4}{EI}\left[1- e^{-\eta t}\cos\omega_n t\right] \tag{68}$$

The solution for bending moment in the vibrating beam based on the deflection relation follows:

$$y = \sum_{n=1}^{\infty} A_n \phi_n(x)\, \bar{\gamma}_n(t) \tag{69}$$

where $A_n \bar{\gamma}_n(t)$ = time response of nth mode

Bending Moment $$M = -EI \frac{d^2y}{dx^2} \tag{70}$$

$$M = -\sum_{n=1}^{\infty} \frac{\ell^4 P_n \dfrac{d^2[\phi_n(x)]}{dx^2}}{(\ell \beta_n)^4} \bar{\gamma}_n(t) \tag{71}$$

where

$$\phi_n''(x) = \frac{1}{\beta_n^2} \frac{d^2[\phi_n(x)]}{dx^2}$$

$\phi_n''(x)$ Tabulated values in Ref. 2.

Then

$$M = -\sum_{n=1}^{\infty} \frac{\ell^2 P_n \phi_n''(x)}{(\ell \beta_n)^2} \bar{\gamma}_n(t) \tag{72}$$

Solution for flexural stress in vibrating beam

$$\sigma_{max} = \frac{MD}{2I} \tag{73}$$

- M = bending moment, in-lb
- D = diameter of pipe
- I = moment of inertia about neutral axis

Solution for Shear force in vibrating beam

Shear force $$Q = -EI \frac{d^3y}{dx^2} \tag{74}$$

$$Q = - \sum_{n=1}^{\infty} \frac{\ell^4 P_n \frac{d^3}{dx^3}\left[\phi_n(x)\right]}{(\ell \beta_n)^4} \bar{\gamma}_n(t) \tag{73}$$

where $$\phi_n'''(x) = \frac{d^3}{dx^3}\left[\phi_n(x)\right] \beta_n^3$$

$\phi_n'''(x)$ Tabulated in Ref. 2

then

$$Q = - \sum_{n=1}^{\infty} \frac{\ell P_n \phi_n'''(x)}{(\ell \beta_n)} \bar{\gamma}_n(t) \tag{76}$$

63.9 References

1. "Vibration and Shock Specifications for Components on Saturn, C-1, Block II Vehicles," Internal Note by Dynamics Section, George C. Marshall Space Flight Center; IN-P VE-S-62-7; May 1962.

2. R. P. Felgar and D. Young, "Tables of Characteristic Functions Representing Normal Modes of Vibration of a Beam," The University of Texas Publication, Circular 44, July 1949.

3. R. P. Felgar, "Formulas for Integrals Containing Characteristics Functions of a Vibrating Beam," The University of Texas Publication; Circular No. 14, 1950.

4. S. H. Crandall, Random Vibration, New York, John Wiley and Sons, Inc., 1958.

5. R. J. Roark, Formulas for Stress and Strain, New York, McGraw-Hill Book Company, Inc., 1954.

6. C. M. Harris and C. E. Crede, Shock and Vibration Handbook, McGraw-Hill Book Company, Inc., 1961.

7. S. Timoshenko, Vibration Problems in Engineering, D. Van Nostrand Company, Inc., 1937.

64. EFFECTS OF RADIATION, VACUUM, AND THERMAL ENVIRONMENTS ON POLYMERIC GASKET MATERIALS

by

J.R. McLoughlin

64.0 Summary

The properties of polymers which are important for their consideration as elements of seals are discussed. The effects of radiation, high vacuum, high temperature, and low temperature on the mechanical behavior of various types of polymers are described. Thermal expansion, the glass transition, stress relaxation, oxidation, thermal degradation, and dynamic behavior are considered.

64.1 Introduction

The chief interest in polymers for use in seals is as the gasket material. In this application the most important properties to be considered are the mechanical properties of the polymer although resistance to attack and degradation by other materials in the environment is, of course, a necessary requirement.

Ideally, a gasket material should respond instantaneously to applied pressure and exert back pressure against the flange or compression element indefinitely. Furthermore, the material should be able to conform readily to temperature changes in the seal area without releasing its back pressure or moving laterally with respect to the compression elements. Such ideal requirements are, of course, very difficult to achieve with real materials except over limited temperature regions. For example, a network polymer in that region of temperature where it exerts ideal rubber behavior will very nearly conform to these requirements. However, if the temperature is raised very far, the rubber will relax its back pressure due to degradation of the polymer network by oxidation or simple thermal breakdown. Even the most thermally resistant rubbers such as silicone rubbers will be attacked slowly at temperatures of 250°C, and the degradation proceeds more rapidly as the temperature is raised. This causes the stress in the rubber to relax so that eventually the gasket ceases to press back against the seal flanges unless the latter are designed to continuously produce pressure by spring action. This process which takes place in a rubber is known as chemical scission, and the stress relaxation which it produces is called chemical stress relaxation. Some rubbers undergo such behavior at lower temperatures than others. For example, polysulfide rubbers undergo chemical scission by a process of opening sulfur bonds at 60-100°C. Ordinary carbon-based natural and synthetic rubbers are somewhat better, depending on exact formulations and anti-oxidants used, but none are very durable at 150°C. More thermally resistant polymers are being investigated, but it is doubtful whether the temperature limit will be raised much above 300°C in the near future. Therefore, polymers can be considered useful as gasket materials only at temperatures of 300 degrees Centigrade and lower.

As the temperature is decreased, another characteristic behavior of polymers must be considered. This is the transition from a rubber-like material to a glass-like material. All polymers exhibit this behavior, although the characteristic hardening takes place at different temperatures for different materials, and the shape of the modulus-temperature curve may be somewhat different due to variations in crystallinity, polarity, chain length and other structural variations. This transition is known as the glass-transition. Most polymers exhibit this behavior at room temperature and above, but some hydrocarbon rubbers have transitions at temperatures well below 0°C, such as polyisobutylene at -74°C, natural rubber at -73°C, and GR-S at -61°C. Some silicone rubbers also have very low glass transitions and are more suitable for use as rubbers at such temperatures than carbon-based rubbers because they do not have as great a tendency to crystallize.

Below the glass transition, all polymers behave like hard solids with Young's moduli of elasticity in the neighborhood of 10^{10} dynes/cm.^{2} (145,000 pounds/sq. inch) and higher. Above the glass transition, a polymer deforms

by uncoiling of long chains of atoms which are linked together in a network of periodic "crosslinks". This is what makes it possible to stretch a rubber several hundred percent. The modulus may be as low as 100 P.S.I. As the rubber is cooled through the transition, it is no longer possible for the chain segments to move freely, and finally they cannot move at all, so that any deformation due to stress can only come through small displacements of chain atoms with respect to neighboring atoms on the same or nearby chains. Because this "freezing-in" process occurs over a rather wide temperature interval, there is another type of stress relaxation which occurs in high polymers at and below the glass transition (and sometimes in crystal transformations). This relaxation is associated with short movements of segments of chains, and its chief importance for this study is that it results in a slow decay of the reaction force which is exerted by a gasket polymer on its restraining flanges. Considerable data on this stress relaxation of polymers in their glassy state (below the glass transition temperature) have appeared in the literature, but most of the direct measurements of relaxation do not extend far below the glass transition, due to the small deformations and long times which are involved in such studies. Instead, the majority of investigators have used dynamic measurements (vibrations) to study the deformation behavior of polymers at low temperatures. Such measurements have been extended down to as low as 4° Kelvin in some cases and to 80° Kelvin in the case of quite a few polymers. A good review of the work done in this field was published recently by A.E. Woodward and J.A. Sauer (Ref. 1). This article presents dynamic shear modulus data and dynamic loss data for such polymers as polymethacrylates, polyvinyl ethers, polyvinyl esters, polyethylene, polyamides, polyurethanes, polyesters, polyvinyl chloride, polyvinylidene chloride, polytrifluorochloroethylene (Kel-F), polytetrafluoroethylene (Teflon) and polyacrylonitrile.

To understand the importance of these measurements to this project, it is only necessary to realize that the small-deflection behavior of a polymer in various modes of distortion such as creep, stress relaxation, and constant rate of strain can be estimated from its behavior in such dynamic measurements. A wealth of information has been published on this subject, much of which has been collected in J.D. Ferry's book, Viscoelastic Properties of Polymers (Ref. 2). If we are interested in the probability of stress relaxation of a polymeric gasket at low temperature which may result in failure by excessive decrease in the force the gasket exerts against its restraining members, we must convert the dynamic data to stress-relaxation data. This can be done approximately by looking at the dynamic loss at a given frequency and temperature. A peak in the dynamic loss-temperature curve means that a mode of relaxation occurs at that temperature. Conversely, a low value of dynamic loss indicates low relaxation at that temperature for that frequency. Polymer properties are very sensitive to time as well as temperature, so behavior at several frequencies is necessary to gain a true understanding. However, it is usually possible to make a frequency-temperature conversion so that we can predict low-frequency behavior from high-frequency behavior by sliding the curves along the temperature scale. That is, the same behavior observed at a certain frequency and temperature will be observed at a lower frequency at a

lower temperature. Considerable experience is available for making this time-temperature transformation based on many polymers. So, from the published information on dynamic losses of polymers at low temperatures, there is available a body of information enabling us to make an approximate prediction of long-time stress relaxation behavior at low temperatures. In general, this shows that most polymers have very little dynamic loss below around -100°C. The most notable exceptions are those polymers which apparently exhibit some crystal transformations at lower temperature, such as polyethylene, polytetrafluoroethylene (Teflon), and polyamides (Nylon). Even these have disappeared at -200°C. Therefore, we can expect very little stress relaxation in polymers at temperatures of -200°C. Instead they will behave like hard solids with a high modulus of elasticity and typically will tolerate only low strains without failure, sometimes less than 1%.

One of the most serious limitations in the use of polymers as gaskets lies in the high coefficient of thermal expansion of polymers compared to metals which are likely to be used in the restraining flanges and compression elements. Polymers have a higher coefficient of expansion in the rubbery state, above the glass transition, where values of linear expansion around 1 to 2 x 10^{-4} per °C are normal. This is about 10 to 20 times as high as most metals. The thermal expansion coefficients of plastics are only about 1/2 to 1/3 as high below the glass transition as above it, but they are still much higher than for metals. The discrepancy between metals and rubbers is not so serious, since a rubbery gasket can readily distort to conform to its metal retaining element. However, as it is cooled below the glass transition, the capacity for the plastic to deform and match the metal surface is diminished rapidly and is practically non-existent at very low temperature. Assuming a seal held in place by metal compressing elements on top and bottom surfaces and cooled to low temperature after compression, the reactive force by the plastic against the compression elements will begin to decrease as soon as the temperature drops through the glass transition. It may actually decrease to zero and the gasket may shrink away from the compressing faces if some provision is not made for a "follow up" spring action by these compression faces. While the flanges can be designed to achieve such a spring action in the direction normal to the compression surface, the mismatch of expansion in a direction parallel to the compression surface is much more difficult to compensate, since the gasket and compression face are in constant contact. This may result in sliding of the gasket across the compression face so that irregularities in the face no longer match the irregularities in the plastic gasket which were molded in at much higher temperature.

These considerations suggest that if relative sliding motion proves to be a problem, the coefficients of expansion of compression face and gasket might be matched by incorporating mineral fillers in the polymer to lower its coefficient of expansion or by making the retaining mechanism out of reinforced plastic in order to raise its coefficient. Since reinforced plastics are now listed among the strongest known materials of construction, this seems like a good possibility. When glass fibers are used as the reinforcement, the thermal coefficient of expansion is much less than that of the basic plastic, while the stress relaxation (or creep) is considerably decreased. Moreover, the strength of the plastic is considerably enhanced.

64.2 Radiation Resistance

The question of radiation resistance of seal materials may arise since the vehicles carrying these seals may pass through belts of high intensity radiation such as the Van Allen belt. However, the seals would be expected to be shielded from direct radiation by other materials, the exact thickness and composition of which would be determined by the design. All we can do now is outline roughly the behavior which might be expected with polymers. The situation is further complicated by the different intensities of radiation and different particles encountered in various parts of the radiation belts. According to a recent report by R.S. Rochlin (Ref. 3), the Van Allen radiation consists of protons and electrons trapped by the earth's magnetic field. The protons have energies ranging as high as 700 M.e.v. or more and are capable of penetrating up to several inches of lead. The energy distribution and number of electrons varies with both positions in the belt and time, but they will be almost completely absorbed by thin layers of shielding. For example, a detector in the Pioneer IV space probe which was shielded by 1 gram/cm.^{2} (equivalent to a 0.050 inch thickness of stainless steel) indicated a total dosage of 10 r./hour in the heart of the inner Van Allen zone. In the heart of the outer zones, the dose ranged from 10 r./hour to 100 r./hour equivalent. It was further reduced by a factor of 50 by 4.6 grams/cm.^{2} additional shielding. These doses correspond to 8.3 Rad./hour maximum in the inner zone and 83 Rad./hour maximum in the outer zones. Examination of a report by C.G. Collins and V.P. Calkins (Ref. 3) on radiation damage in polymers shows that there is no significant damage to most polymers below a dosage of 10^6 Rad.; therefore, the effect of Van Allen radiation on polymeric seals can be safely ignored in the case of vehicles passing through the belt only once. In the case of satellites which may spend significant amounts of time in high radiation intensity zones it might be necessary to design seals with some radiation resistance. Collins and Calkins list the dosage for threshold damage and for 25% damage for a number of polymers, part of which is reproduced on the next page. Since average radiation doses encountered may often be less than 10 Rads./hour and since seals may readily be protected by more than the equivalent of 0.05 inches of stainless steel, it is unlikely that many cases will arise where radiation resistance will be a prime consideration in design.

FIGURE 64.1

Radiation Damage in Plastics and Rubbers (Ref. 4)

Material	Threshold Damage Rads.	25% Damage Rads.
Natural Rubber	2×10^6	2.5×10^7
Butyl Rubber	2×10^6	4×10^6
Neoprene	2×10^6	5.5×10^6
Thiokol ST	5×10^5	1.5×10^6
Silicone Rubber	9×10^5	5.5×10^6
Cellulose Nitrate	6.3×10^5	5.7×10^6
Ethyl Cellulose	1.4×10^6	5.4×10^6
Furan (Duralon) Asbestos & Carbon Filled	3.3×10^8	3.3×10^9
Methyl methacrylate (Plexiglas)	8.2×10^5	1.1×10^7
Trifluorochloroethylene (Fluorothene)	1.3×10^6	2.0×10^7
Phenol Formaldehyde (Unfilled)	2.7×10^6	1.1×10^7
Polyamide (Nylon FM-1)	8.6×10^5	4.7×10^6
Polyethylene Terephthalate (Mylar)	3.0×10^7	1.2×10^8
Polystyrene	8.0×10^8	4×10^9
Polytetrafluoroethylene (Teflon)	1.7×10^4	3.7×10^4
Polyvinyl Chloride (Geon 2046)	1.9×10^7	1.1×10^8
Vinylidene Chloride (Saran)	4.1×10^6	4.5×10^7

Note: Dosage are defined as follows:

Threshold dosage: The dosage at which physical property changes first become apparent. This represents a point at which the functional ability of the material is unchanged.

25% damage dosage: The dosage at which at least one of the physical properties of the material has changed by 25% from its initial value. This was arbitrarily chosen as the point beyond which the usefulness of the solid materials would be questionable.

64.3 Vacuum Effect

The questions of the effect of a high-vacuum environment on the performance of polymeric seals may also be raised. In general, a high vacuum may be expected to cause volatilization of low-molecular-weight materials if any are present. However, volatilization rate is proportional to vapor pressure, and vapor pressure of polymeric materials goes down very fast as molecular weight goes up. Another way of looking at this is to observe that boiling point goes up fast with molecular weight. For example, in the linear dimethyl siloxane polymer series (methyl silicones), the boiling point of the dimer with a molecular weight of 162 is 100°C at 1 atmosphere. As the series progresses to longer and longer chains, the boiling point rises very fast. At molecular weight 278, it is 153°C, at molecular weight 394, it is 194°C, and at a molecular weight of 742, the boiling point is 199°C at a pressure of 0.02 atmospheres. Since rubbers have an infinite molecular weight because they are crosslinked, and even uncrosslinked straight chain polymers have molecular weights in the hundreds of thousands and in the millions, they have substantially zero vapor pressure; therefore, they can be regarded as non-volatile. Some plastics do, however, contain plasticizers which are lower-molecular-weight materials added to increase flexibility. It would be possible to distill out some of these molecules in long periods under high vacuum, particularly at high temperature. The best way to avoid this possibility and consequent property changes is to choose materials without low-molecular-weight plasticizers for use where long exposure under high vacuum is necessary. It is usually necessary to confer with the supplier to make this choice, since it is impossible to tell from trade names which formulations contain low-molecular-weight plasticizers.

64.4 Oxidation Degradation

One effect of high-vacuum environment will be a benefit due to the absence of oxygen. The most rapid deterioration of many plastic materials occurs by a mechanism of oxidation. This effect has been shown to be due to the oxygen in the air which chemically attacks the rubber molecules, cutting them like a pair of scissors. This has been observed by a host of workers, Refs. 8 to 10, who have found that the experimental approach of stretching the rubber in an air oven and measuring the decrease in force required to hold the same extension is a convenient way of measuring the rate of attack by oxygen. Sometimes the oxygen causes crosslinks to form between chains faster than the degradative mechanism can cut chains. In this case the polymer may stiffen with time in oxygen at high temperature rather than soften, as is the case when the chain cutting or scission reaction predominates. In either case, the end product is a deterioration in properties from the standpoint of the seal designer. If scission predominates, the seal will gradually loosen with time as the stress relaxes. If crosslinking predominates, the rubber will become too hard and lose its flexibility, so that it may eventually crack. These processes have been so well documented for some materials that the stress-relaxation curves for different temperatures can be shown to obey the Arrhenius rate law. Figure 64.2 shows how the stress relaxation due to oxidation of natural rubber follows the same curve for different temperatures but displaced along the logarithmic time scale. Such a displacement indicates a process following a simple rate law and having a constant activation energy.

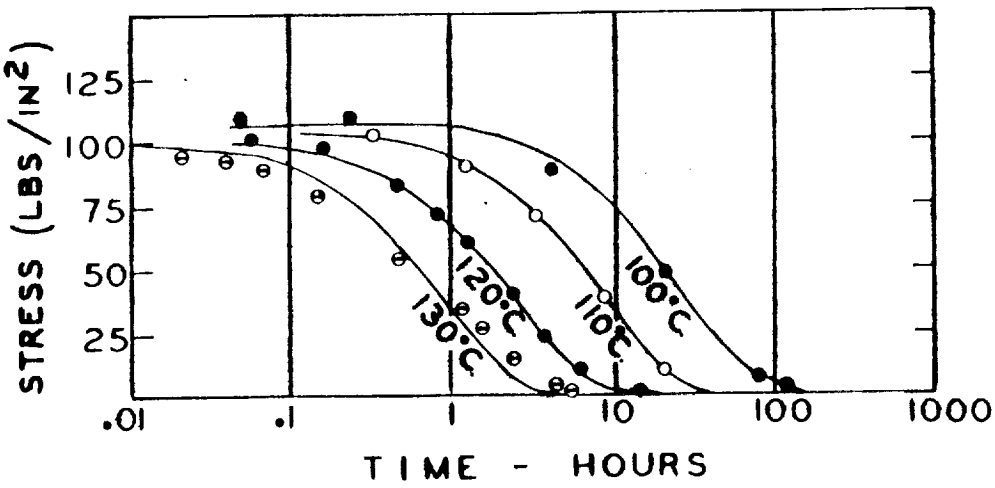

FIGURE 64.2

STRESS RELAXATION OF NATURAL (HEVEA) RUBBER AT SEVERAL TEMPERATURES (Ref. 6)

FIGURE 64.3

STRESS RELAXATION OF POLYSULFIDE RUBBER AT VARIOUS ELONGATIONS AT 60°C (Ref. 6)
(Stress ÷ initial stress)

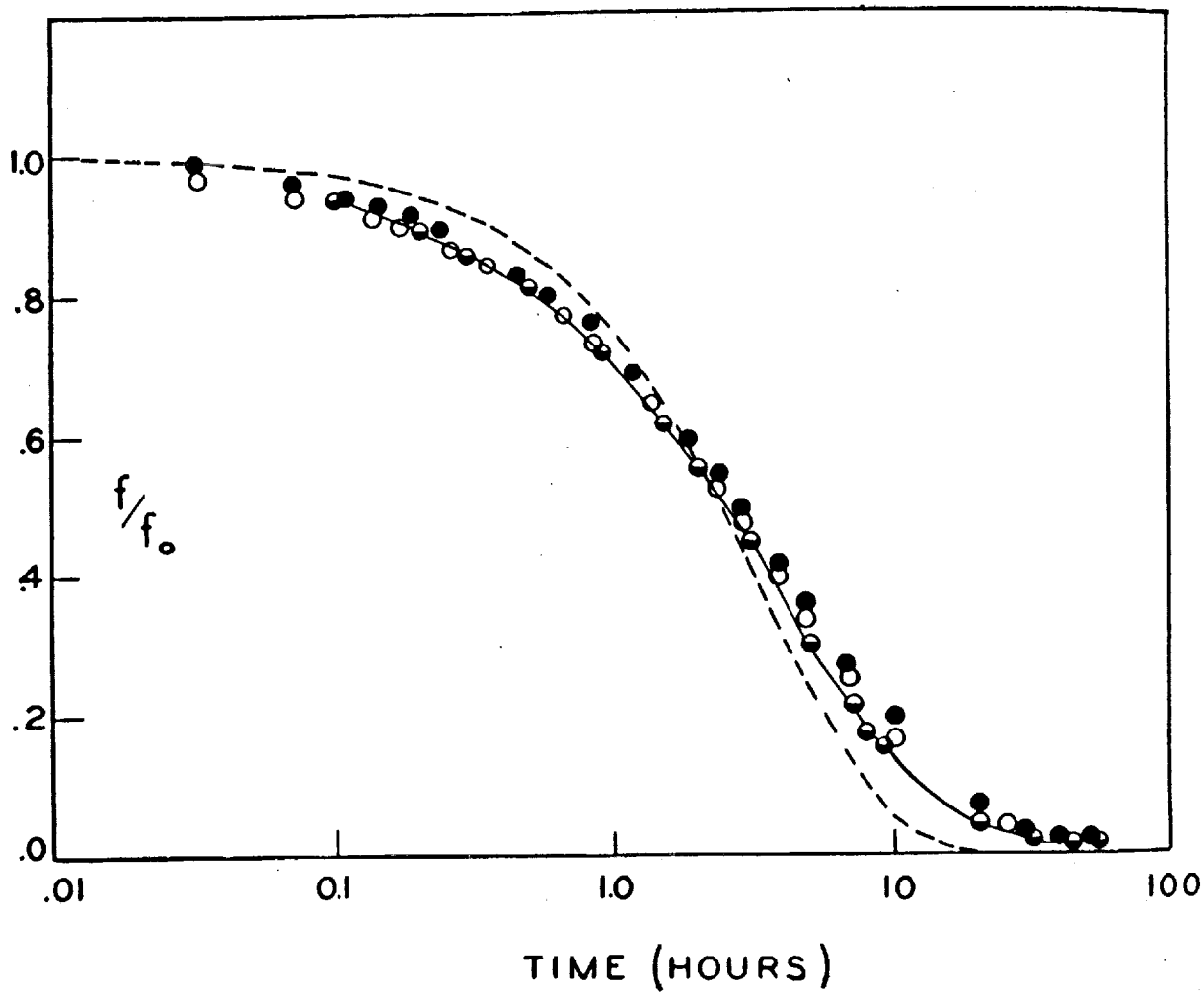

● 10% Elongation
○ 30% Elongation
◒ 50% Elongation

64.5 Thermal Degradation

Naturally, none of these effects will be observed in the absence of oxygen, but there are other types of degradation which can occur in polymers even without oxygen. If the temperature is high enough, polymer chains may begin to split up into smaller fragments, which may volatilize if small enough. Sometimes this process occurs in a kind of polymerization in reverse or chain unzipping. When this happens, polymer molecules lose one monomer unit at a time like beads coming off a string. The monomers are quite volatile at the temperature where this occurs, so they boil off immediately. In polystyrene, for example, this process begins at 300°C.

Another type of degradation at elevated temperature is bond exchange. This results in stress relaxation just as bond scission by oxidation does, but the chemistry is a little different and it does not depend on the presence of oxygen. In polysulfide rubber, for example, bond exchange occurs between sulfur atoms on adjacent chains, resulting in rapid stress relaxation at temperatures as low as 60°C, as illustrated in Fig. 64.3.

A convenient way of ranking the thermal stability of polymers is the use of thermogravimetric analysis. This test consists in heating the polymer sample at a constant rate while accurately measuring its weight change. This is most often done in nitrogen to avoid the effects of oxidation. The weight curve will show a sharp drop where decomposition starts and the temperature at which this occurs can be regarded as a measure of the thermal stability of the polymer.

FIGURE 64.4

Decomposition Temperatures of
Some Common Polymers as Determined by
Differential Thermal Analysis

Material	Temperature, °C
Polystyrene	395
Maleic hardened epoxy	405
Polymethylmethacrylate	345
6-6 Nylon	419
Polytetrafluorethylene (Teflon)	555
Polytrifluorochloroethylene (Kel-F)	410
Viton A	460
Silicone resin	505

64.6 Differential Expansion

As mentioned briefly earlier, the differential coefficient of expansion between polymers and metals will result in the loosening of a seal compressed by metal elements as the temperature is lowered below the glass transition. Furthermore, it will make almost no difference how much the seal is compressed when it is in the rubbery state; as the polymer cools through the glass transition, chain coiling and uncoiling is frozen and the only motions left to the polymer molecules are small displacement of the chain segments with respect to other segments on the same molecule and segments on adjacent molecules. As the polymer is cooled, it would normally shrink, but if it is restrained from doing this by a metal framework, the chain segments will be effectively displaced from their equilibrium positions by an amount equal to the differential coefficient of expansion between the metal and the polymer. Therefore, the force exerted by the polymer molecule on its restraining elements can be calculated roughly by using the strain due to the differential coefficient of expansion and multiplying by the average Young's modulus of elasticity over the temperature interval considered. An example of this behavior is shown in Fig. 64.5. These data were obtained for polymethylmethacrylate (Plexiglas) which exhibits typical rubber-like behavior at temperatures above 105°C and has a glass transition between 80°C and 105°C. The experiments illustrated show the change in force required to hold fixed the elongation of a sample of this material while lowering the temperature. Two different elongations were used; in each case the elongation was applied by stretching the sample at 150°C and then the oven temperature was allowed to drop slowly to room temperature. As soon as the temperature dropped below 100°C, which is in the glass transition, the force (plotted as stress) began to rise and continued steadily up until the oven reached the lowest temperature. The oven was then warmed and the stress fell almost on the same curve with some hysteresis at the glass transition. The important observation is that with two widely different elongations imposed at 150°C, the identical curve was traced below the glass transition. If one assumes that all the strain below the glass transition is due to linear coefficient of expansion of the polymer (9×10^{-5}/°C) and, using an average Young's Modulus of 300,000 P.S.I. in the glassy region, one calculates a stress of 1350 P.S.I. or 93×10^6 dynes/cm.^{2} which is almost exactly what is observed. Thus, the polymer sample "stretched itself" as it cooled. Furthermore, if it had been in a compressed state upon cooling through the glass transition, it would have made little difference; it still would have contracted and either stretched itself or pulled away from its restraining elements unless it was fastened to them by an adhesive.

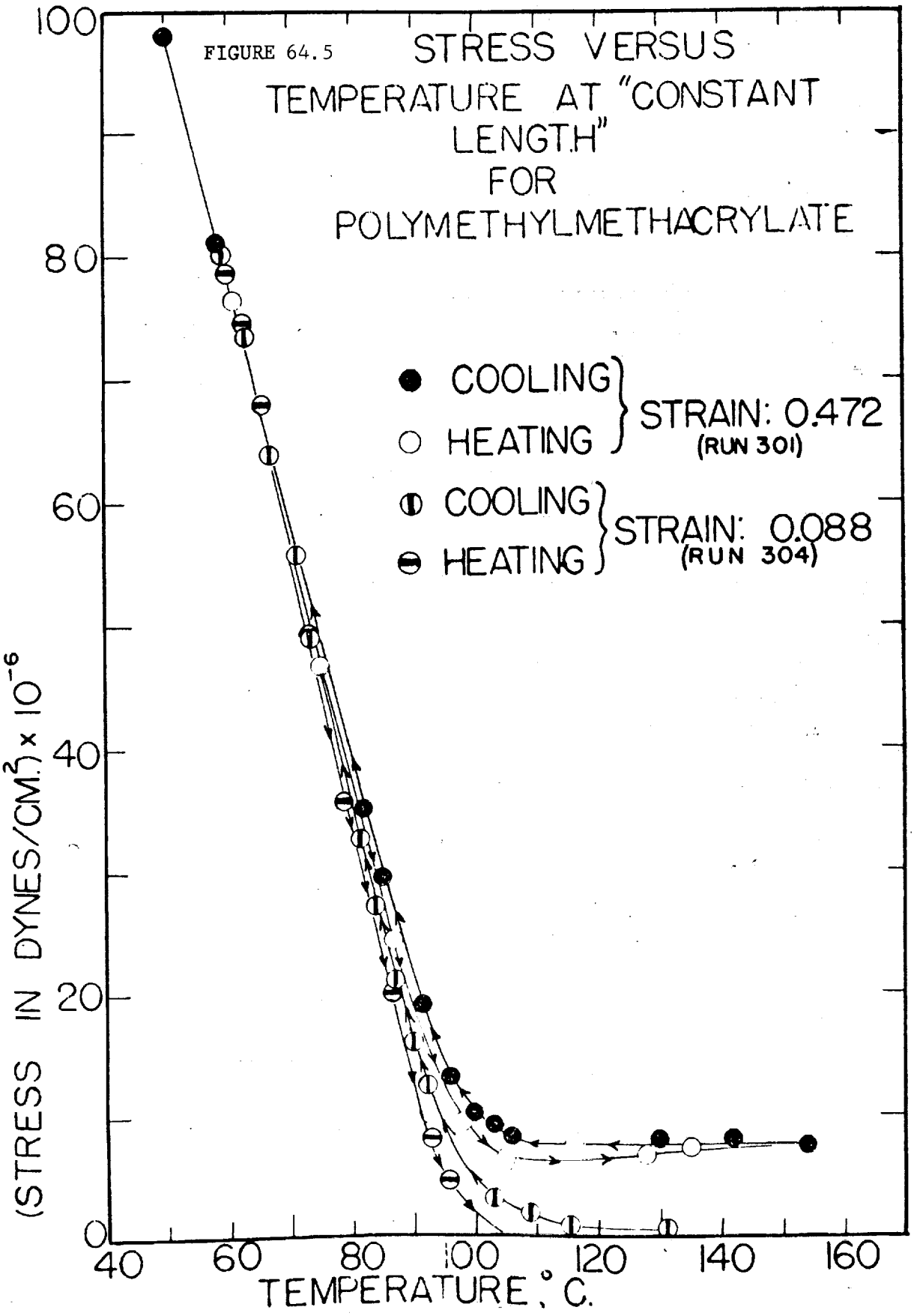
FIGURE 64.5
STRESS VERSUS TEMPERATURE AT "CONSTANT LENGTH" FOR POLYMETHYLMETHACRYLATE
COOLING
HEATING
STRAIN: 0.472
(RUN 301)
COOLING
HEATING
STRAIN: 0.088
(RUN 304)
(STRESS IN DYNES/CM.²) x 10⁻⁶
TEMPERATURE, °C.
0
20
40
60
80
100
40
60
80
100
120
140
160

64.7 Glass Transition

The behavior exhibited by polymethylmethacrylate in the above illustration is a perfectly general one, which will be exhibited by any polymer upon cooling through the glass transition; and it illustrates the importance of knowing the glass transition temperature, the coefficient of expansion of the polymer, and its modulus of elasticity. A further observation in the above example is how closely the stress levels on the warming curve agree with the stress levels on the cooling curve; this illustrates the relatively low degree of stress relaxation which has occurred in the glassy state due to the progressive freezing-in of modes of relaxation as the temperature is lowered.

Since the glass transition is so important in the behavior of polymers, a short table is reproduced below to show where this transition falls for some common polymers. It will be noted that all the polymers listed encounter this transition upon cooling to -100°C.

FIGURE 64.6

Polymer Glass Transition Temperatures

Material	Glass Transition, °C
Polyisobutylene	-74
Natural Rubber (Hevea)	-73
Polyvinyl acetate	+32
Polyurethane	-35
Polystyrene	100
Polymethylmethacrylate (Plexiglas)	105
Polyvinyl chloride	74
Butadiene - styrene rubber	-33
Silicone rubber	-80
Polytetrafluoroethylene (Teflon)	+25

The way in which the modulus of elasticity increases sharply as temperature decreases below the glass transition is illustrated in the curves shown in Fig. 64.7. These depict the shear modulus of several rubbers as a function of temperature. It will be noted that an increase in modulus ranging between a factor of 100 and 1000 occurs in a fairly narrow temperature interval.

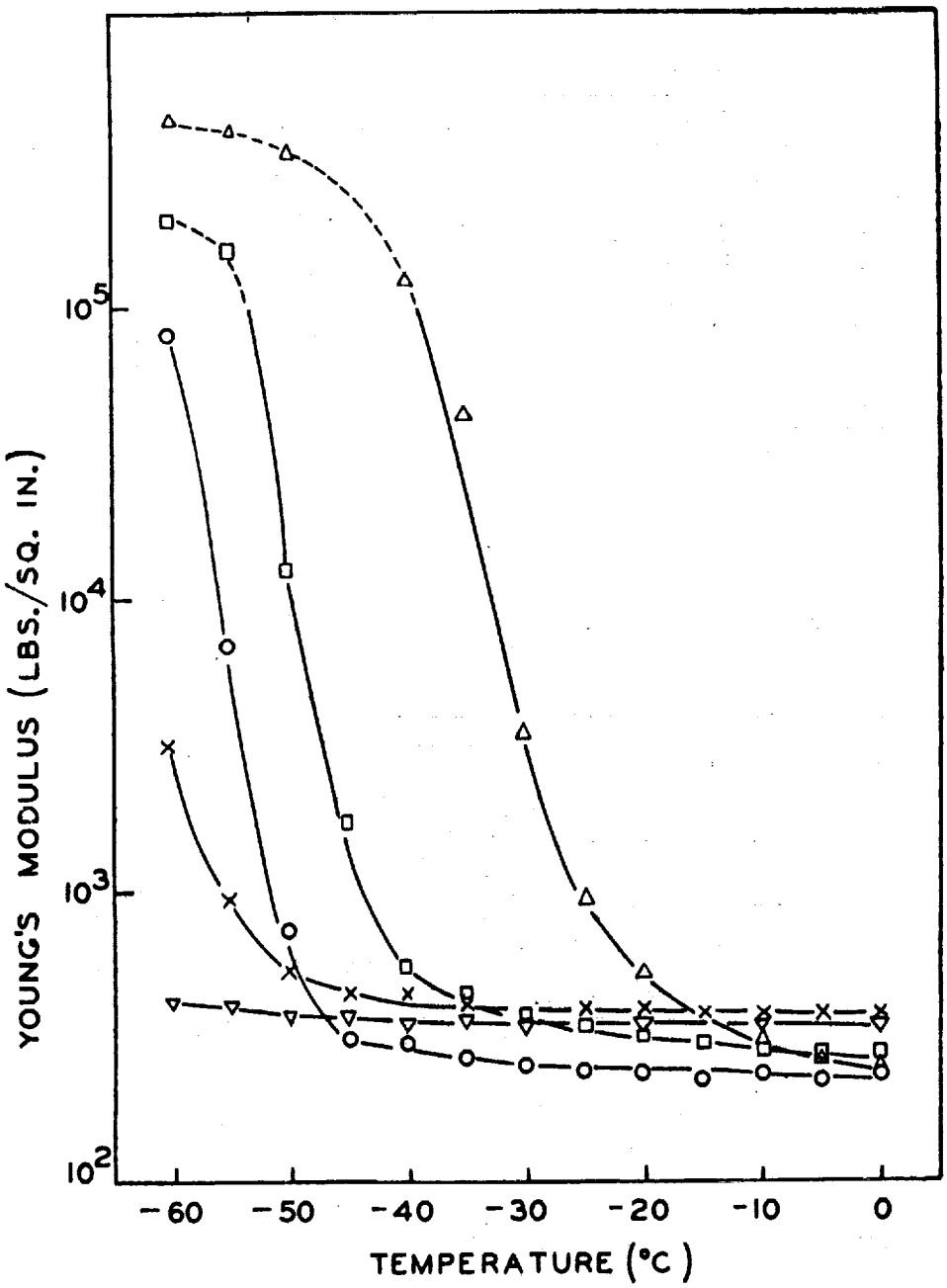

FIGURE 64.7

YOUNG'S MODULUS VS. TEMPERATURE FOR VARIOUS VULCANIZED RUBBERS (Ref. 6)

- ○ natural rubber
- ▽ polybutadiene
- × butadiene-styrene 85/15
- □ butadiene-styrene 75/25
- △ butadiene-styrene 60/40

64.8 Glassy State Stress Relaxation

The properties of polymers in the glassy state below the glass transition are an important consideration where polymers are to be used as seals at low temperature. Some polymers have been studied directly in this temperature region by use of stress relaxation measurements (Refs. 11, 12). These measurements show that stress relaxation does indeed occur in glassy polymers, but at a very slow rate compared to relaxation in the transition region. The relaxation is, of course, a function of temperature and depends on free volume and often on water content and plasticizer content. The free volume in a polymer below its glass transition depends on thermal history. Samples cooled rapidly have greater free volume than those cooled more slowly; therefore, rapidly cooled samples exhibit greater relaxation of stress at low temperature than those which have more time to accommodate to the temperature change during the cooling process.

Because relaxation is a slow process in the glassy state, and due to experimental difficulties in measurements at low temperatures over long periods of time, few relaxation measurements have been made directly on polymers below the glass transition where the glass transition occurs at low temperature. Instead, the technique of dynamic measurements has been widely used to study the response of polymers at small deflections below their glass transition temperatures. This technique consists in subjecting the specimen to a cyclic load and measuring the amplitude and phase shift of the resulting deflection. The ratio of stress amplitude to strain amplitude is the complex modulus of elasticity, and the phase angle between the stress amplitude and strain amplitude is the loss angle δ. For a material with zero loss, the stress amplitude and strain amplitude would be in phase, and the angle δ would be zero. The tangent of the angle δ indicates the relative magnitudes of viscous and elastic effects in the material, and hence the relative degree of stress relaxation to be expected. For a simple Maxwell (spring - dashpot) viscoelastic model of the material, the relaxation time is the time for 63% decay in stress under a steady-state deformation and is $10/\pi$ times the period of oscillation for which $\tan \delta = 0.05$.

By making measurements at different frequencies and temperatures, it is sometimes possible to estimate long-term behavior at low temperatures from higher-frequency behavior at higher temperatures. In order for this to be done, it is necessary that all parts of the frequency-response curve have the same temperature dependency. This is a fair assumption if all the measurements are made far enough below the glass transition. At the present time, however, only limited frequency and temperature response data are available for most polymers at low temperatures, so only qualitative remarks concerning their viscoelastic behavior can be made. That is, it can certainly be said that polymers which exhibit low dynamic losses below their glass transitions will exhibit low stress relaxation. Some dynamic measurements on Plexiglas and polyethylene are shown in Figures 64.8 and 64.9, respectively. Examination of some of these dynamic-losses-versus-temperature plots which contain data at several frequencies shows that the loss curves shift to lower temperature in a fairly uniform manner as the frequency is reduced. For

example, in Figure 64.8, the point where tan δ is 0.05 shifts from 35°C to -20°C as the frequency is reduced from 2000 c.p.s. to 0.4 c.p.s. If one assumes that the shift is uniform on a logarithm-of-frequency scale, the temperature at which tan δ is 0.05 at a frequency of 8×10^{-5} c.p.s. would be -75°C. A frequency of 8×10^{-5} c.p.s. corresponds to a relaxation time of 40,000 seconds, or about half a day. This means that there would be substantial decay in stress observed in Plexiglas when strained at -75°C and held at constant strain during a period of half a day. However, such a stress relaxation on this time scale would fall off fast at lower temperatures, since the loss is decreasing with temperature at the frequency for which tan $\delta = 0.05$. These are only qualitative interpretations of the data, which is all that is possible where the frequency-loss curves do not slide perfectly along the temperature scale, as evidenced by the fact that the loss peak height is much greater at 2000 c.p.s. than at 0.4 c.p.s. The fact that the loss peak height decreases with reduction in temperature would suggest that the relaxation would be even lower at -75°C than the above simple extrapolation might indicate.

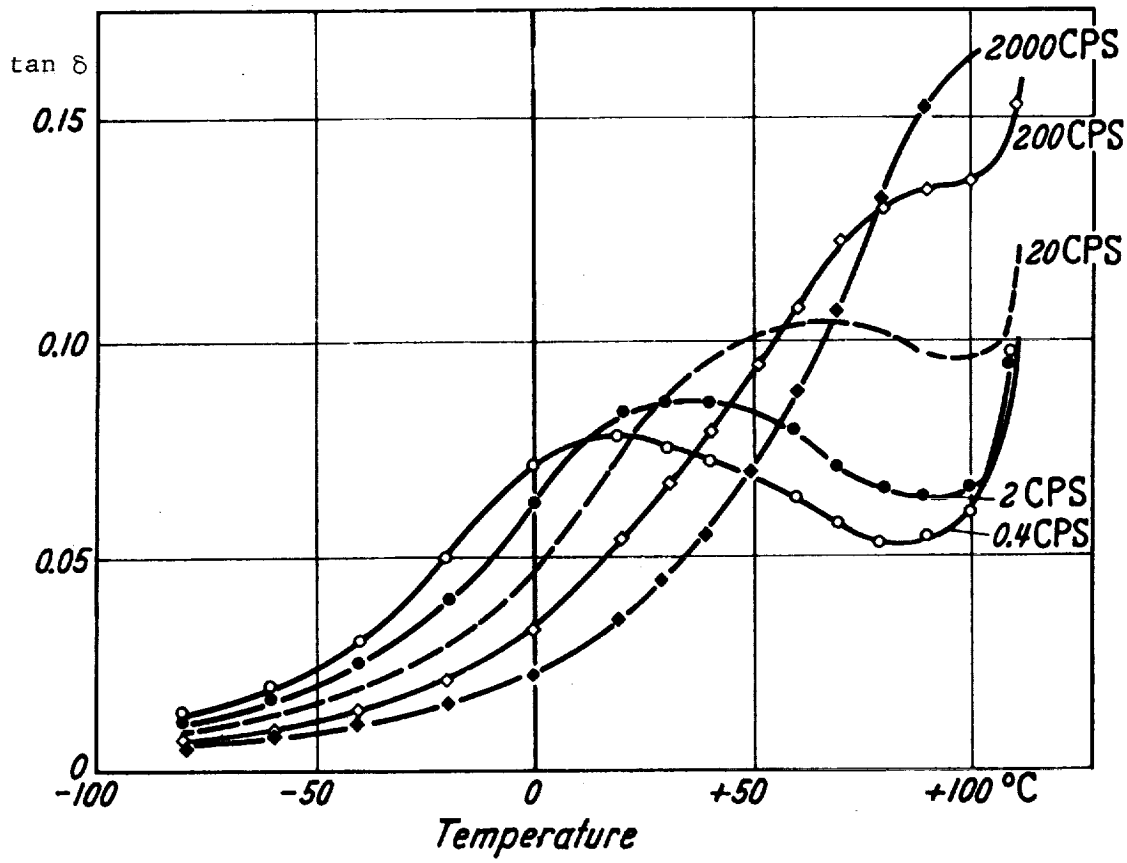

FIGURE 64.8

MECHANICAL DAMPING OF POLYMETHYLMETHACRYLATE
(PLEXIGLAS) AS A FUNCTION OF TEMPERATURE AND FREQUENCY (Ref.1)

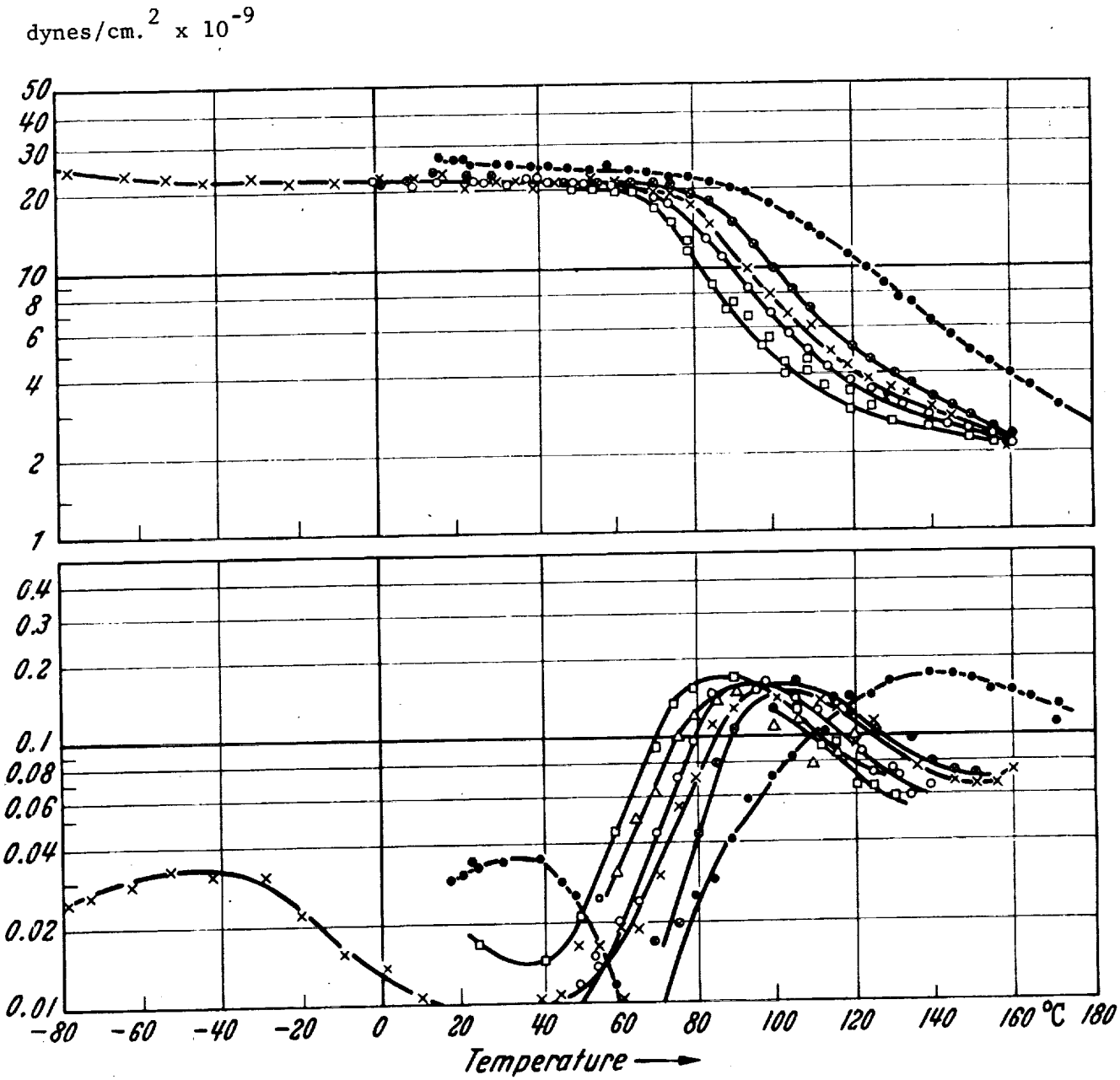

FIGURE 64.9

MODULUS AND LOSS ANGLE TANGENT, TAN δ, OF UNORIENTED CRYSTALLINE POLYETHYLENE TEREPHTHALATE AT VARIOUS FREQUENCIES (Ref. 1)

- ● 10,000 c.p.s.
- ⊗ 5.9 c.p.s.
- × 0.72 c.p.s.
- ○ 0.082 c.p.s.
- △ 0.0094 c.p.s.
- □ 0.001 c.p.s.

64.9 Ultimate Strength and Elongation at Low Temperature

When a limited amount of dynamic measurements are available at too few frequencies, it is difficult to carry out the necessary correlations between dynamic measurements and stress relaxation. More measurements of dynamic properties at low temperature are needed to predict low-temperature stress relaxation, but an even greater need is for ultimate-strength measurements on polymers at low temperatures, since these materials can be expected to be brittle below the glass transition temperature; the lower the temperature below the glass transition, the greater the likelihood of brittleness will be. Yet, only limited data are available (Ref. 13) to show either how much stress various polymers will endure at very low temperatures or how much elongation they will endure before breaking. These measurements are probably of greater importance than stress relaxation, creep, or dynamic measurements since failure by cracking at these temperatures seems to be a much greater possibility than failure by distortion. It must be remembered that no known rubbers act like rubbers at liquid-oxygen and liquid-nitrogen temperatures. All are more or less brittle, glass-like materials, just as are all plastics. Which materials are least subject to low elongation failure would seem to be the key question, and this can only be answered by experiment.

64.10 Conclusions

Exposure to the intensity and kind of radiation exhibited in the Van Allen belts will not have a serious effect on polymer properties unless exposure times of years are required or unless the polymeric materials are exposed without shielding.

The effect of high vacuum on polymer properties will be negligible unless the formulation contains more than small amounts of low molecular weight plasticizers or solvents.

High temperatures cannot be tolerated by polymers very long. Many rubbers oxidize and either soften or embrittle at temperatures of 150°C (302°F) and lower. Others undergo chemical changes without oxygen. Thermoplastics such as polystyrene and polymethylmethacrylate revert to monomer at temperatures over 300°C (572°F) and their properties deteriorate slowly at much lower temperature. Polysulfides deteriorate at 60°C (140°F). Higher temperature polymers are in development but 250-300°C looks like the upper operation limit at present for these materials.

Low temperature causes all polymeric materials to stiffen because they pass through glass transitions before reaching -100°C (-148°F). In their glassy state below this transition, all polymers are very stiff and more or less brittle although very little information is available on strengths or failure elongations at liquid oxygen and liquid nitrogen temperatures. Dynamic measurements have been made at such low temperatures; these reveal high moduli and very little flow.

All polymers have much greater thermal expansion coefficients than metals and, therefore, present problems if used in contact with metals at low temperature where the polymers have little flexibility or flow and, hence, cannot accommodate as well. The use of fillers to decrease expansion coefficients of polymers is a possibility, but most fillers increase stiffness and decrease the failure elongation in the glassy state. The use of fiber-reinforced, polymeric supporting elements in contact with polymeric gaskets may help relieve the problems due to coefficient-of-expansion differences.

64.11 References

1. A.E. Woodward and J.A. Sauer, "The Dynamic Mechanical Properties of High Polymers at Low Temperatures", Fortschritte Der Hochpolymeren-Forschung (Advances in Polymer Science), Band 1, Heft 1, p. 114 (1958).

2. J.D. Ferry, The Viscoelastic Properties of Polymers, John Wiley and Sons, Inc., 1961.

3. R.S. Rochlin, "Ionizing Radiation in Space," Vol. 5, General Electric Co. Technical Information Series Report No. 60GL16 (1960).

4. C.G. Collins, V.P. Calkins, "Radiation Damage to Elastomers, Plastics & Organic Liquids," General Electric Co. Report APEX-261, U.S. Department of Commerce, Office of Technical Services, 1956.

5. A.D. McIntyre, "Low-Temperature Properties of Rubbers," J. Appl. Pol. Sci. 5, 195 (1961).

6. A.V. Tobolsky and H. Mark, Physical Chemistry of High Polymeric Systems, Interscience Publishers, 1950.

7. A.E. Woodward, J.A. Sauer, R.A. Wall, "Partially Crystalline Polyolefins," J. Pol. Sci. 50, 117 (1961).

8. A.V. Tobolsky, D. Metz, R.B. Mesrobian, J.A.C.S. 72, 1942 (1950).

9. M. Mochulsky and A.V. Tobolsky, Ind. Eng. Chem. 40, 215 (1948).

10. R.D. Andrews, E.E. Hanson and A.V. Tobolsky, J. Appl. Phys. 17, 352 (1946).

11. J.R. McLoughlin and A.V. Tobolsky, "The Viscoelastic Behavior of Polymethylmethacrylate," J. Colloid. Sci. 7, 555 (1952).

12. A.V. Tobolsky and J.R. McLoughlin, "Elastoviscous Properties of Polyisobutylene V. The Transition Region," J. Pol. Sci. 8, 543 (1952).

13. T.F. Durham et al., Cryogenic Materials Data Handbook, Supplement 3, U.S. Department of Commerce, Office of Technical Services, 1961. (See Section H.2 for Kel-F, Section H.3 for Mylar, Section H.4 for Nylon, and Section H.5 for Teflon).

DISTRIBUTION LIST FOR REPORTS ON CONTRACT NAS 8-4012

NASA Headquarters, Washington 25, D.C.

Mr. Henry Burlage, Jr.
Chief, Liquid Propulsion Systems, RPL (3)

Mr. A.O. Tischler
Assistant Director for Propulsion, MLP (1)

NASA, Marshall Space Flight Center, Huntsville, Alabama

Mr. Charles Wood (M-P&VE-PT), Technical Manager (24)
Office of Technical Information, M-MS-IPC
Contracting Officer, M-P&C-C
Patent Office, M-PAT

NASA Other Locations

Technical & Scientific Information Facility
Attention: NASA Representative, Code CRT
P.O. Box 5700, Bethesda, Maryland (24)

Attention: Technical Librarian

Ames Research Center
Moffett Field, California (2)

Goddard Space Flight Center
Greenbelt, Maryland (2)

Jet Propulsion Laboratory
California Institute of Technology
4800 Oak Grove Drive
Pasadena, California (2)

Langley Research Center
Langley Field, Virginia (2)

Lewis Research Center
21000 Brookpark Road
Cleveland 35, Ohio (2)

Marshall Space Flight Center
Huntsville, Alabama (2)

Manned Spacecraft Center
Houston, Texas (2)

Advanced Research Projects Agency
Pentagon, Room 3D154
Washington 25, D.C.

Aeronautical Systems Division
Air Force Systems Command
Wright-Patterson Air Force Base, Ohio

Attention: Technical Librarian

Air Force Missile Development Center
Holloman Air Force Base, New Mexico

Air Force Missile Test Center
Patrick Air Force Base, Florida

Air Force Systems Command, Dyna-Soar
Air Force Unit Post Office
Los Angeles 45, California

Army Ordnance Missile Command
Redstone Arsenal, Alabama

Armed Services Technical Information Agency
Arlington Hall Station
Arlington 12, Virginia

Arnold Engineering Development Center
A.E.O.R.
Tullahoma, Tennessee

Bureau of Naval Weapons
Department of the Navy
Washington 25, D.C.

Central Intelligence Agency
2430 E. Street, N.W.
Washington 25, D.C.

Headquarters, United States Air Force
Washington 25, D.C.

Office of Naval Research
Washington 25, D.C.

Attention: Technical Librarian

Picatinny Arsenal
Dover, New Jersey

Rocket Research Laboratories
Edwards Air Force Base, California

U.S. Naval Ordnance Test Station
China Lake, California

U.S. Atomic Energy Commission
Technical Information Services
Box 62
Oak Ridge, Tennessee

Liquid Propellant Information Agency
Johns Hopkins University
Applied Physics Laboratory
8621 Georgia Avenue
Silver Spring, Maryland

Aerojet-General Corporation
P.O. Box 296
Azusa, California

Aerojet-General Corporation
P. O. Box 1947
Sacramento 9, California

Aeronutronic
A Division of Ford Motor Company
Ford Road
Newport Beach, California

Aerospace Corporation
2400 East El Segundo Boulevard
El Segundo, California

Arthur D. Little, Inc.
Acorn Park
Cambridge 40, Massachusetts

Astropower, Inc., Subsidiary of Douglas
Aircraft Company, Inc.
2968 Randolph Avenue
Costa Mesa, California

Astrosystems, Inc.
82 Naylon Avenue
Livingston, New Jersey

Atlantic Research Corporation
Edsall Road and Shirley Highway
Alexandria, Virginia

Attention: Technical Librarian

Beech Aircraft Corporation
Boulder Facility
Box 631
Boulder, Colorado

Bell Aerosystems Company
P. O. Box 1
Buffalo 5, New York

Bendix Systems Division
Bendix Corporation
Ann Arbor, Michigan

Boeing Company
P. O. Box 3707
Seattle 24, Washington

Convair (Astronautics)
Division of General Dynamics Corporation
P. O. Box 2672
San Diego 12, California

Curtiss-Wright Corporation
Wright Aeronautical Division
Wood-ridge, New Jersey

Douglas Aircraft Company, Inc.
Missile and Space Systems Division
3000 Ocean Park Boulevard
Santa Monica, California

Fairchild Stratos Corporation
Aircraft Missiles Division
Hagerstown, Maryland

General Electric Company
Missile and Space Vehicle Department
Box 8555
Philadelphia, Pennsylvania

General Electric Company
Rocket Propulsion Units
Building 300
Cincinnati 15, Ohio

Grumman Aircraft Engineering Corporation
Bethpage, Long Island, New York

Kidde Aero-Space Division
Walter Kidde and Company, Inc.
675 Main Street
Belleville 9, New Jersey

Attention: Technical Librarian

Lockheed Aircraft Corporation
Missile and Space Division
Sunnyvale, California

Lockheed Propulsion Company
P.O. Box 111
Redlands, California

Marquardt Corporation
16555 Saticoy Street
Box 2013 - South Annex
Van Nuys, California

Martin Division
Martin Marietta Corporation
Baltimore 3, Maryland

Martin Denver Division
Martin Marietta Corporation
Denver, Colorado

McDonnell Aircraft Corporation
P. O. Box 6101
Lambert Field, Missouri

North American Aviation, Inc.
Space & Information Systems Division
Downey, California

Northrup Corporation
1001 East Broadway
Hawthorne, California

Pratt & Whitney Aircraft Corporation
Florida Research & Development Center
West Palm Beach, Florida

Radio Corporation of America
Astro-Electronics Division
Defense Electronic Products
Princeton, New Jersey

Reaction Motors Division
Thiokol Chemical Corporation
Denville, New Jersey

Republic Aviation Corporation
Farmingdale
Long Island, New York

Attention: Technical Librarian

Rocketdyne (Library Dept. 586-306)
Division of North American Aviation, Inc.
6633 Canoga Avenue
Canoga Park, California

Space General Corporation
9200 Flair Avenue
El Monte, California

Space Technology Laboratories
P. O. Box 95001
Airport Station
Los Angeles 45, California

Stanford Research Institute
333 Ravenswood Avenue
Menlo Park, California

TAPCO Division
Thompson-Ramo-Wooldridge, Inc.
23555 Euclid Avenue
Cleveland 17, Ohio

Thiokol Chemical Corporation
Redstone Division
Huntsville, Alabama

United Aircraft Corporation
East Hartford Plant
400 Main Street
Hartford, Connecticut

United Technology Corporation
587 Methilda Avenue
Sunnyvale, California

Vought Astronautics
Box 5907
Dallas 22, Texas

Armour Research Foundation
Illinois Institute of Technology
10 West 35th Street
Chicago 16, Illinois

Battelle Memorial Institute
505 King Avenue
Columbus 1, Ohio

National Bureau of Standards
Cryogenic Engineering Laboratory
Boulder, Colorado